AN OPTICAL ~~STUDY OF~~ INVESTIGATION INTO SHOCK WAVE PHENOMENA IN LIQUIDS AND SOLIDS

by

CHARLES JOHN WYKEHAM HEDLEY

Department of Physics
Royal Holloway College

This thesis is presented for the Degree of Doctor of Philosophy in the University of London

May, 1973.

ABSTRACT

Methods for the production and detection of shock waves are reviewed with particular emphasis on the production of shock waves by exploding wires and by the absorption of energy from a pulsed laser system.

An exploding wire system is described for the generation of shock waves in perspex plates. Observation is made using the stress induced birefrigence, and 'time integrated' photographs of shock waves are produced. At lower energies the exploding wire produces a mixture of wire vapour and molten droplets. The disintegration of the droplets is shown and described in terms of the mechanism shown by Lane and Edwards[104] to operate for water droplets.

A modified Kerr cell shutter with an unsymmetric electrode geometry is described with reference to possible use as a fast light shutter for measuring shock wave velocities. A development of this shutter has one of the electrodes in the Kerr cell consisting of a stack of razor blades. Light which has been diffracted from an electrostrictively induced phase grating near the blade edges, has been detected. A number of mechanisms are described which take effect within the modified cell.

A system for the production and detection of shock waves by a Q-switched ruby laser is described. Shock waves are produced in liquids both by electrical breakdown and by evaporation of the surface material from a metal target. Experimental results show the production of shock waves with velocities up to 10^4 m/s in water. The ablation wave produced when the surface of a metal wire is evaporated by a laser has been photographed. This shock wave accelerates as it moves towards the centre of the wire. Finally, the process of stimulated Brillouin scattering is described as the pulsed laser is focused into a liquid.

CONTENTS

C O N T E N T S

(continued)

CONTENTS
(continued)

CHAPTER I

INTRODUCTION

1.1 EARLY WORK

The mechanism of shock wave production has been extensively investigated during the last 130 years. Stokes (1848)[1] noted that in the classical theory of sound, the leading edge of a large amplitude wave would tend to steepen as the wave velocity increases with the density of the medium. The equations of motion in a perfectly elastic medium assumes that the adiabatic elastic moduli are independent of the compression. In the case of real materials this is approximately true only for very small disturbances. In order to obtain more exact solutions one must assume that there are some non-linear terms in the velocity. Approximate solutions of the non-linear equations show, that for large amplitudes, the leading edge of the wave steepens until it develops into a discontinuity. Meanwhile, the back face becomes less steep. Stokes suggested that the limiting steepness of a wave depends on the thermodynamical properties of the fluid in which the disturbance is taking place. In particular, heat conduction and the viscous damping factor would affect the thickness of the transition.

An exact solution of the more general equations can be obtained if a steady propagation of an unchanging profile is possible. The profile was labelled by Lord Rayleigh, (1910)[2] as the permanent regime profile, and its existence is dependent on Earnshaw's relation, ignoring irreversible processes, $\left(\frac{\partial^2 P}{\partial V^2}\right)_s = 0$ being satisfied across the shock front[3].

In a medium, a shock wave is a region of very small thickness across which the thermodynamic properties of the medium all change. Flow upstream from the shock wave is supersonic[4], and downstream the flow is subsonic. The thickness of the shock transition is found to decrease with

the increasing strength of the wave, and for strong shock waves it is only slightly larger than the mean free path in the material.

Rankine (1870) and Hugoniot (1889) formulated the relationships between the shock wave's velocity and the thermodynamic equation of state for a polytropic gas[5-7]. The shock adiabatic, also known as the Hugoniot Relation describes the shock wave in terms of the thermodynamical variables of the medium. It is derived from the Rankine-Hugoniot relations which are a statement of the conservation laws across the shock wave, and is of the form:

$$\epsilon_1 - \epsilon_2 + \tfrac{1}{2}(V_1 - V_2)(p_1 + p_2) = 0 \ . \qquad \ldots (1.1.1)$$

The first two Rankine-Hugoniot relations for a travelling shock front are derived only from the conservation of momentum and mass and thus apply even when energy is being generated in the medium, as is the case with detonation waves.

The fourth condition across the shock front[7] is that entropy is discontinuous. We have

$$\rho_2 S_2 v_2 - \rho_1 S_1 v_1 \geq 0 \ . \qquad \ldots (1.1.2)$$

Thus a shock wave is a means whereby energy is dissipated in ideal fluid flow, the dissipation taking place totally within the very narrow region defined by the thickness of the shock front.

1.2 WEAK AND STRONG SHOCK WAVES

The Hugoniot relation is a general equation which holds for shock waves of all strengths. Whilst in the case of a strong shock wave the values of p_1, ρ_1 and ϵ_1[4] can usually be neglected, for a weak shock wave the discontinuities in all the variables are small. The Hugoniot can thus be transformed and expanded in terms of the powers of the small differences. As a result of the second order terms of $p_2 - p_1$ cancelling

out, the discontinuity in entropy is third order of smallness compared to the pressure discontinuity. The compressibility $-\left(\frac{\partial V}{\partial p}\right)_s$ decreases with increasing pressure so $\left(\frac{\partial^2 V}{\partial p^2}\right)_s > 0$.

From momentum conservation considerations $j^2 = (p_2 - p_1)/(V_1 - V_2)$ for a weak shock wave this can be written so that $j^2 = -\left(\frac{\partial p}{\partial V}\right)_s$, thus the velocities v_1 and v_2 are approximately equal, and hence:

$$v_1 = v_2 = v = jV = \sqrt{\left[-V^2\left(\frac{\partial p}{\partial V}\right)_s\right]} = \sqrt{\left(\frac{\partial p}{\partial \rho}\right)_s} \quad . \qquad \ldots (1.2.1)$$

This is the velocity of sound, i.e. $v = c$, at this limit we can see that a weak shock wave decays to produce a sound wave.

1.3 THE THICKNESS OF SHOCK WAVES

Taylor and Maccoll (1935)[8] considered the fluid as continuous across the shock front and yielded figures for the shock front thickness by assuming that the thermal conductivity and viscosity are linear in terms of the velocity and thermal gradients. These values showed that for a shock front with a pressure ratio across the transition region of ~ 1.15, the front was 3×10^{-4} cm thick. A strong shock with a pressure ratio of 8 across the shock, has a thickness $\sim 10^{-5}$ cm.

These calculations were for air, and as 10^{-5} cms is approximately the mean free path in air, a number of workers approached the problem considering classical kinetic theory. This approach produces the result that the shock front thickness is never small compared with the mean free path, but for extremely strong shocks the Maxwellian distribution of molecular velocities is not adhered to and one must consider the relaxation times of the individual molecules, as this produces a limitation on the rate at which energy can be transferred.

1.4 THEORY FOR CYLINDRICAL AND SPHERICAL SHOCK WAVES

The problem considered in this thesis is the generation and detection of shock waves in liquids and solids, and the measurement of shock wave velocities. In the experimental work, shock waves are produced by means of a laser induced plasma and from exploding wires.

Taylor[9,10] has considered the idealized problem of a finite amount of energy suddenly released in an infinitely concentrated form. This work, carried out during the second world war, gives the mathematics for such a shock wave produced from an atomic explosion. In such an explosion, the particle velocity is far in excess of the smaller amplitude wave velocity of the medium.

The radius of the shock wave is related to the time elapsed since its creation by the equation:

$$R = S(\gamma)\ t^{2/5}\ E^{1/5}\ \rho_0^{-1/5} \ . \qquad \ldots (1.4.1)$$

Taylor's analysis is for a strong explosion in air. Most of the air within the shock front is forced into a thin shell just inside that front. As the front expands, the maximum pressure decreases, and below 10 atmos., the equation is no longer accurate.

In the ideal problem, the maximum pressure is proportional to R^{-3} and this is found experimentally to be true in the regions close to a high explosive detonation. At great distances R from the centre of the explosion, the pressure decays as in a sound wave, proportional to R^{-1}.

In this type of shock wave, the intensity decreases as the radius gets larger, but the total energy within the wave remains constant. For this wave, the similarity assumptions can be made so that:

$$\text{pressure,} \qquad p/p_0 = y = R^{-3}\ f_1 \ ,$$
$$\text{density,} \qquad \rho/\rho_0 = \psi \ ,$$
$$\text{radial velocity,} \qquad u = R^{-\frac{3}{2}}\ \varphi_1 \ ,$$

where R is the radius forming the outer edge of the disturbance; p_0 and ρ_0 are the pressure and density in the undisturbed region. If r is the radial coordinate, $\eta = r/R$ and f_1, φ_1 and ψ are functions of η. These assumptions are consistent with the equations of state, motion and continuity.

Lin[12] has extended Taylor's analysis to the cylindrical case. In Lin's problem, the finite amount of energy is instantaneously released along a straight line of infinite extent. The calculation of pressure, density and velocity are carried out using a set of similarity assumptions similar to Taylor's.

$$\text{pressure}, \qquad p/p_0 = f_1(\eta)\, R^{-2}$$

$$\text{density}, \qquad \rho/\rho_0 = \psi(\eta)$$

$$\text{velocity}, \qquad u = R^{-1}\, \varphi_1(\eta) \ .$$

The assumptions hold for moderately strong shock waves. As an assumption of constant specific heat is made, the results should not be very accurate where dissociation takes place. However, Taylor observed a surprisingly good agreement between theory and experiment for very intense explosions. The neglection of heat conduction and radiation should also make the equations less accurate for very intense waves. The equations for the flow behind a cylindrical shock wave are:

$$\frac{\partial u}{\partial t} + u \frac{\partial u}{\partial r} = -\frac{1}{\rho} \frac{\partial p}{\partial r} \qquad \ldots (1.4.2)$$

(equation of motion)

$$\frac{\partial \rho}{\partial t} + u \frac{\partial \rho}{\partial r} + \rho \left(\frac{\partial u}{\partial r} + \frac{u}{r} \right) = 0 \qquad \ldots (1.4.3)$$

(equation of continuity)

and

$$\left(\frac{\partial}{\partial t} + u \frac{\partial}{\partial r} \right) \left(\frac{p}{\rho^\gamma} \right) \qquad \ldots (1.4.4)$$

(Equation for thermodynamic process of the flow)

u, p, ρ are the velocity, pressure and density of the flow at radius r and time t. γ is the ratio of the specific heats.

Substituting the similarity assumptions, the decay law for the radial velocity of the shock wave can be obtained:

$$U = \frac{A}{R} = \frac{dR}{dt} = 0.505 \left(\frac{E}{\rho_o}\right)^{\frac{1}{4}} t^{-\frac{1}{2}} , \qquad \ldots (1.4.5)$$

where A is a constant having dimensions of length times velocity. Similar expressions can be obtained to describe the pressure and temperature of the wave.

1.5 MEASUREMENTS OF WAVES IN SOLIDS

Since the second world war, work has been carried out on the determination of the equations of state by the study of the propagation of shock waves in solids. The dynamic compression of the medium affords higher pressures than had hitherto been available and with much less cumbersome apparatus than that which is required to produce pressures of the order of 0.3 megabars statically [13,14,18]. The first studies were made on metals [16]. Walsh and Christian [15] applied the Rankine-Hugoniot treatment with shock wave pressures of up to 100 kilobars. Before such an approach is possible, some basic assumptions must be made.

The typical shock pressures are many hundreds of times greater than the bulk strength of the materials, and a type of equation of state for a fluid is applied. In this case an unspecified functional relationship between P, V and T can be considered to represent the metal adequately. These assumptions avoid treatment of effects due to the rigidity of the material, and shear effects play a negligible part in the description of the state of the metal at that pressure range. When the shock wave is reflected at the edge of a sample solid, then the measurement of the shock wave velocity and the free surface velocity gives adequate

data for the application of the first two Rankine-Hugoniot equations. The particle velocity in the shock front can be deduced from the measured free surface velocity. This velocity results from normal shock wave reflection at the free surface. There must be zero pressure difference across the free surface boundary, which requires that a wave must be reflected with equal amplitude but opposite sign. The conditions give the surface a velocity approximately twice the particle velocity in the shock front[17].

Measurements of shock and free surface velocities in perspex can yield, by the same technique, the Hugoniot equation of state for that medium. Shock pressures of up to 13×10^{10} dynes/cm^2 give a maximum shock velocity of 5.47 mm/μsec. A typical shock velocity in perspex is of the order of a few millimetres per microsecond, and the compression ratio $\sim$ 1.25 - 2.

A variety of techniques have been used to detect the shock waves[11,19-23]. Pack (1948)[24] has used a system of electrical pin contacts which are brought together by the distortion of the metal produced by the shock wave. Using this technique he has made straight determinations of shock wave velocities in both steel and lead.

Streak cameras can be used[25] to show the acceleration of the shock away from an explosion while the wave gains energy. The use of a framing camera[26] (for example a fast image converter can produce framing rates of up to 10^8 sec^{-1}) gives a more complete picture of the form and distribution of the wave propagation.

In order to produce a sharp photograph which 'freezes' the movement of the shock wave, a framing rate with exposures of less than a microsecond is necessary. This length of exposure is obtainable with a Kerr cell[27], though in the past, camera systems have made use of a battery of single

Kerr cell cameras, and the cinematic effect has been built up from such a series of separately triggered devices. The image converter is a more adaptable camera.

The 'open flash' method of photography[28] obviates the need for either of these pieces of equipment. In this system the length of the exposure is regulated by the speed of an illuminating flash, while the camera shutter is held open. A suitable bright and fast-switching light source could be a pulsed laser. The typical output from some commercial dye lasers is just about exactly the 1.0 μsec pulse which is required to 'freeze' the motion of the shock wave, but in most of these lasers the recovery rate is not sufficiently fast to allow more than a single exposure in the time scale defined by the shock wave velocity.

The use of a single light pulse both to produce the shock wave and to detect it, has several advantages over a system where the detection light pulse has to be synchronized to the explosion. Such a system completely eliminates the problems of jitter, the delay time between the explosion and the shock wave photography is measured directly from the optical delay path travelled by the photographic part of the beam. A Q-switched ruby laser which is powerful enough to produce shock waves, typically has an output pulse length < 20-30 nsec., which is easily within the pulse length limit necessary to produce a clear picture.

1.6 OPTICAL METHODS OF SHOCK DETECTION

Although shock waves of sufficiently great intensity (> 10 atmos.) are directly visible due to the associated radiation[10,25], moderately strong shock waves can be rendered visible by a variety of techniques. The shock wave produces in the material a significant change in refractive index, and schlieren[29] and shadowgraph[30] techniques are applicable. These techniques require a uniform illumination over the complete area of

interest and the wave is photographed as a negative. The reflection of light from the shock induced refractive index increase[31,32] is of specular nature indicating the smoothness of the front. By this method, shock front densities[22,33,34] can be determined as well as velocities[35].

Probing the shock wave with polarized light[36] and a crossed polaroid system produces a positive image of disturbance if the wave produces any optical rotation. In liquids this is nearly always the case. In an optically active solution such as a glucose solution, the rotation is dependent on the sugar concentration which increases with the pressure of the shock wave. Initial optical activity is not, however, vital in order that the shock wave produces optical rotation, for in normally optically inactive media, double refraction can be induced by a number of mechanisms.

The presence of large velocity gradients behind the shock front produces an effect similar to the Lucas[36,37] effect in ultrasonics, where the large pressure in the waves induces an anisotropy in the material. Many materials which show no Lucas effect in ultrasonics undergo this deformation when subjected to very much larger shock pressures. Larger molecules can be both distorted and aligned by the presence of the velocity gradient[38,39].

Birefringence induced by some of these mechanisms has been observed in water[36] as well as in methane and a variety of larger organic molecules[40], none of which show any optical activity in the presence of ultrasonic waves.

In practice. strong shock waves can be photographed by the combination of reflection and refraction which is bound to take place if the disturbance is of sufficient intensity. David and Ewald[40] have photographed shock waves in water with shock pressures of up to 100,000 atmospheres.

In transparent solids, the same general principles for shock wave photography apply as for liquids. The birefringence in perspex caused by the induced anisotropy where it is strained, is well known and has long been used for making stress patterns visible with static deformation. A number of other plastics and glasses show this phenomenon[31] when stressed. Under dynamic compression the mechanism is slightly different, because in the presence of strong shock waves the elastic limit is exceeded and the birefringence is caused by plastic compression and flow. The shear stress in the solid can be ignored. This birefringence allows photography of shock waves in perspex[41,42] provided that a short enough light pulse is available.

Fröngel et al[43] have used schlieren techniques coupled with a high speed stroboscope[44] in order to produce multiple photographs of shocks using the shock induced optical strain.

CHAPTER II

MECHANISMS FOR THE PRODUCTION OF SHOCK WAVES

2.1 SURVEY OF METHODS

2.1.1 Chemical Explosive

Although the experimental work on this thesis does not include the use of chemical explosives, these are historically by far the most important means for the artificial production of shock waves, and must be placed first in any survey of techniques. In the past, mainly on account of the military applications, they have received most attention.

Detonation within a mass of chemical explosive is not instantaneous. If a fraction of the explosive is ignited, the combustion produces a shock wave which heats the remaining explosive as it passes through it. When the shock wave is sufficiently strong, i.e. if the energy produced per unit volume of explosive is great enough, then the wave will ignite the material as it passes through it, and gain energy as it travels. Behind the shock wave the gas burns, and if the time for all the gas to be burnt $= \tau$, then the width of this zone $= V\tau$. For a sufficiently fast shock wave, the wave front is a discontinuity zone of burnt and unburnt material, such a surface is the detonation wave. Different detonation shapes can be achieved by using explosives of different combustion rates.

2.1.2 Nuclear Explosion

Unlike the shock wave produced by chemical explosives, a nuclear explosion is characterised by being practically instantaneous. The nuclear explosive can be considered as a point source of energy, and the resulting blast wave does not contain the debris to be found in the wave from conventional explosives. Nuclear devices can contain $\sim$M tons equivalent of TNT. This results in considerable heating in the intense shock front during the early stages of its formation. The consequence

is that with blast wave pressure of 10 atmos. and greater, considerable energy is lost in heat. At 20 atmos. as much as 45% of the energy is wasted in heat, and this means that the atomic bomb is only half as efficient as a conventional bomb in which the initial explosion is spread over a larger volume.

Taylor's similarity equations and analysis can be applied to such an explosion with remarkable accuracy. Comparison of photographs of an atomic blast[45] and the theoretical predictions shows that over the first 200 m, $(R^{\frac{5}{2}}t^{-1})$ was a constant. This constant enables a calculation of the initial energy of the explosion to be made. In this case the explosive energy was equivalent to ~20K tons of TNT.

The characteristic mushroom shaped cloud produced by an atomic explosion is not a shock phenomenon. It is produced by the convection as the volume of very hot gas left behind after the explosion rises through the atmosphere. This low density air bubble can rise with a vertical velocity of ~35 m/s before it is broken up by the turbulent mixing of the hot air with the surrounding cold air. The measured velocity also corresponds exactly to the theoretical rate of rise.

2.1.3 Spark Shock Formation : Thunderclap

Mathematically this can be treated similarly to a nuclear explosion. Detonation is almost simultaneous along a line. Taylor's analysis has been modified by Lin (1954), to give a relation describing the radius of the strong cylindrical shock produced by a spark as a function of the time (t) :

$$R = S\left(\frac{E}{\rho_o}\right)^{\frac{1}{4}} (t - t_o)^{\frac{1}{2}} . \qquad \ldots (2.1.1)$$

This function only holds before the point when the shock wave has decayed so the pressure ratio across the shock is no longer large (~10). For weak

shock waves the density ratio across the front is no longer constant and his similarity assumptions are not followed.

Any mechanism whereby energy release is axially instant and simultaneous can be described by this formula. One typical process is the thunder shock wave caused by a lightening strike.

2.1.4 Hypersonic and Supersonic Flow

A supersonic projectile moving through the atmosphere pushes ahead of it a shock wave, because the pressure wave which the missile produces in the atmosphere is never able to get away from the body. For supersonic (Mach number $1 \rightarrow 5$) bodies a conical wave is produced with a large angle to the body.

In the case of hypersonic missile ($M > 4$) a strong shock wave is produced which attenuates as it moves away from the body, a long way from the nose it degenerates to a wave with a small angle. For sufficiently high Mach numbers the axial flow may be neglected[12] and the similarity solutions for a cylindrical shock wave apply.

The energy transferred to the atmosphere by the shock wave gives the aerodynamic drag of the missile.

2.1.5 Shock Tubes

The shock tube is at present a widely used tool for studying the chemical physics of gases at high temperatures. When a cold gas is heated by a shock various processes take place within the heated gas (e.g. excitation of molecular vibrations, dissociation, ionization, etc.) the extent of these processes depends on the temperature and density.

The common form of classical shock tube (as distinct from an electromagnetic shock tube) consists of a long tube with circular or rectangular cross-section. The tube is divided into two parts by a thin diaphragm situated across the tube.

The pressures in the two sections of the shock tube are greatly different. The low pressure chamber is filled with a test gas at a pressure usually of the order of a few centimetres of mercury.

On the opposite side of the diaphragm the high pressure chamber is filled with the driver gas with a pressure of tens or hundreds of atmospheres. Typical shock tube dimensions would be such that the tube is several metres long with the inside diameter of a few centimetres.

The shock tube is operated by breaking the diaphragm so that the high pressure driver gas flows into the long low pressure chamber. The pressure distribution is shown in Fig.2.1. A shock wave develops and is propagated into the low pressure gas, while a corresponding rarefaction wave moves through the driver gas[46]. Fig.2.1 shows the pressure and temperature distribution as the wave moves down the tube and is reflected from the end.

The maximum shock velocities obtainable by this technique are limited, and newer types of shock tubes have been introduced. These operate on different principles. Fowler[47] has constructed a T-shaped tube in which the gas is rapidly heated by electrical discharge across electrodes in the horizontal bar of the T. The heated gas is expelled at high velocity into the 'vertical' part of the T, and a shock wave is created ahead of it.

Kolb[48,49] has produced a T-tube in which the plasma is accelerated by a 'magnetic' piston. Other shock tubes using magnetic acceleration have been described by Kholev and Poltavchenko and Josephson, and many variations exist.

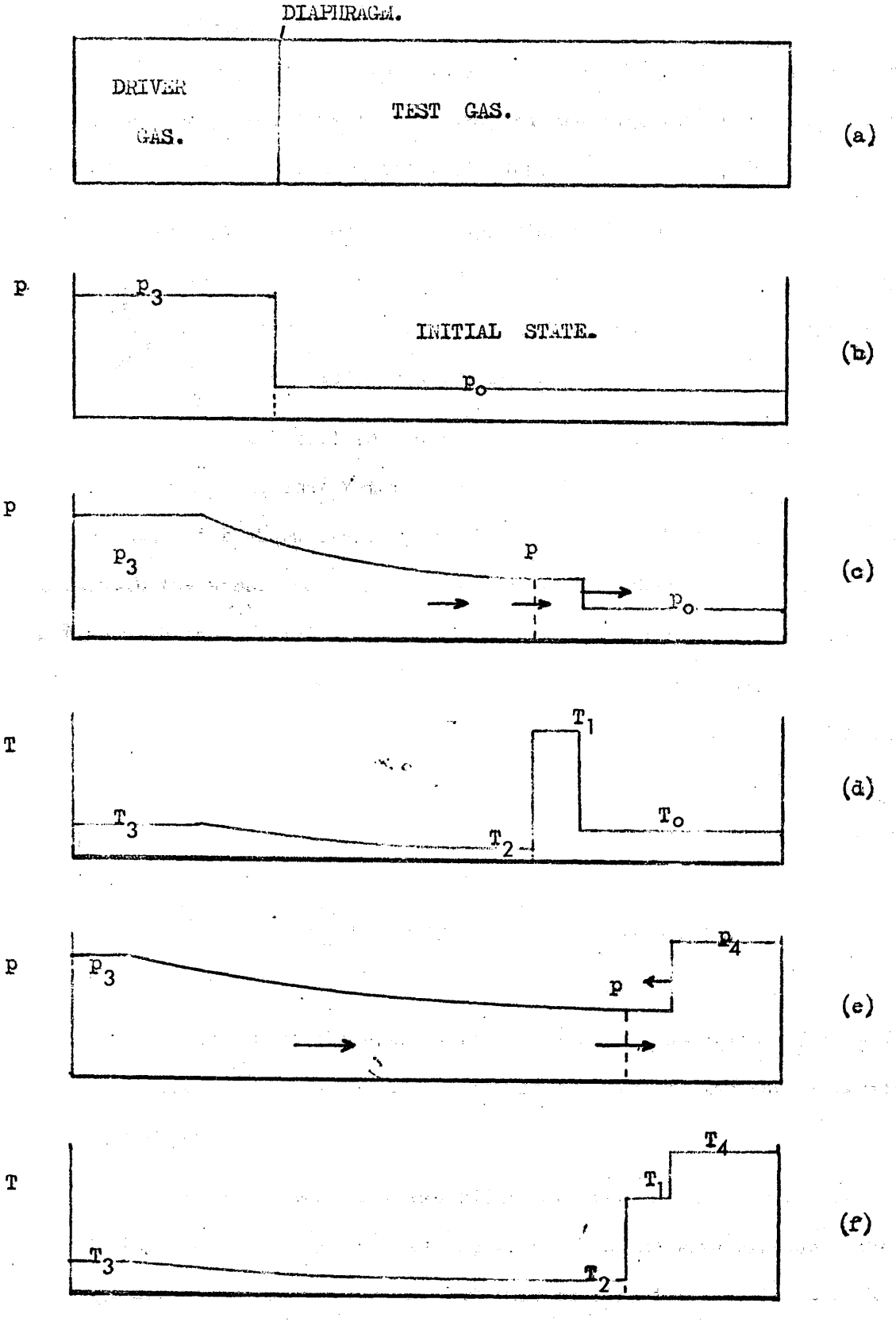

PRESSURE AND TEMPERATURE CHANGES INSIDE A SHOCK TUBE.

FIGURE 2-1.

2.1.6 Exploding Wires

Early experimental work by Anderson et al[50,51] on exploding wires was concerned primarily with the study of the spectrum emitted by the high pressure vapour produced by the explosion.

The typical parameters of exploding wire experiments consist of a wire 0.5→5.0 cms in length and ≤0.1 cm diameter. The wire is exploded by electrical discharge with energy $\sim 10^2$ J dumped in the wire from high voltage (5-50 kV) capacitors in a low inductance circuit.

While it is still luminous, the shock wave can be photographed directly by conventional rotating mirror camera[52-56]. After about one micro-second the shock front is completely separated from the contact surface with the wire, and is no longer luminous. Comparison of shock wave motion with the predictions from Lin's theory shows that during the early stages of its propagation, the shock wave is still receiving energy from the discharge. The shock wave trajectory obeys more accurately the Lin mathematical formulation when it is no longer gaining energy[52]. A plot of $(2R)^2$ against t produces a straight line graph for a period of several microseconds after the first microsecond, but Lin's solution with its assumption of instantaneous energy release cannot apply completely accurately in this case.

Correlation of the optical and electrical measurements during the wire explosion[25] shows the efficiency of the process for the production of shock waves.

A peripheral arc is formed after the wire has started to expand and during the rapid explosion of the wire. As the wire explodes, the voltage across it reaches a peak, but this rapidly falls as the arc is established. Most of the energy is deposited in the wire during the time of the voltage peak. A second, axial, arc can occur after the wire

explosion has got under way and the material density along the axis is reduced sufficiently. This arc will illuminate both the outward going shock wave produced by the expanding wire material and the inward going one[56]. If the rate of energy deposition is not sufficiently great, then the initial peripheral arc may not strike and there is a certain 'dwell' time before the wire absorbs enough energy for it to explode. If the wire is large enough the discharge energy may be insufficient to produce complete vapourisation of the wire, the explosion may then be caused by the wire forming molten droplets with connecting arcs. The droplets are thrown off as a shower of liquefied ~~wave~~ wire material[57].

The ease with which a wire can be exploded[58,59] depends not only on its dimensions, but also on its sublimation energy and mechanical strength. Thus, a wire of constantan explodes in less time and at a lower energy than a copper wire of identical dimensions.

The most efficient discharge takes place when the capacitor is completely discharged during the explosion due to the current pulse through the wire, i.e. when there are no re-strike phenomena[60]. Generally, however, only about one third of the energy from the capacitors is transferred into the shock wave[61-63]. Smaller diameter wires[64] are generally more efficient shock wave ~~products~~ produced than thick wires. The wire itself usually has a resistance comparable to that of the spark-gap switch which is used to control the circuit. Approximately half of the energy discharged from the capacitor is thus dissipated in the spark-gap, another one sixth of the energy is used in the production of the radiation accompanying the exploding wire, this leaves approximately one third of the energy stored in the capacitors which is transferred into the shock wave.

Taking into allowance the energy losses in the switch and assuming complete vapourisation of the wire, McGrath[65,66] has measured shock wave

pressures from exploding wires, and by comparison with the data for chemical explosives (TNT), has produced a scaling factor so that the equivalent charge of TNT (measured in 'μ-pounds') can be calculated from the known electrical parameters of the circuit and the latent heats of the wire.

2.1.7 Impact Phenomena : Liquid and Solid Projectiles

At impact velcoities greater than ~ 400 m/s the damage effect of liquid and solid projectiles becomes very similar. The liquid drop will behave more like an elastic solid, although keeping its flow properties[67]. At typical ordinance velocities (~ 1,100 m/s) the impact produces two waves related to the elastic and plastic wave velocities in the target plate[68]. For given projectile and plate material the crater volume per unit projectile kinetic energy has been found to be constant[69] and a function of impact velocity[70,71].

For impacts in the hypervelocity (> 2,500 m/s) range[72] when firing aluminium projectiles at annealed steel plate targets, only one wave velocity has been detected. At this higher impact velocity, the relationship between crater volume on kinetic energy is still found to hold, although the disintegration of the hypervelocity projectile makes its recovery not possible.

2.1.8 Development of Non-Linearity : Breaker Effects

According to Stokes[1] shock waves may develop from a normal compression wave because of the non-constant compressibility of the medium. In this case the changing velocity profile is analogous to the effect of the tidal bore[73,74].

In this case the tidal movements are propagated faster, the deeper the water involved. Thus the difference of water level between low and high tide can be propagated up a river with the rear parts of the wave catching up the forward as the front of the wave moves into shallower

water. In most cases the frictional effects of the river bed attenuate the wave, but this effect can be lessened as the river becomes narrower higher upstream. In some cases bores of several feet can form[74]. The turbulence in the front of the bore dissipates its energy.

2.1.9 Energy Absorption by Particles in a Laser Beam

The power density at the interaction area and the nature of the surface of the particles are important in this case. For low power densities with pulsed lasers which are not Q-switched, damage may be produced, but the critical flux density[75] is $\sim 10^8$ W/cm^2. Much work has been carried out on the absorption of laser radiation by opaque surfaces on large metal targets[76-83]. The results of this research can be easily applied to the case of smaller particles.

Below the critical flux density, the thin layer on the surface of the material which is absorbing the radiation, undergoes a phase transformation provided sufficient energy is supplied. At very low power densities the surface under irradiation may melt, but nearer the critical power the surface is evaporated.

For low power levels, the heating effects can be treated by ordinary thermodynamics and the associated shock wave as the metal vapour plume expands into the air has been photographed both by conventional high-speed methods and by using a laser to give a series of Q-switched light pulses. An associated acoustic wave has also been photographed[84,85]. The metal vapour plume is generally transparent at low temperatures and so does not interfere with the incoming laser beam.

Above the critical flux density, experiments have been performed up to the 10^9 W/cm^2 range. This has necessitated the use of high powered Q-switched lasers.

The use of the Q-switched laser results in extremely fast rates of energy deposition so that by the time the surface of the material explodes, it is in fact no longer receiving any energy from the laser pulse. The total quantity of the energy can be delivered to the surface in a pulse < 20-30 ns long, thus although the plume of vapour emitted from the material is not necessarily transparent to the laser beam at these energies, it in no way affects the absorption of energy by the surface[86]. Measurement of the plume velocity in this case[87] shows that it is very different from the plume produced at lower powers. Light is absorbed by metals by raising electrons to higher energy states in the conduction band[88]. The mean free time between electron collisions in a good conductor is $\sim 10^{-14} - 10^{-13}$ s, thus during the period of the input light pulse ($\sim 10^{-8}$ s) there will have been many collisions, so that the energy absorbed by one electron will be spread around the metal. Within the area at which the light is absorbed, the transfer into heat can be considered to be instantaneous. Ready[89,90] found that the material beneath the surface reached vapourisation temperature before the surface had absorbed the latent heat of vapourisation. This results in a high pressure pulse, and superheating of the underlying material until the temperature rises above the critical temperature[91,92]. A fast, hot plasma jet is emitted in the direction of the light source[93], though within a large solid angle[94,95]; by reaction, a shock wave is generated which passes into the undisturbed part of the solid. Some liquid metal may also be ejected, the result is a crater scoured out on the surface of the target.

This process can easily be applied to small particles ($\sim 10^{-2}$ cm in diameter) when it is seen that the heat flow is rapid enough for the whole of the particle to reach vapourisation temperature and thus lead to superheating at the centre of the particle, while the latent heat of vapourisation is absorbed at the surface.

2.1.10 Focused Laser Energy Absorption from a Q-Switched Pulse

The mechanism of shock wave production by dielectric breakdown induced in a liquid at the focus of a Q-switched laser has been examined by a number of workers[28,96-98,102]. Shadow photography in conjunction with spark light sources triggered by the incoming laser light has been used, but the technique of passing the light beam used for shock wave production around a delay path after production of the wave, and re-using it to photograph the waves, gives shorter delay times between wave production and photography.

Average shock velocities of up to 0.70 cms/μs can be produced, though coupling is better if the laser beam is focused on to a metal target (cf. preceding section).

Impurities play a major role in laser induced electrical dielectric breakdown processes. The addition of only minute quantities of Al_2O_3, for example, can lead to multiple points of breakdown along the axis of the laser beam, even away from the focal point[97]. To ensure that the shock waves are produced solely by breakdown and not by the absorption of light energy by very fine particles, it is essential that very pure liquids are used. It is also necessary to ensure that the liquid itself does not absorb light of the wavelength used.

Threshold values for breakdown show a wide range[98]. Breakdown threshold has been observed by Roach to vary from 4MW to 33MW laser output power over a range of eight organic liquids. The breakdown could be observed visually as a glowing bubble of gas is produced, but it is also accompanied by an audible crack.

In the case of a liquid where light absorption takes place, an axial cylindrical acoustic wave is generated[97], indicative of a fairly uniform absorption along the path of the beam. When a ruby laser is

used for retinal coagulation in the eye[99-101], there is almost certainly such an associated production of pressure waves in the region of interaction.

2.2 DISCUSSION AND COMPARISON OF TECHNIQUES: ISOLATION OF AN EXPLOSION (DEBRIS CONFINEMENT)

The methods of shock wave production which are most easily used in the laboratory are chemical explosives, the spark shock, exploding wires and the laser produced phenomena. We are concerned here with exploding wires and laser produced shock waves. The production of shock waves from laser induced dielectric breakdown and by the absorption of laser light energy by microscopic particles can be likened to a nuclear explosion on the microscale, in so far as the explosion produces little or no debris and a finite quantity of energy is effectively dumped at a mathematical point almost instantaneously. In this case the Taylor similarity theory for spherical shocks is applicable although the wave is not strong enough to lose much of its energy through radiation. In the case of the method of evaporation of material from a metal target, the Taylor theory cannot be applied because of the absence of spherical symmetry, also the shock wave may gain energy from the metal vapour during the initial stages of its creation. When the shock wave has reached maximum strength, and as it starts to decay, the normal Rankine-Hugoniot equations may be applied to the motion of the plane shock wave which is produced normal to the surface of the target. In the case of shock wave production by evaporation from a target, the associated metal vapour 'debris which is produced, may hinder the optical measurement of the outgoing shock wave.

Both lasers and exploding wires as well as spark sources, have the advantage that, as well as being on the micro-scale, the amount of energy being provided for the shock wave production is easily controlled and measured. Dielectric breakdown produces a highly uniform spherical shock,

whilst exploding wires and spark sources produce highly uniform cylindrical waves. The spark shock source has already been shown to obey Lin's theory for cylindrical waves. When it has passed its maximum strength, and is in the process of decay, the exploding wire produced wave also follows Lin's calculated motion. During the formation of the shock wave from a wire the shock wave gains energy over a short period of time ($\sim \mu s$) but the energy is applied uniformly and simultaneously along the axis of the wire.

As is the case with metal evaporation by a laser, the exploding wire also produces debris. This debris, which consists of metal vapour, radiates energy over a relatively long period of time ($\sim$ms) . If the 'open flash' exposure technique of photography is to be used to photograph the shock wave, then the presence of the hot, radiating metal vapour will obscure the shock wave and it becomes necessary to contain the wire in some form of light-proof box which will allow the passage of the shock wave, but not the associated wire vapour and light.

In order to produce an efficient coupling of shock wave energy between two media, it is necessary for the shock wave velocity to be similar in each medium. If the wire is exploded in air, there will not be a very efficient transfer of shock wave energy into a neighbouring solid. It is therefore advantageous to explode the wire in a liquid and surround this axially by a solid container with similar mechanical properties. It has already been shown that because of the high pressure created by shock waves in solids, the solid is deformed plastically by the wave, and the effects of shear stress can be ignored. Thus the solid acts similarly to a liquid in these circumstances and typical shock wave velocities in solids are not far different than for liquids. It is necessary, however, for the solid to be such that it will flow plastically, and is not liable to brittle fracture. For shock wave transmission from one solid to another the same criteria apply, and an intimate contact between the two solids is necessary.

CHAPTER III

DESCRIPTION OF APPARATUS FOR INITIAL SHOCK WAVE STUDIES

3.1 DISCHARGE CIRCUIT FOR EXPLODING WIRE

For the initial investigations the exploding wire technique was used as a shock wave source. This requires the rapid dumping into the wire of enough electrical energy to vapourize the wire completely. The method used, the discharge of electricity from storage capacitors, requires that the capacitors are charged to a high voltage in a low inductance circuit if the discharge is to be sufficiently rapid to vapourize the wire.

The available capacitor (Bonar Long Electronic Rapid Discharge) was rated at 10 μF and 20 kV. In use, the capacitor was never charged above 11 kV so that the contained energy was always less than 605 J. For observations of the explosion of the wire, a range of lower energies was also used (~80 J at 4.0 kV in the capacitor) to produce an explosion of molten wire material. The 10 μF capacitor was later replaced by three storage capacitors of 38 μF rated at 8 kV. The series capacitance of these three was 12.5 μF.

The discharge circuit is shown in Fig.3.1. The Brandenburg power supply (Type MR SO/RA) produced up to 1.0 mA at 50 kV and the recharging of the capacitors took some minutes.

A 40 Ω dump resistor was permanently in parallel with the wire. This ensured the complete discharge of the capacitor every time, by dissipating the surplus energy after the wire had blown. A high resistance potential divider 100:1 ratio and 22.2 MΩ was also in parallel with the exploding wire, and was used to measure the instantaneous discharge voltage across the wire during the course of the explosion.

The discharge circuit was switched by a triggered air spark-gap switch. The spark-gap had a typical resistance of ~3 Ω when in the 'on'

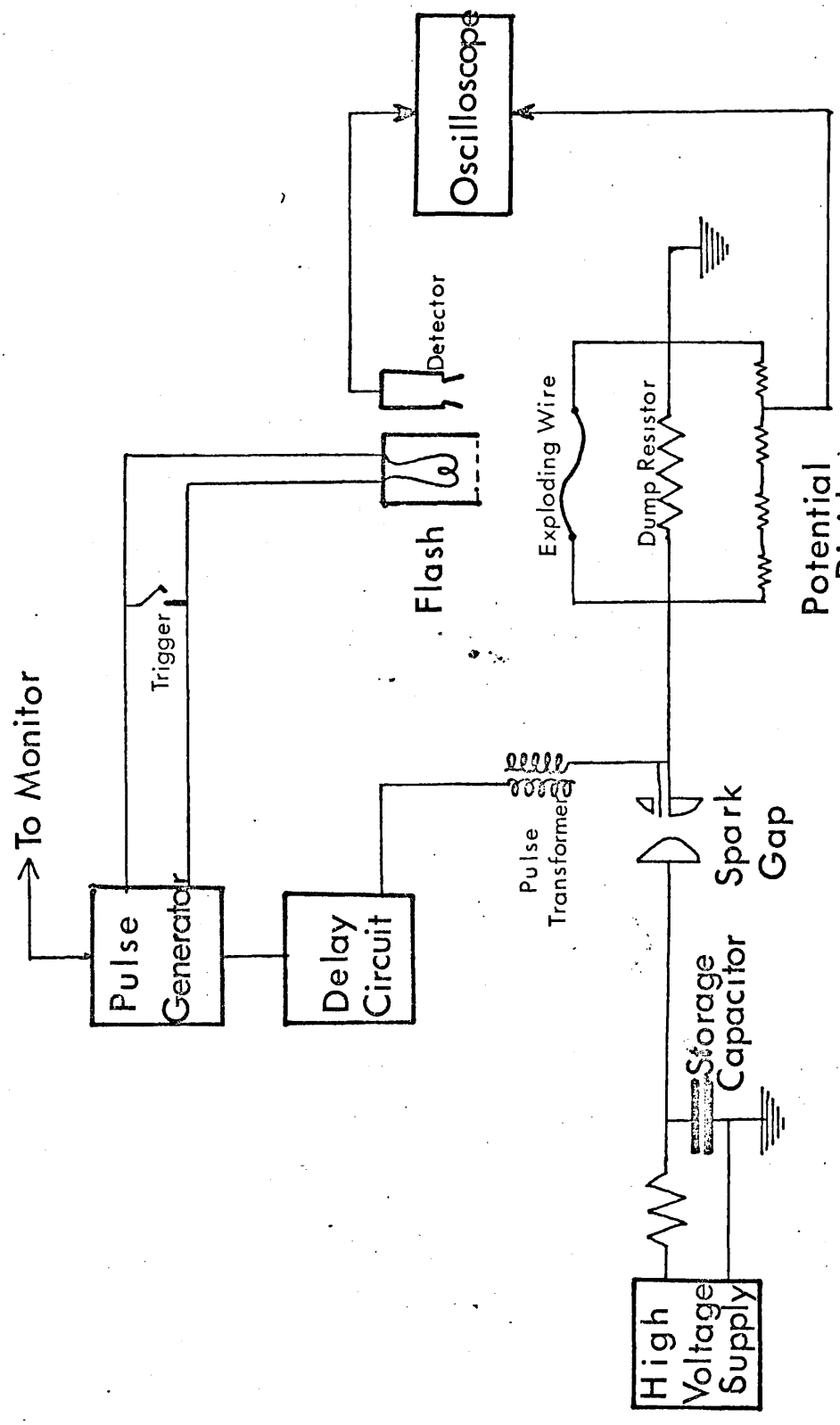

Fig. 3-1.

Discharge Circuit for Exploding Wire.

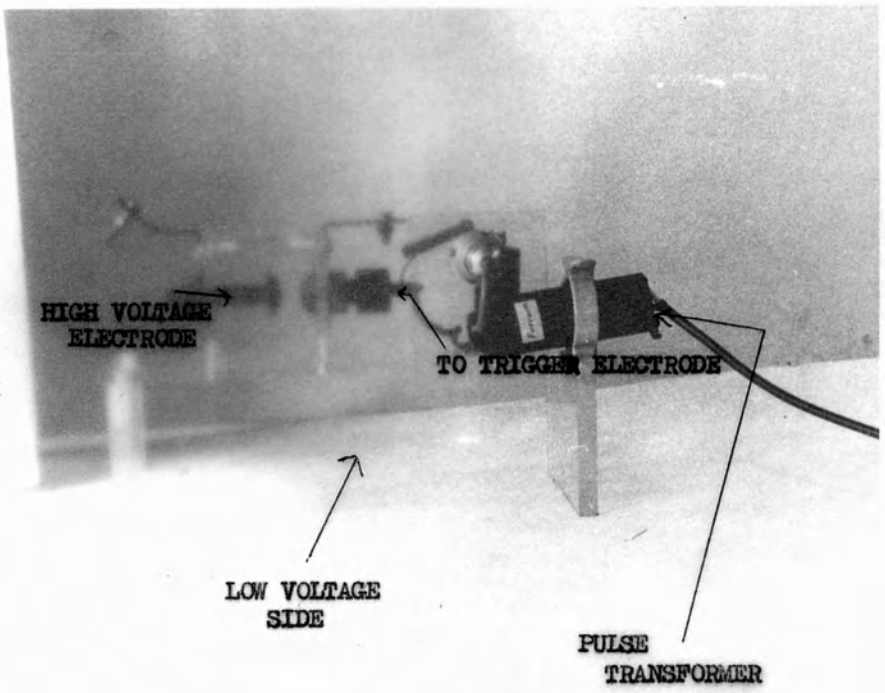

SPARK GAP SWITCH.

FIGURE 3-2.

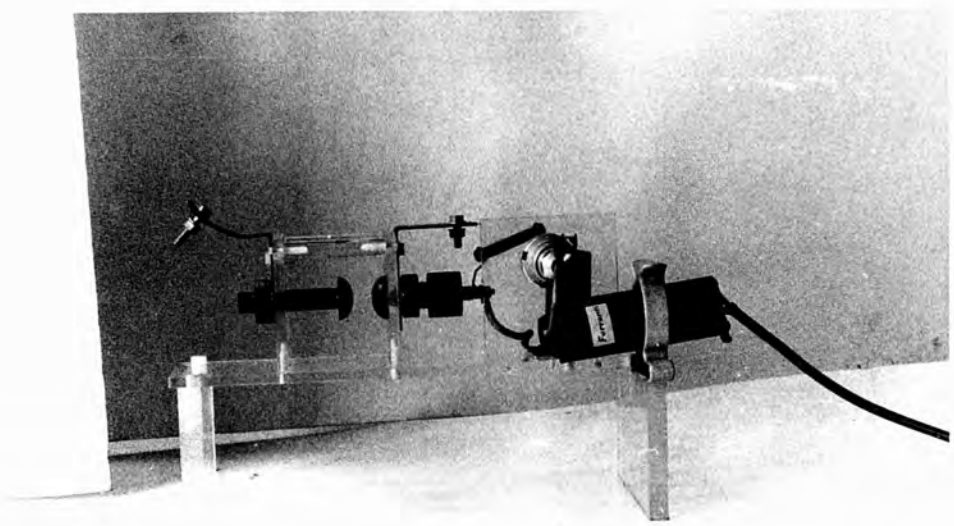

condition. The tungsten triggering electrode was inside and concentric to the electrode on the low voltage side of the switch (Fig.3.2). The wire to be exploded was also positioned on the low voltage side of the switch and was thus held safely at earth potential until the discharge.

The output thyratron in the pulse generating circuit switches 150V in 50ns. This pulse is passed through a pulse delay circuit before entering the Ferranti P.T.60.(100:1) pulse transformer.

The inductance of the discharge circuit was kept to a minimum and the discharge time $\sim 5\mu s$. The voltage was monitored on one beam of a Telequipment dual beam oscilloscope triggered by the discharge. The second beam of the oscilloscope was used to monitor the photoflash used to illuminate the shock waves.

A number of wires were exploded. At low voltages for liquid drop observations 28 S W G steel piano wire was used as well as 29 S W G 'Eureka' (Constantan : 60% Cu, 40% Ni alloy). Eureka wire has a very much lower melting point and latent heat than steel wire and so the energy required to explode it is greatly reduced.

3.2 EXPLODING WIRE CAVITY

In order to study the wire explosions directly, a dural cavity of cylindrical cross-section was constructed to contain the fragments of the exploded wire. The internal diameter of the cavity was $4\frac{1}{2}$" and outside diameter 7", its depth was 2". The top and bottom of the cavity were sealed by $\frac{1}{4}$" thick plate glass windows 6" diameter and clamped tightly on to neaprin (neoprene) O-rings recessed on the end of the cavity cylinders in order to make the container waterproof.

The axis of the cavity was set vertical, and the leads to the two electrodes holding the wire were led through the walls by vacuum tight

seals. The wire was clamped vertically between the two electrodes whose separation was $\frac{3}{4}$". The electrodes were extended into the cavity so that the wire was held 2.5 cms from the wall of the cavity thus permitting a uniform explosion.

The light from the wire as it was about to explode was shielded from the camera by an aluminium plate placed between the camera and the top electrode across the line of axis of the wire. This shield, which was removable, also protected the windows from molten particles of wire thrown up at the ends of the wire where the explosion is not cylindrical.

Provision was made in the cavity so that it could be filled with liquid through inlets inset into the wall of the cavity adjacent to the electrode mountings, and thus out of the 'line of fire' of exploding wire particles. When the cavity was filled with air, these acted as a pressure release.

When the cavity is filled with water, the main reflective surface for any shock waves travelling through the liquid is at the external face of the cavity wall, at which point observation of the shock waves is not possible. For this reason the cavity was chiefly used to contain wire explosions at low energies in air.

In addition to the wire containing cavity just described, a large box 2'×2'×3' was constructed from hardboard, and the electrodes to hold the exploding wire were mounted inside with the wire mounted vertically. The top of the enclosure was constructed with a glass window so that the camera could be mounted above, to photograph an area of about one square foot about the wire. This enclosure was of such a size that the droplets of wire hitting the wall and being bounced back could be neglected. The wire was positioned near the centre of the enclosure so that by the time wire particles reached the walls they had slowed to a velocity with

insufficient energy for them to return, also the coefficient of restitution of the matt face of the hardboard was considerably less than that of the dural cavity.

By placing a small aperture (0.5 cms diameter) about 2" from the wire it was possible to select droplets travelling in a chosen direction and aim them at a selected target which was mounted vertically inside the enclosure at a distance of ~10" from the wire. Some targets were placed immediately adjacent to the wire in order to receive particles at their maximum energy.

3.3 WIRE DEBRIS CONTAINMENT: THE SHOCK WAVE GENERATING CYLINDER

The reasons for enclosing the exploding wire have already been covered in Chapter II, Section 2. In order to be able to view the maximum area of interest it is necessary for the cylindrical container surrounding the wire to have a small diameter. Also the electrodes leading into and supporting the cylinder must be kept small. An optimum cylinder size exists such that the cylinder has a diameter small enough not to interfere with the field of view, but not so small that it is not strong enough to contain the blast of the wire explosion.

The first cylinder to be constructed was designed to contain a 1.95 cm long wire. The internal diameter was $\frac{1}{2}$" and the external diameter 0.65". The electrodes holding the wire were held by a nylon insulator inside aluminium end caps which were screwed on to the mild steel cylinder with a screw thread. This was found to be insufficient to contain the pressure built up during the explosion, the screw thread being too fine. The replacement shock generating cylinder was constructed with $\frac{3}{4}$" outside diameter and $\frac{1}{2}$" internal diameter (see Fig.3.3). The screw thread to hold on the caps was strengthened to a coarser thread which was strong enough. The wire was mounted axially within the cylinder by threading it through

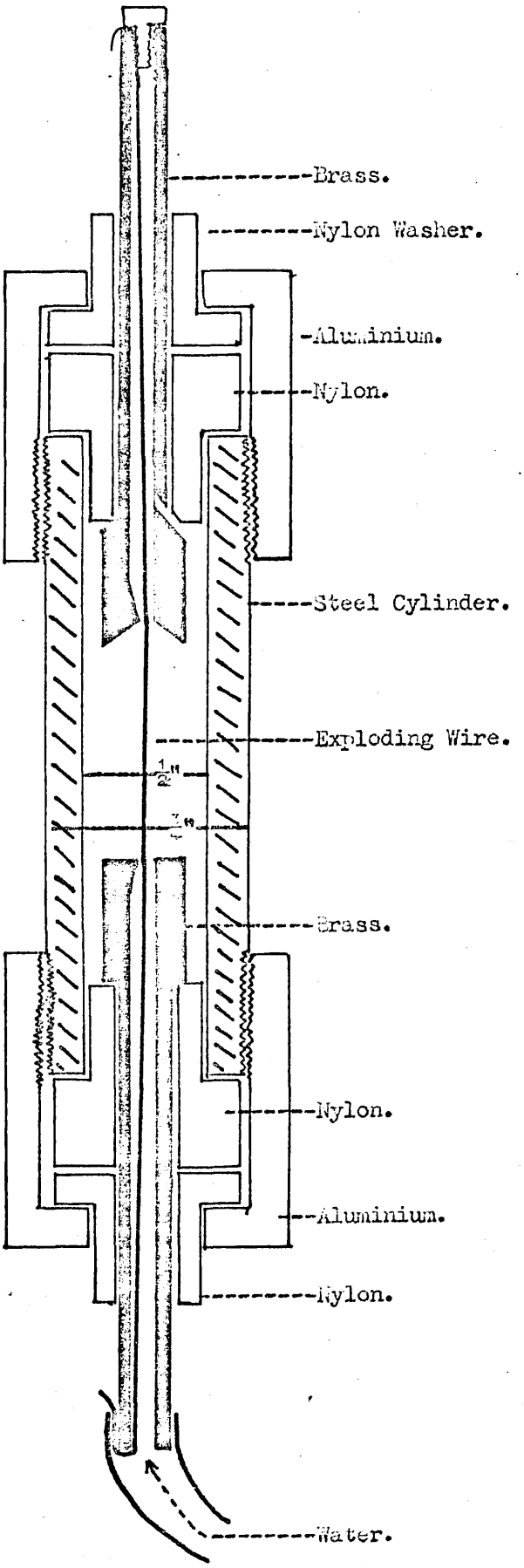

SHOCK WAVE PRODUCTION - WIRE CONTAINMENT.

FIGURE 3 -3.

the 4 mm outside diameter hollow brass electrodes. The electrodes were so shaped that the wire, when fed through the lower electrode, was directed into the narrow hole in the end of the second (top) electrode. In this way, wire replacement was made possible without the necessity of dismantling the container. When the wire was held in position, the container was flushed out by a stream of water entering through the lower electrode and leaving through the top. The electrodes were constructed to project into the cavity so that the blast from the exploding wire was kept away from the ends of the cavity and did not damage the insulating material between the electrodes and the outer steel casing. The electrodes themselves were in the path of the exploding wire and thus liable to damage. This necessitated the occasional remaking of the electrode tips where the wire blast had distorted the brass.

Nylon spacers around the electrodes on the outside of the cylinders ensured that there was no electrical breakdown between the cylinder and its mountings. Sharp edges were avoided because of the high voltages of the discharges. Electrical breakdown was not a serious problem however, because the voltage was pulsed and not continuous. After the wire has blown, there is a possibility of current passing from the electrodes down through the body of the cylinder; this would in fact be an advantage in that it would help to dissipate any surplus charge left on the capacitors.

3.4 TRANSFER OF THE SHOCK WAVE INTO A PERSPEX PLATE

In order that shock waves are transmitted efficiently from one solid to another, it is necessary for the two surfaces to be clamped tightly together (cf. Chapter II, section 2). The outside surface of the shock wave generating cylinder described in the previous section was given a slight taper so that it was at its maximum diameter opposite the section receiving the blast of the exploding wire. In order to observe the stress

induced in perspex by the waves, a number of perspex discs each had a hole whose diameter is equal to the outside diameter of the cylinder, drilled through a point 2.5" cms from the edge of the disc, accurately perpendicular to the disc's surface. The discs were of a selection of chosen thicknesses, $\frac{1}{8}$, $\frac{1}{4}$, $\frac{1}{2}$, $\frac{3}{8}$ inches.

A number of methods were tried in order to ensure a tight fit between the steel cylinder and the surrounding perspex. By drilling a hole whose diameter was $\frac{1}{2}$" greater than the diameter of the cylinder, the gap was more easily filled in with perspex cement while the cylinder was clamped in position in the centre of the hole. This method was found to be unsatisfactory because the liquid cement shrinks by about 25% volume when it sets, and thus air bubbles form in the gap between cylinder and perspex.

The technique of forcing the steel cylinder in whilst cooled in liquid nitrogen was also used, but it was found to be unnecessary, as with accurate reaming, the disc can be force fitted around the cylinder so that the tightest fit is opposite the wire. During the course of a few explosions, the cylinder distorts plastically to give a very tight fit into the perspex. The stress induced in the perspex by the distortion of the cylinder was easily visible in polarized light, and was released with the removal of the cylinder. (See Fig.4.11).

The plates being adequately supported by the cylinder/plate interface, there was no need for any external clamps to help hold them. Thus the perimetral edge of each disc does not have to touch any other solid supports so that the reflection of the shockwave can be localized to the perspex air interface at all points around the circumference. To ensure that a uniform reflected wave was produced, the edge of each perspex disc was milled accurately so as to be perpendicular to the face of each plate, and polished to produce a smooth finish on the surface.

3.5 PHOTOGRAPHIC SYSTEM

During the initial investigations, two photographic techniques were used to record the wire explosion. As the wire explodes it reaches a very high temperature $\sim 3\times10^3$ °C and emits as broad band spectrum of radiation. Thus, for observations of the exploding wire, it is possible to view the wire by its own light. The liquid drops of wire were traced by their light paths, and all that was necessary to take a photograph was for the camera shutter to be held open during the period of time taken for the completion of the explosion.

The camera was positioned 1 m vertically above the wire, and looked along the wire, focused at the distance of the mid-point of the wire. A Kodak $\frac{1}{2}$-plate camera was used with Kodak P.300 plates and aperture at f = 8. This gave a sufficient depth of focus to cover the $\frac{3}{4}$" long wire. In order to cut reflections from the lower window of the cylindrical observation cavity, it was covered by a layer of black paper during this type of photography. In the larger hardboard enclosure no such precautions were necessary.

In order to produce photographs of the shock waves produced in perspex, the birefringence induced in the perspex was observed by placing the disc/cylinder combination between crossed polarizers (see Fig.3.4). In the normal unstrained condition only a small background radiation could pass through the system from the flashlight. During the passage of a shock wave, the birefringence in the perspex allowed passage of light through the system in the areas corresponding to the stress. The 'open flash' method of photography was used.

A very fast flashlight was unavailable, but a Rollei type E.55 (later replaced by type E.66) was used to give a 1 ms flash. This flash length is over three orders of magnitude longer than that required to produce a sharp picture. A typical shock wave with velocity $\sim 5\times10^3$ m/s

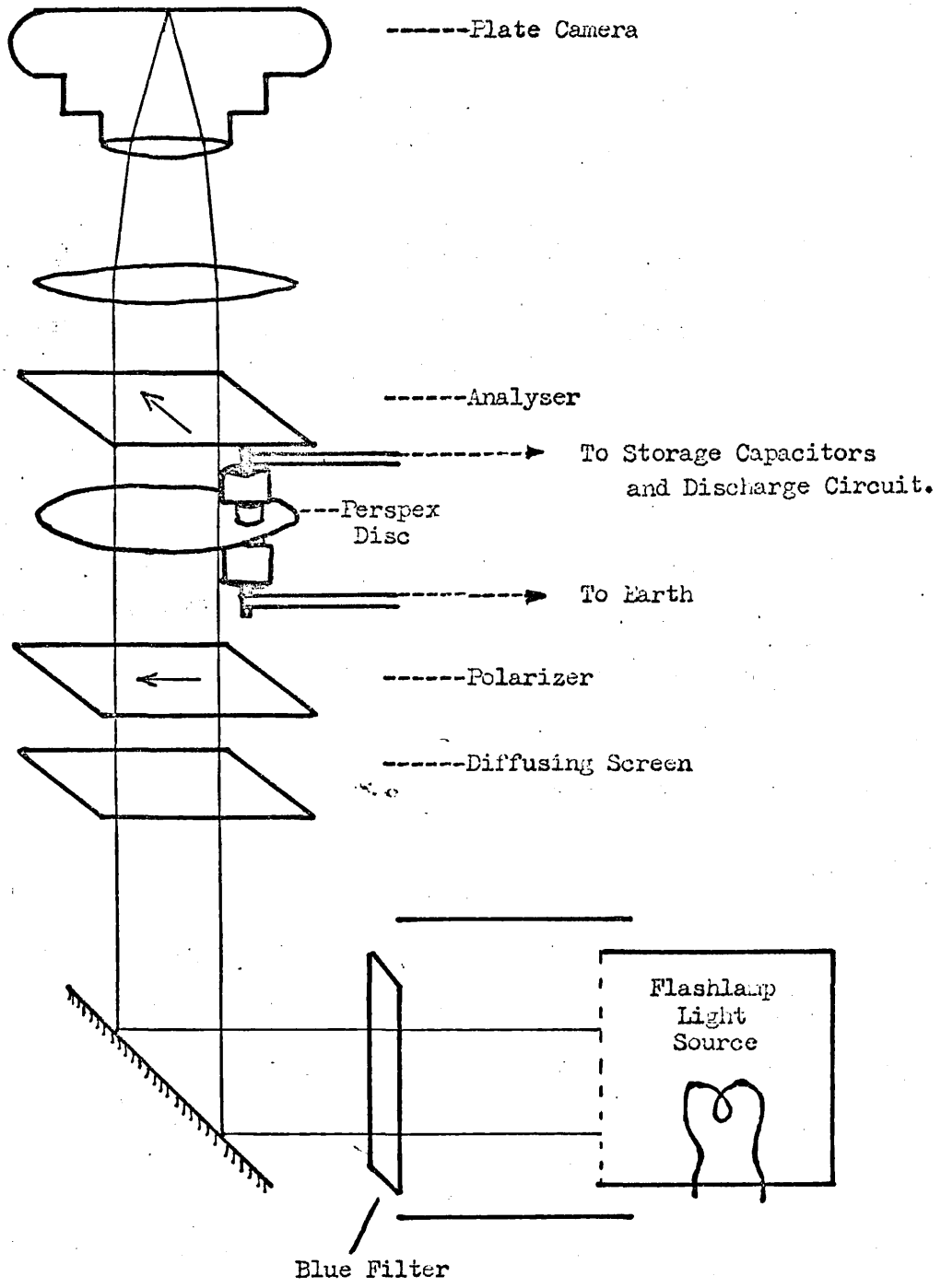

PHOTOGRAPHY OF SHOCK WAVES IN PERSPEX.

FIGURE 3-4.

would travel ~5 metres and have decayed to an acoustic wave in that time. The resulting photograph from this length of exposure shows a time integrated picture of the perspex strain pattern. The flashlight produces a white flash, but in order that the strain fringes correspond to optical rotation of only one wavelength, a blue filter was put in the system.

An electro-photonics dye laser was tried as a light source in order to produce shorter exposures. In the laser, two flash lamp capacitor configurations are possible so that the instrument gives a choice of two output power ratings. The SUA 1 configuration gives 20 kW for 1 μs , the SUA 2 systems introduces a larger capacitor into the flash lamp discharge circuit so that the laser output is raised to 120 kW for ~2 μs . During this period of time the shock wave travels 1→2 cms, but this power output leads to reduced flash tube life. The SUA1 configuration was used for the short pulse light source. The active medium was Rhodamine 6 G, and the laser was tuned by using an optical grating as one of the cavity mirrors. The wavelength used ~590 nm is in the centre of the dye laser output spectrum, the maximum tuning range with Rhodamine 6 G being 570-610 nm . During the 1 μs of the laser pulse the shock wave should move ~ 0.5→ 1.0 cms . If negligible shock front thickness is assumed, then a single exposure of this length gives a measurement of the velocity of the shock front. The apparent thickness of the shock front as photographed, divided by the exposure time, gives the velocity.

The received light intensity from the dye laser was found to be much less than from the flashlight. The main reason for lower intensity was the necessity to expand the beam to 6" diameter. It was found that it was necessary to replace the plate camera by a polaroid camera so that a fast, high contrast 2,000 ASA film could be used.

3.6 TRIGGERING AND SYNCHRONISATION

The capacitor discharge circuit is switched by the spark-gap switch which is triggered from a pulse generating circuit. No synchronizing circuits are needed for direct photographs of the exploding wire, but when the flash light is used, a delay circuit is introduced between the pulse generator and the spark-gap switch (see Fig.3.1). The flash light and pulse generator are triggered simultaneously, but the flash light has a natural delay time of $4 \rightarrow 5\,\mu s$ between triggering and discharge. This delay is compensated for by a delay on the spark-gap trigger pulse. This pulse is delayed $12\,\mu s$ between the pulse generator and spark-gap switch, and thus ensures that the time integrated photograph shows the complete explosion. When the dye laser is used, the delay line is no longer necessary as the dye laser has its own built in variable delay unit. A delay of $10^{-6} \rightarrow 10$ secs can be produced between the triggering of the laser and the output light pulse.

Oscilloscope recordings of the discharge voltage show that the maximum voltage across the wire builds up in $\sim 3\,\mu s$, the wire itself explodes at this time and the delay required on the laser is $\sim 2\,\mu s$ longer than this period. Synchronizing the laser was made difficult by the electrical noise produced by the capacitor discharge. The laser was liable to discharge prematurely. A PIN diode detector was positioned to monitor the laser output, this was displayed on a telequipment dual-beam oscilloscope, together with the voltage across the wire.

The PIN photodiode[103] was a solid state device with an intrinsic rise time of $<$ ns when used with a 50 ohm load. The power requirement was supplied by a dry cell with a small storage capacity. This produced an 18 V negative bias on the photodiode. This system was sufficient to drive the oscilloscope with a vertical sensitivity of 5.0 V/cm. The use of this device enabled the amount of jitter in the synchronization to be measured.

CHAPTER IV

INITIAL INVESTIGATIONS AND RESULTS

4.1 DESCRIPTION OF DISCHARGES, ENERGIES FOR VAPOURISATION

The maximum rate of deposition of energy into an exploding wire is dependent on the resistance of the wire and subsiduary circuit and on the voltage to which the storage capacitors are charged. Provided that the capacitance is great enough to contain the critical quantity of energy which is required to explode the wire, then the actual value of the capacitance is not important as it is no longer a limiting parameter in the determination of the maximum power dissipation. The energy needed in order to explode the wire is dependent on the thermal capacity and latent heats (or more accurately the sublimation energy) of the wire.

Two different wire materials were used. A 'Eureka' alloy wire of 29 SWG (0.345 mm diameter) and having a resistance of $4.32\,\Omega\,m^{-1}$ was exploded. This wire had a small sublimation energy and thus exploded in less time than wires of greater mechanical strength. The second wire to be used was a steel piano wire with 28 SWG (0.0148") diameter. The resistance of the steel piano wire was $1.46\,\Omega\,m^{-1}$ which together with the higher sublimation energy produces a more delayed explosion. The relatively high boiling point of this material ($> 3{,}070\,^{\circ}C$) makes it possible to explode the wire in such a way as to produce a mixture of wire vapour and molten droplets. It is also possible to produce the same form of explosion with Eureka wire, but only over a lower range of discharge energies. The wire droplets from a Eureka wire generally appear to be smaller than those produced by the similar explosion of a steel wire, and also more liable to disintegration.

The discharge voltage across the wire was recorded, and Fig.4.1 shows the plot of voltage against time as measured on the high voltage

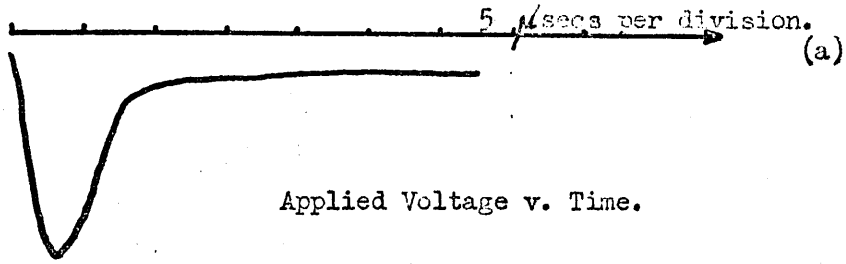

Applied Voltage v. Time.

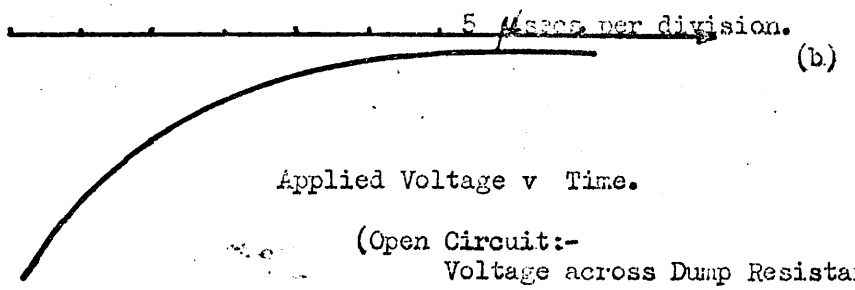

Applied Voltage v Time.

(Open Circuit:-
Voltage across Dump Resistance.)

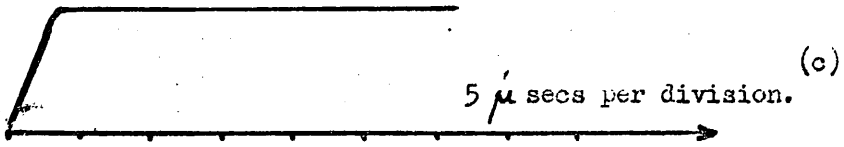

Output of Flashlamp.

FIGURE 4-1.

side of an exploding Eureka wire. The capacitors are discharged both with, and without the wire in position. The Telequipment oscilloscope was used in conjunction with a potential divider (see Fig.3.1). Fig.4.1(c) shows the output of the detector monitoring the flashlamp and shows the rise time of the flash output. Because of the length of the flash rise time, a time delay was introduced between the triggering of the flashlamp and the triggering of the wire explosion. The capacitors initially had an energy of 245J .

When the wire was removed from the discharge circuit, the capacitors discharged, dumping the energy directly into the dump resistor which was permanently in parallel with the wire. In Fig.4.1(a) it can be seen that there is apparently no further arc across the wire after about 10μs from the time the discharge starts, so the voltage builds up as the new equilibrium is reached and then falls more slowly as the remaining charge goes into the parallel dump resistor.

In order to obtain these oscilloscope traces, care had to be taken to screen the oscilloscope and the leads in order to stop the pick-up of spurious signals during the high voltage discharge.

4.2 CORRESPONDENCE OF OPTICAL MEASUREMENTS TO WIRE ENERGY

The energy dumped into the exploding wire is dissipated by two mechanisms. First, it is used in the sublimation and latent heats of the wire so as to produce the resultant explosion, and secondly, some of the remaining energy is dissipated as light radiation and as the kinetic energy of the wire debris.

The comparison of photographs of a series of explosions with similar appearance, when the size of the radiating cloud of vapour produced by the wire is identical for different types of wire, shows that ~40J

less energy stored in the capacitor is required to produce a cloud of given volume from a constantan wire, than that required for a steel piano wire. The cross-sectional area of this luminous cloud is very roughly proportional to the energy stored in the capacitor for energies near the critical minimum to produce an explosion. From the observations, the energy required to explode the wire, can be deduced from the intercept on the energy axis of a graph of energy v. incandescent area. For constantan wire $\sim 64 \pm 5$ J and for steel piano wire 105 ± 5 J must be discharged from the storage capacitors. The measurements can only be very approximate, because any measurement is necessarily complicated by the fact that at low energies the electrical discharge produces a combination of liquid drops and vapour. Thus the cross-sectional area of the vapour cloud, whilst it gives some measurement of the velocity and the temperature which the vapour has reached by measuring the distance it travels while it is emitting visible radiation, does not tell the full story. Glowing droplets of the molten wire travel very much further than the radiating vapour. This implies that either the rate at which the velocity of the drop decreases due to viscous drag is very much less than the deceleration of the vapour cloud, or else the liquid drops start with a higher velocity or temperature. Obviously the initial temperature of the droplets must be lower than the equivalent vapour temperature. Even if the liquid droplets were to start with a higher initial velocity (which is unlikely) the viscous retardation is proportional to v^2 $\{F = k\, v^2\, \rho L^2\}$ so any small variation would not have such effect.

From the photographs (Fig.4.2) it is seen that while the average diameter of the vapour cloud is < 10 cms the paths of the molten droplets can in some cases be traced as far as 50 cms . This is easily explained by the relatively great momentum of the droplets. The viscous drag on

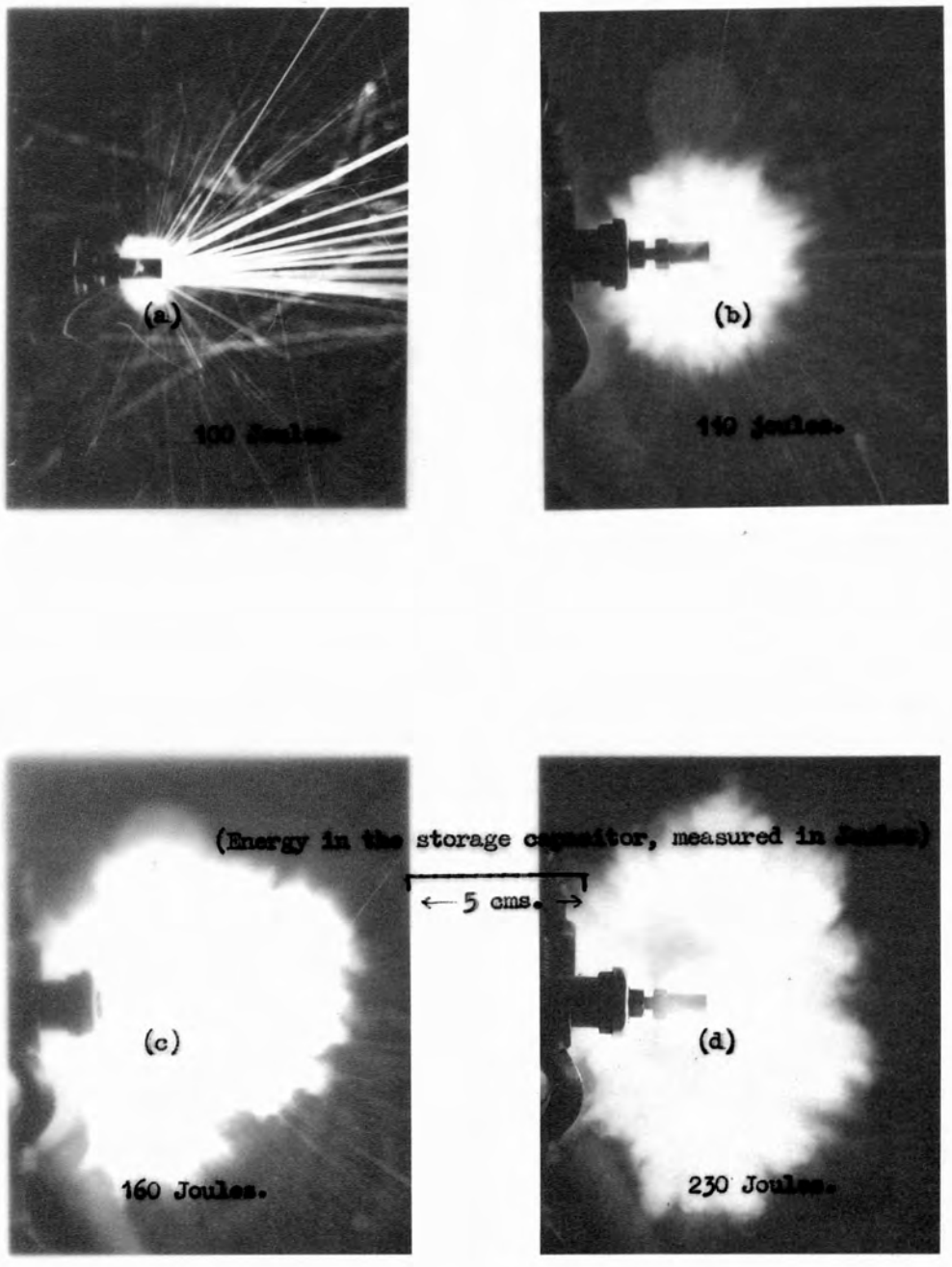

EXPLODING STEEL WIRES.

FIGURE 4-2.

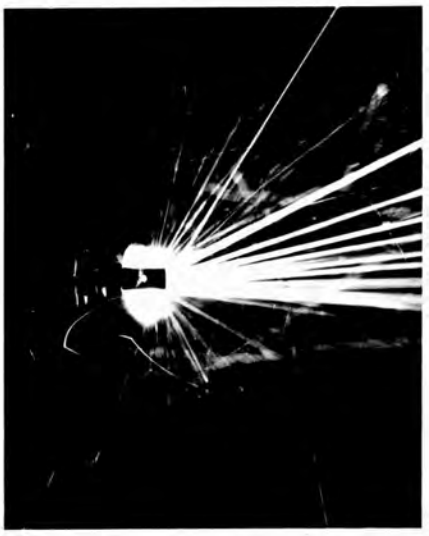

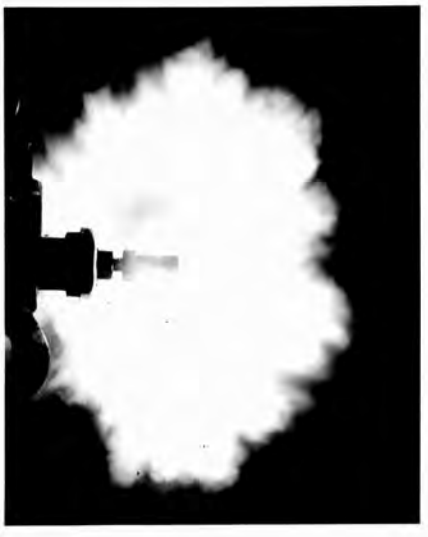

the debris is proportional to r^2 for each particle, and the mass is $\propto r^3$ thus the relatively larger droplets receive proportionally less drag per unit mass.

From Fig. 4.2 it can also be seen that there is a relation between the nature of the wire droplets produced, and the energy of the explosion. While this relationship cannot easily be quantified, it is clear that at low energies the wire has a great tendency to explode non-uniformly, and produce a great number of larger slow moving liquid droplets. As the energy of the discharge increases, the size of the particles decreases whilst their velocity increases. At higher energies there is a far greater uniformity in the explosion, as indeed there must be if momentum is to be conserved. When less energy is supplied to the wire, the momentum conservation in an apparently non-uniform explosion can only be explained if part of the wire is presumed to have melted and exploded while the main body of the wire is still in situ to absorb the reaction, this must clearly have been the case in Fig.4.2(a).

4.3 PHOTOGRAPHIC OBSERVATIONS OF WIRE EXPLOSIONS

Photographic recordings of the incandescent liquid drops thrown off by an exploding wire, show that there is a distinct difference between the effects produced by the explosion of a constantan wire, and the explosion of a steel wire. The physical differences in the solid materials of the wires — latent heats and melting points — are reflected in the liquid properties. The surface tension of the liquid is a significant parameter as it relates to the initial size of the drop. This size together with the velocity, determines the behaviour of the drop on impact with a solid target.

In Figs.4.3 and 4.4 the explosions of constantan wires using capacitors containing energies of 110J, 95J, and 80J, respectively, are shown.

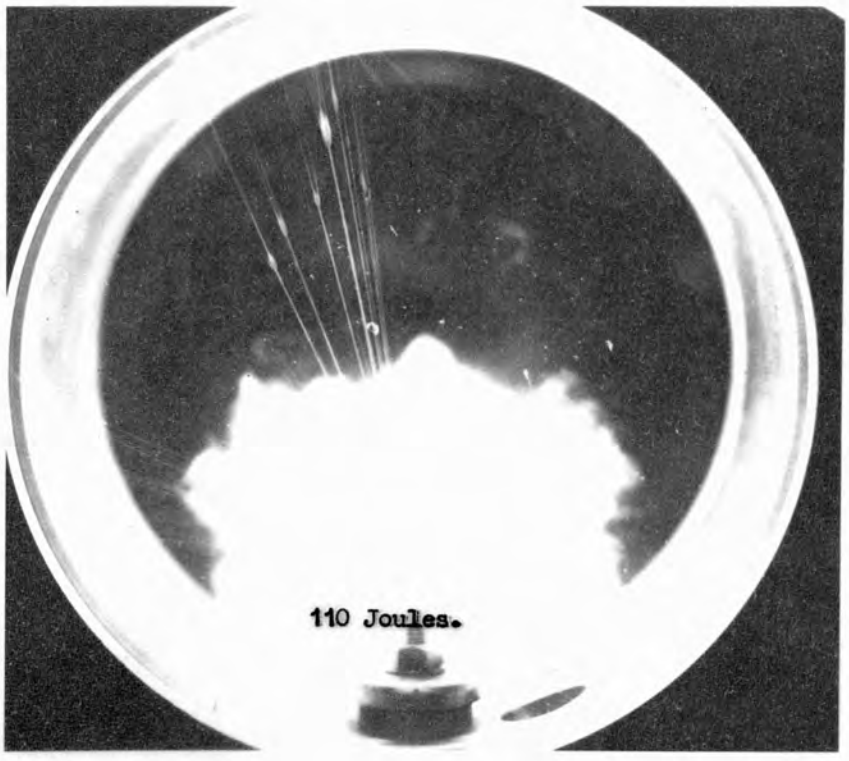

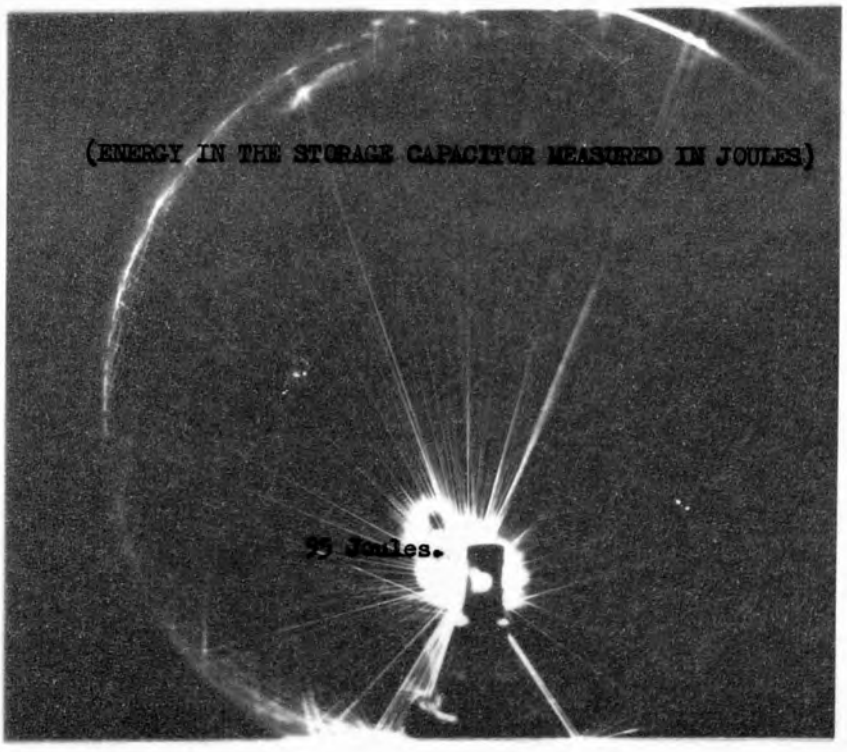

EXPLODING CONSTANTAN WIRES.
FIGURE 4-3.

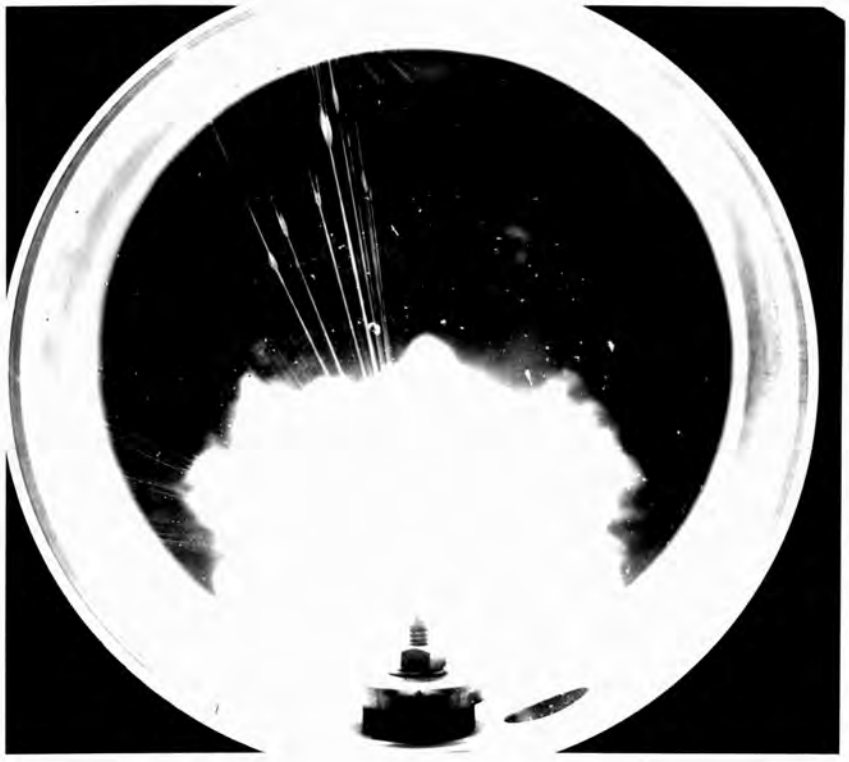

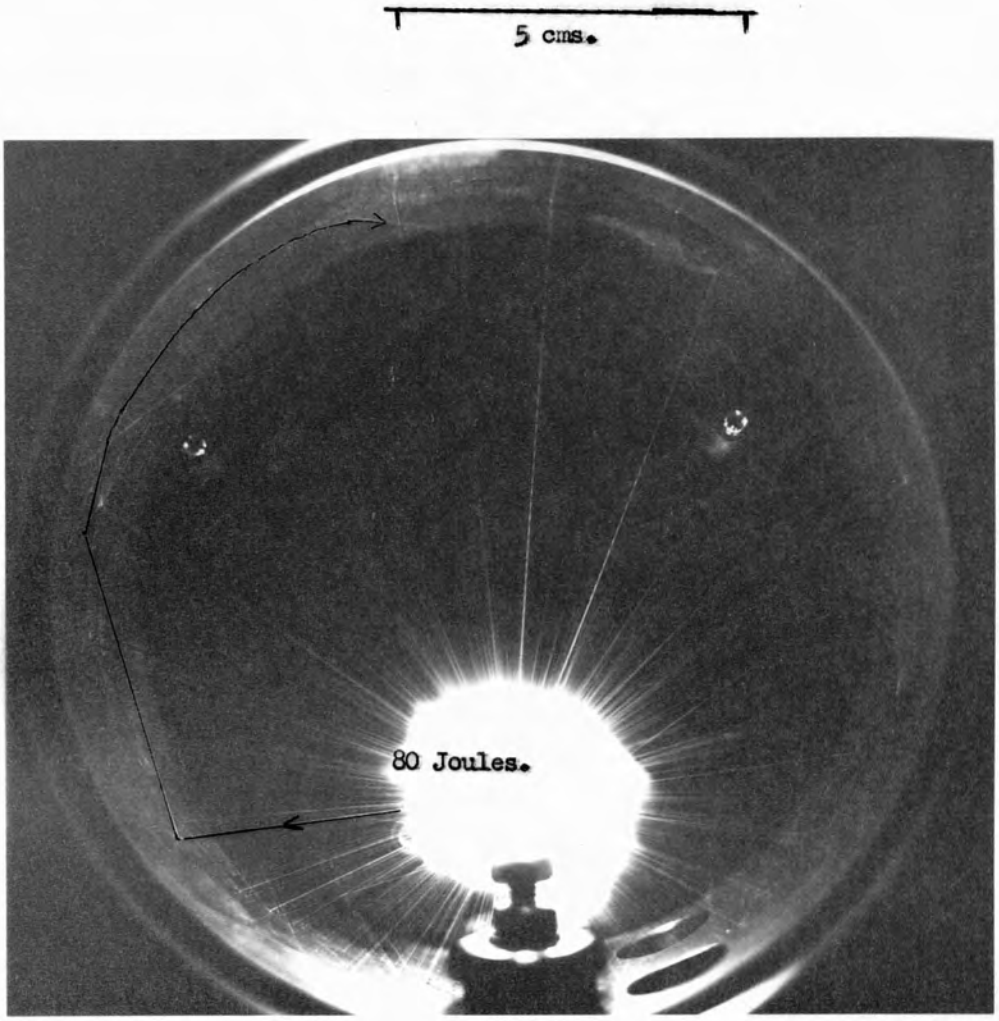

(Cavity Diameter: 4.5")

EXPLODING CONSTANTAN WIRE.

FIGURE.4-4.

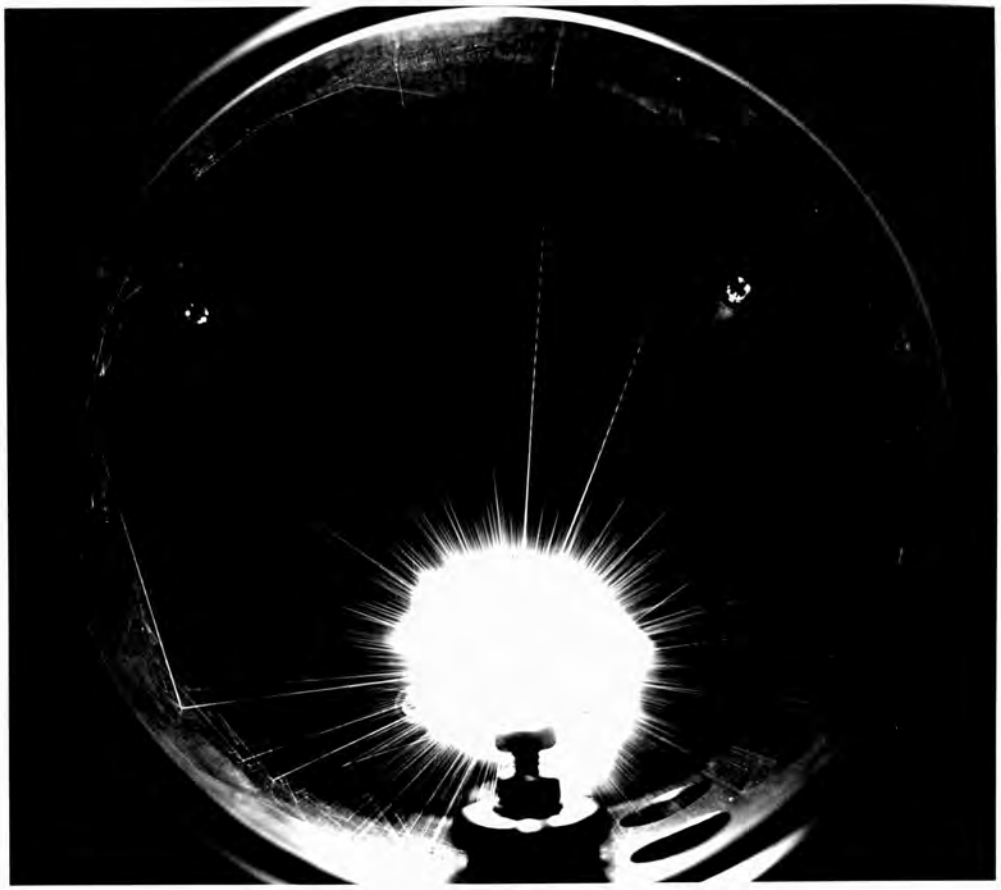

The wires were enclosed in the dural chamber with the glass cover plate in position. At these energies a wire does not always explode uniformly. In Fig.4.3(a) it can be seen that a sizeable segment of the surface of the wire has been blown off in one direction before the main explosion. This primary explosion consists of about twelve large droplets which move not only radially, but also axially upwards towards the glass cover plate. On striking the cover plate a series of secondary explosions is produced as the droplets disintegrate. Disintegration may, however, have been produced by the action of the atmosphere, by the mechanism as described on page 55. In Fig.4.3(b) a similar effect can be seen with the droplets this time striking the wall of the cavity. It can be seen that again the larger drops disintegrate to produce a 'splash' appearance on impact. The smaller drops, however, are reflected off the surface without giving rise to any secondary droplets. Indeed as Fig.4.4 shows, these droplets have a small coefficient of restitution with the dural walls ($\sim$ 0.17) and in Fig.4.4 the path of one droplet can be traced around nearly one quarter of the circumference of the cavity.

Also on this plate it can be seen that two of the droplets have a periodic variation in the intensity of the emitted radiation. The periodicity is constant over the complete path covered inside the cavity, and so it cannot be used to give a measurement of the deceleration of the particle. The velocity of the particle must be approximately constant over the path if a uniform periodicity can be assumed. There are two possible mechanisms for producing the periodicity. First, it may have been caused by the droplet oscillating and changing the shape of the profile facing the film; secondly, if the particle consisted of solid material then a rotation of an asymmetric particle would produce the same effect. Any interaction with the glass cover plate can be ruled out as the periodicity starts only $\sim$0.75 cm from the wire. For a particle to reach the glass this close to the axis of the wire a high axial velocity would be necessary. If this had been the case the particle would have

had sufficient impact velocity to bounce clear of the cover. The likelihood of interaction with the glass cover is also lessened because in similar circumstances in Fig.4.3(a) when interaction with the glass cover may have been observed, there is no consequent periodicity.

Fig.4.5 shows further plates produced by this technique. The main details of the photographs are pointed out on the plates. However, no satisfactory explanation can be produced to explain the motion of the particle in plate (b), it may be that this is a very slow moving droplet whose motion is altered by an oxidation process.

Observations were also made of the paths of particles from the exploding steel wires. For these observations the large container was used, and a restricting aperture was placed next to the wire making possible the observation of the paths of individual droplets of wire unimpeded by the mass of debris also flying around the enclosure. The surface tension of steel is higher than that of constantan, and thus different results were expected with regard to the size and stability of drops produced by equivalent explosions.

Fig.4.6 shows some of the plates obtained by this method. The large droplet in Fig.4.6(b) is the result of an explosion with capacitor energy near the critical minimum required to explode the wire, (125J). The impact with the target causes the droplet to disintegrate into seven secondary droplets. The single droplet which is separated by the aperture in Fig.4.6(a) is reflected off the same sheet of aluminium. This smaller droplet does not disintegrate immediately on impact, as the droplet slows down it appears brighter. Fig.4.7 shows the same effect.

In all three cases it is seen that a secondary explosion takes place after impact with the target plate. The highly unstable, large, slow moving drop disintegrates virtually on the surface of the plate. As the

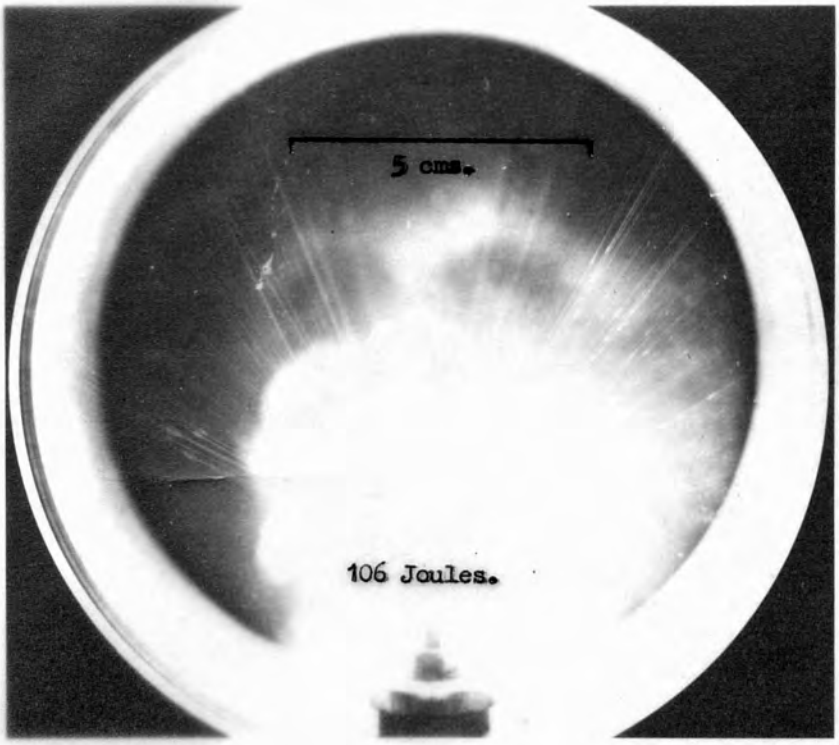

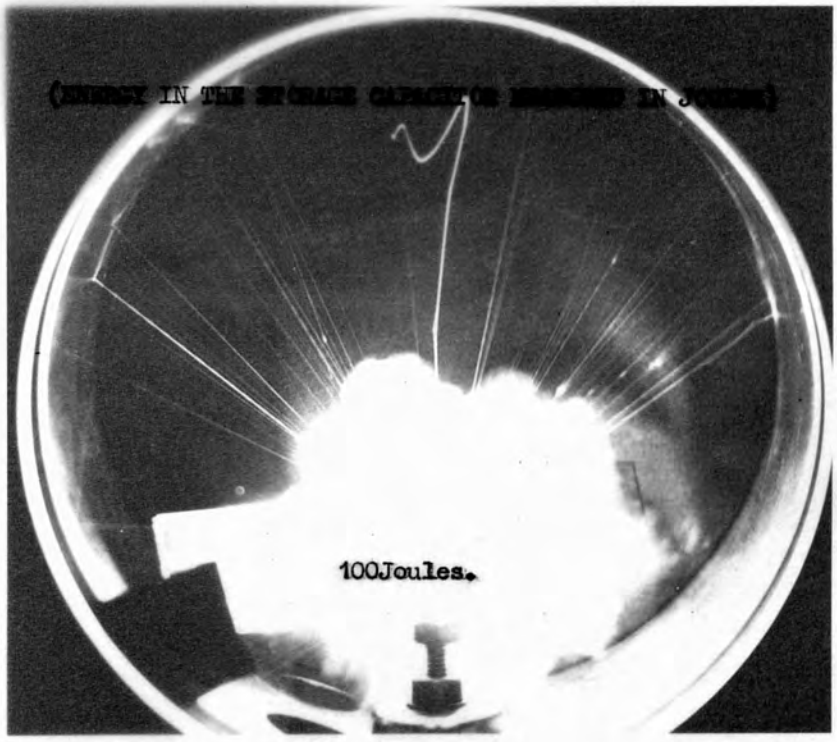

EXPLODING CONSTANTAN WIRE.

FIGURE 4-5.

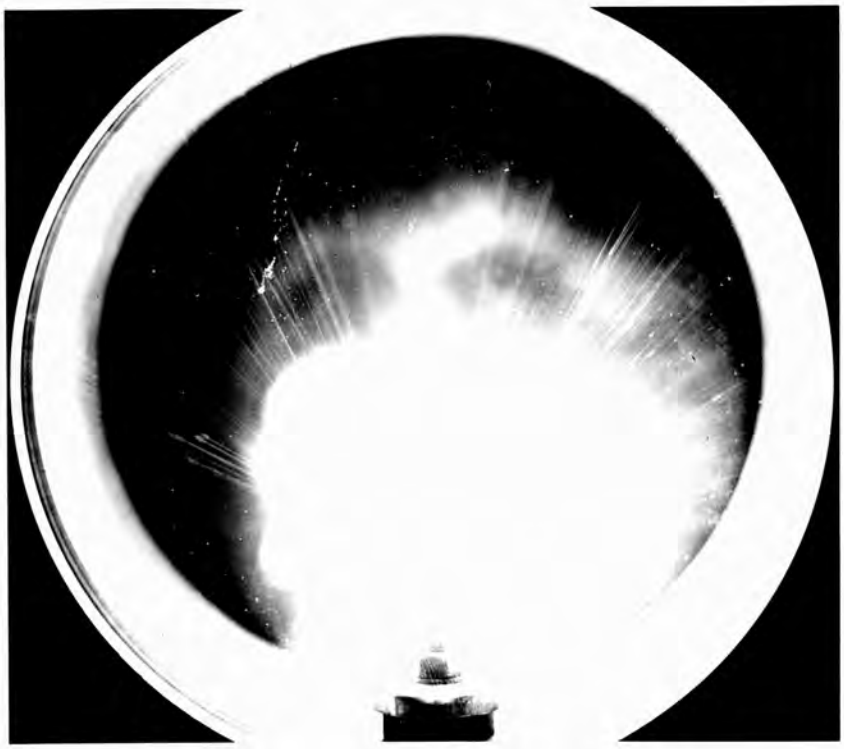

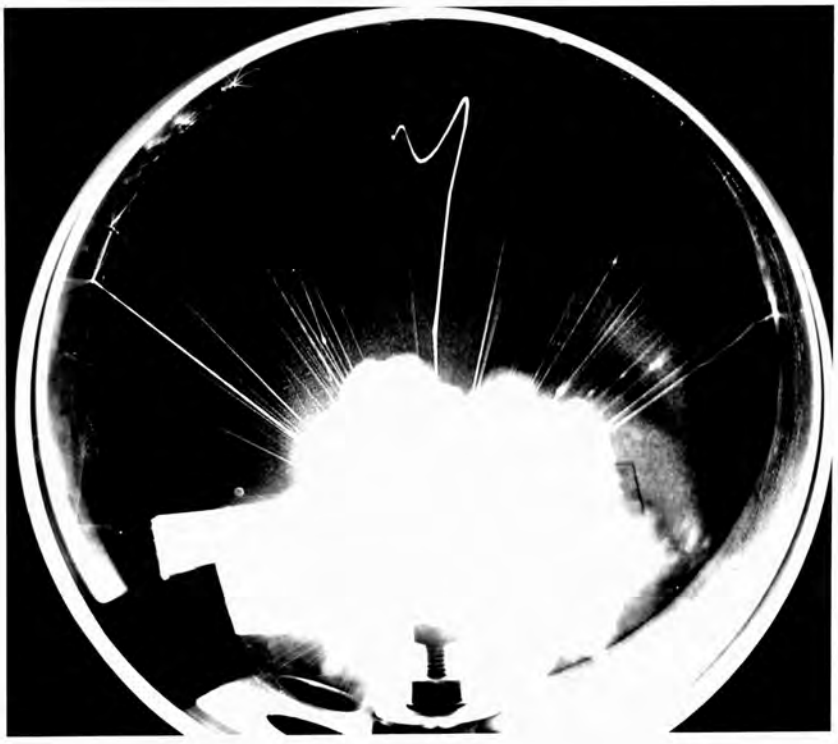

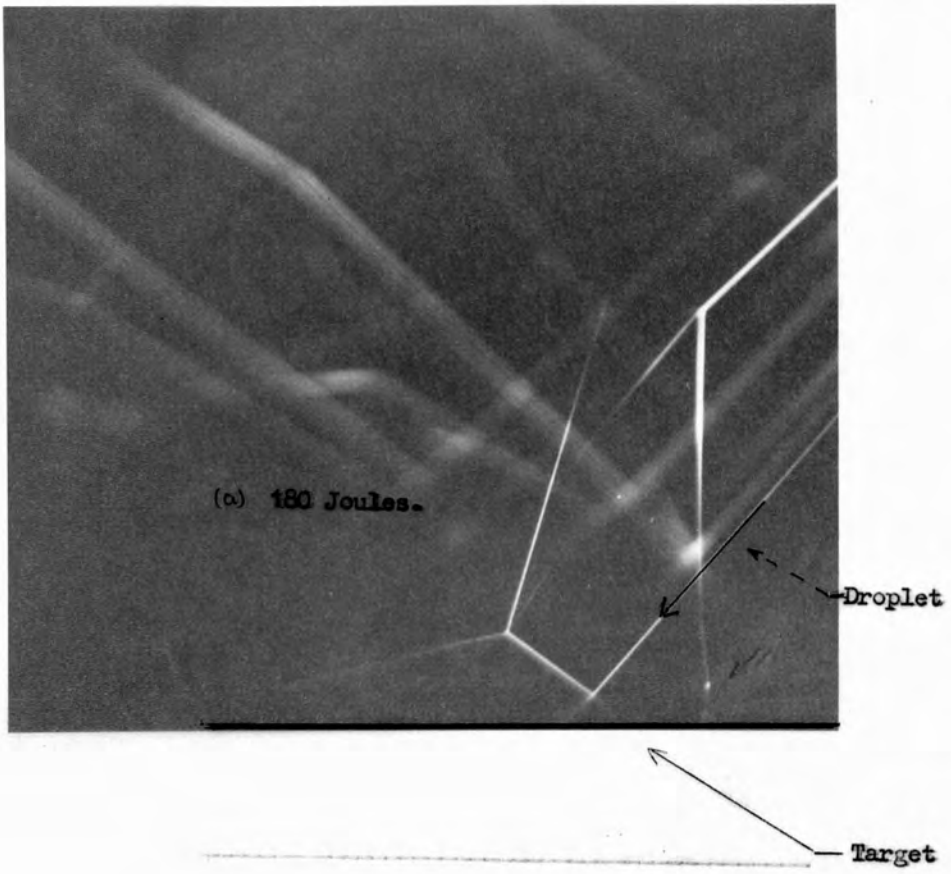

STEEL WIRE DROPLETS STRIKING AN ALUMINIUM TARGET.

FIGURE 4-6.

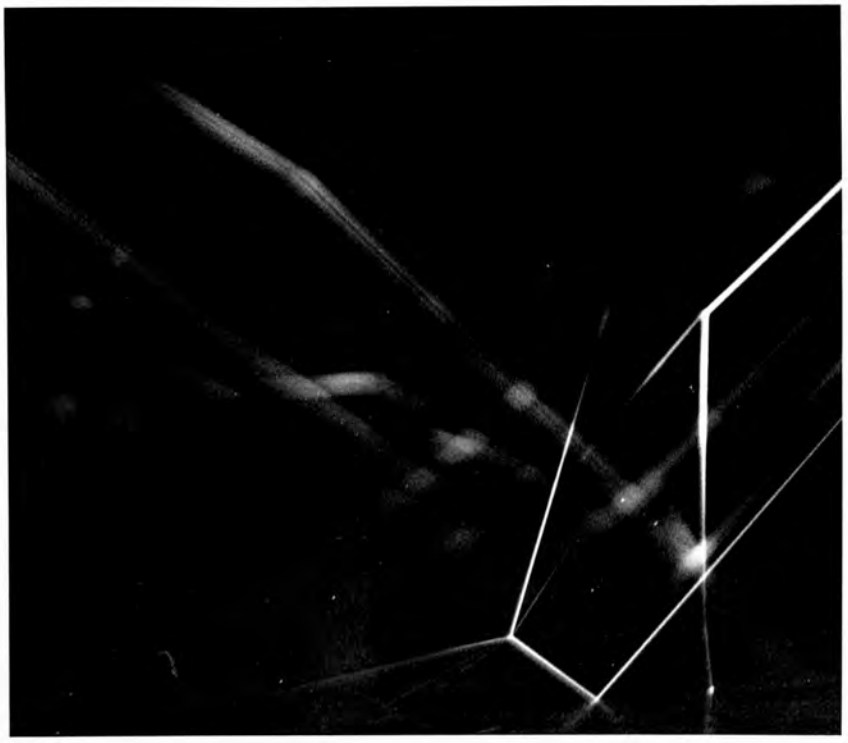

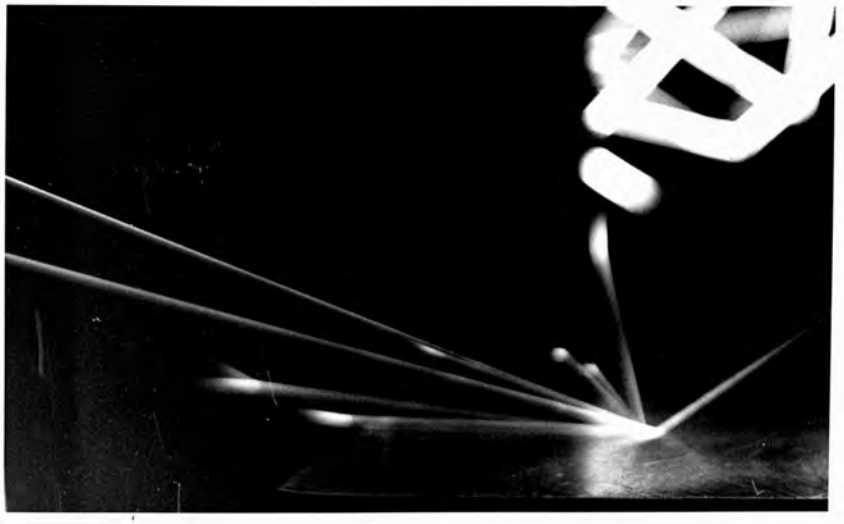

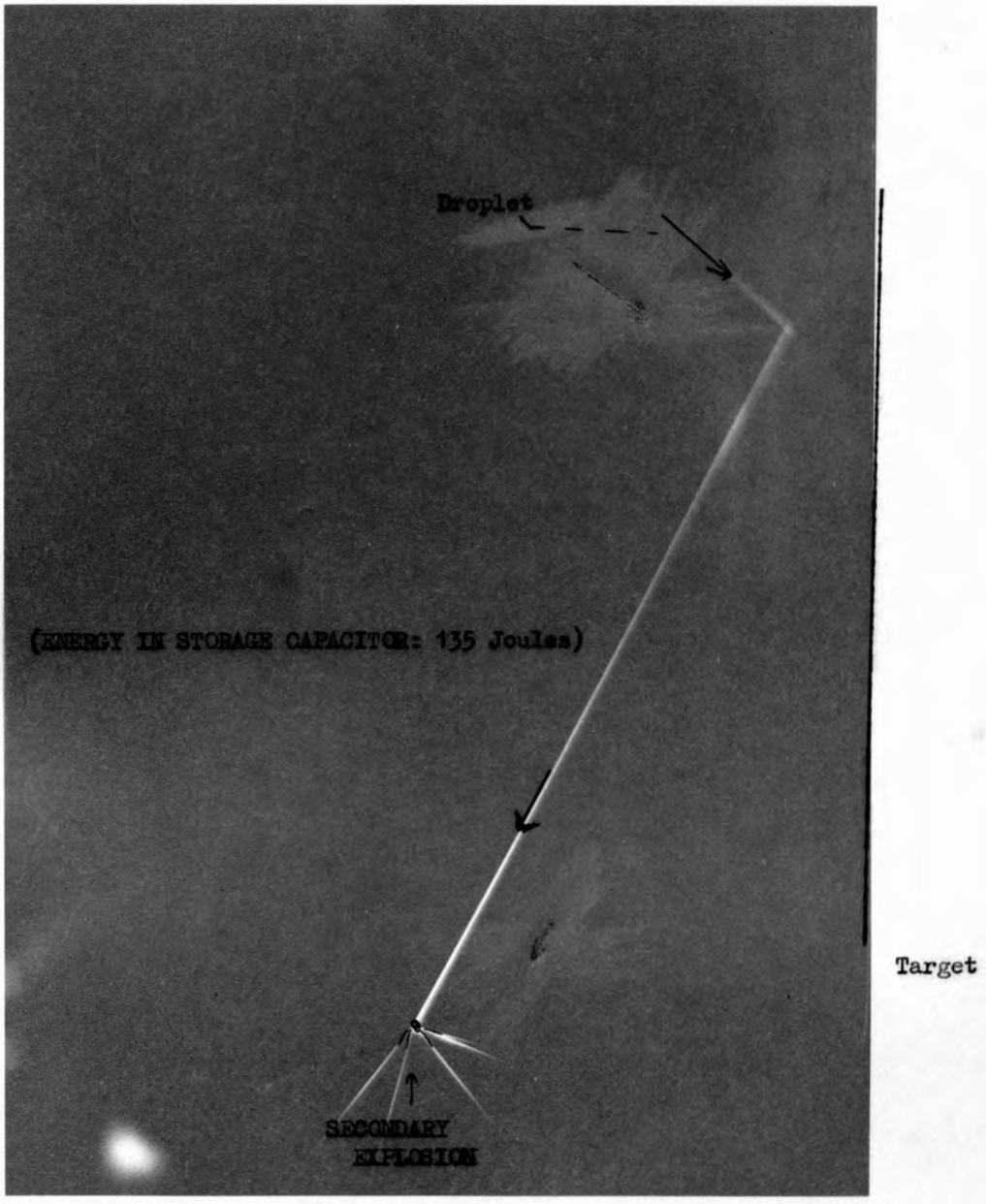

STEEL WIRE DROPLET HITTING ALUMINIUM TARGET.

FIGURE 4-7.

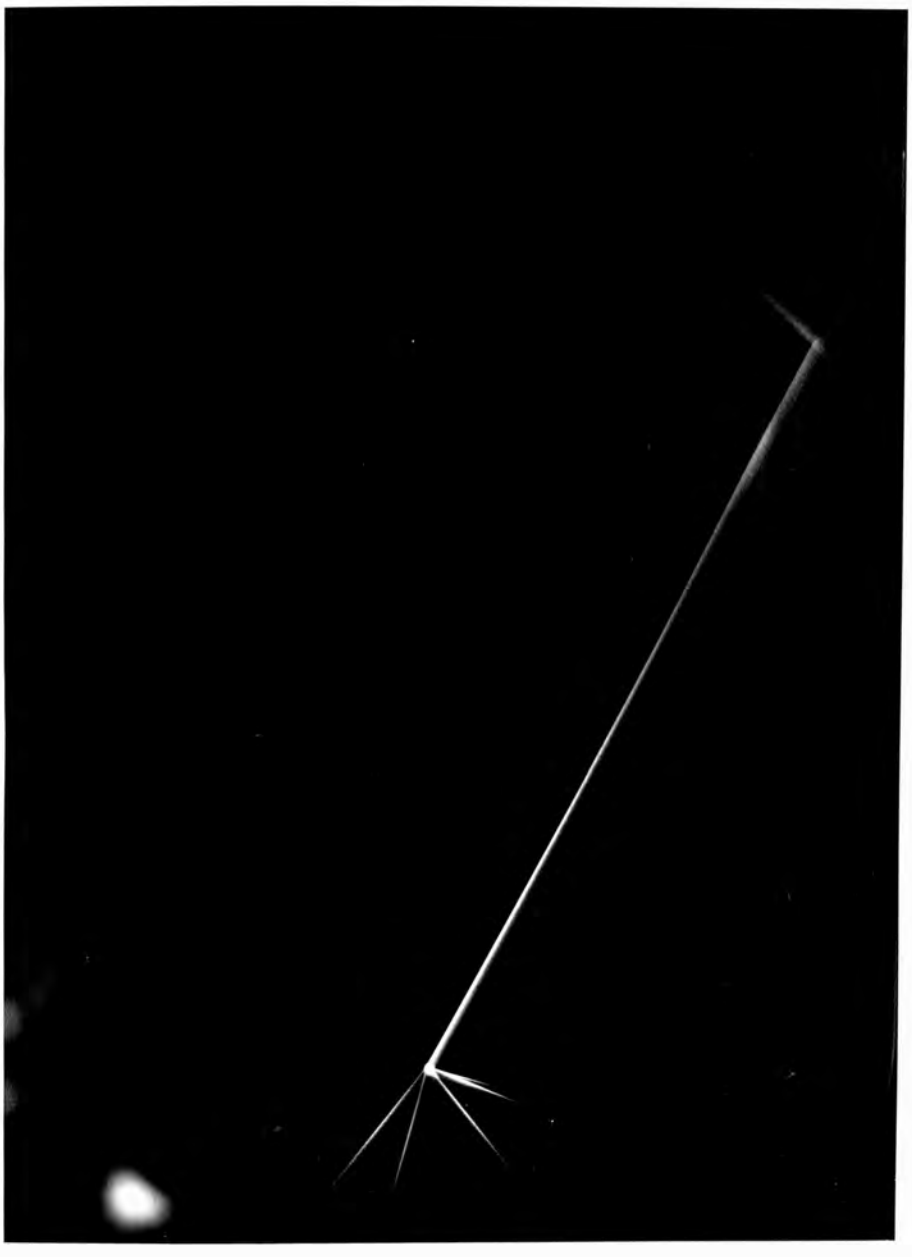

energy of the explosion is increased, the smaller, faster drops explode at a distance from the surface independently of any further interaction.

The apparently spontaneous disintegration of wire droplets may be the product of a number of mechanisms. Otherwise stable droplets may be rendered unstable by impact on to the target. When a drop strikes a solid surface, a compressive wave is produced which moves through the drop from its forward-facing to its backward-facing surface. According to Barnett[67] the reflection of the wave from the back surface creates a tensile wave which produces instability within the drop, and leads to the likelihood of cavitation and disintegration. It should be emphasised here that many of the drops appear to disintegrate spontaneously. Barnett's mechanism cannot apply for these cases, except for some of the droplets which may have undergone an impact with part of the electrode structure supporting the wire. The impact mechanism described by Barnett could well account for the disintegration shown in Fig.4.6(a), but for spontaneous disintegration, two other mechanisms remain.

Lane et al[104,105] have shown the action of the atmosphere on a liquid drop projectile to be such as to produce the disintegration of the droplet. A relationship can be determined between the velocity of the droplet moving through the air, and a critical diameter above which the droplet will be unstable at that particular velocity. The critical diameter of the droplet is dependent on the surface tension of the liquid. It is found that

$$u^2 \cdot d = \text{constant} \qquad \ldots (4.3.1)$$

where u = maximum velocity through the medium at which the droplet is stable.

d = diameter of the droplet.

The relationship for the surface tension is also a simple one :

$$u = k\sqrt{\frac{\gamma}{d}} f(\sigma, \rho) \qquad \ldots (4.3.2)$$

where γ = surface tension,

σ,ρ = density of liquid and air respectively, and

k = constant.

As the droplet travels through the air it becomes increasingly flattened on the front surface and expands laterally. Fig.4.8 shows a series of photographs taken by Lane to show drop disintegration. As the droplet expands laterally the front surface is blown in so that a hollow bag is formed with a roughly circular rim. The hollow bag expands to a size many times that of the original droplet until eventually the bag bursts, producing a shower of smaller drops.

After the bag has burst, the rim remains intact for a short time before disintegrating into a number of droplets which are much larger than those created by the bursting bag. The mass of the drop is divided so that approximately 70% of the mass is contained in the ring. The remaining 30% of the mass is contained in the surface of the bag. Thus, at the moment before it bursts, the bag has an extremely small thickness. In the case of the droplet shown in Fig.4.8 the thickness is $\sim$10 microns.

In the case of large droplets, the stability is reduced and oscillations are liable to upset the disintegration. In many cases, the bag may develop a local thickening which produces a central stalk which survives the disintegration of the bag. The size of droplets thrown off by the exploding wire is unlikely to be large enough for this to happen.

Assuming that the relationship between u and d holds good over a wide range of drop size, the critical velocity for a water droplet, the same diameter as the wire is $\sim$175 m/s. As the relationship with surface tension is square root dependent, this value probably holds for wire droplets to within an order of magnitude. This range of particle velocity is quite easily obtained from exploding wires, though if the wire

STAGES OF BREAK-UP OF DROPS OF WATER.

DIAMETER OF DROP 2·2 MM.
VELOCITY OF AIR STREAM 24 M/SEC.

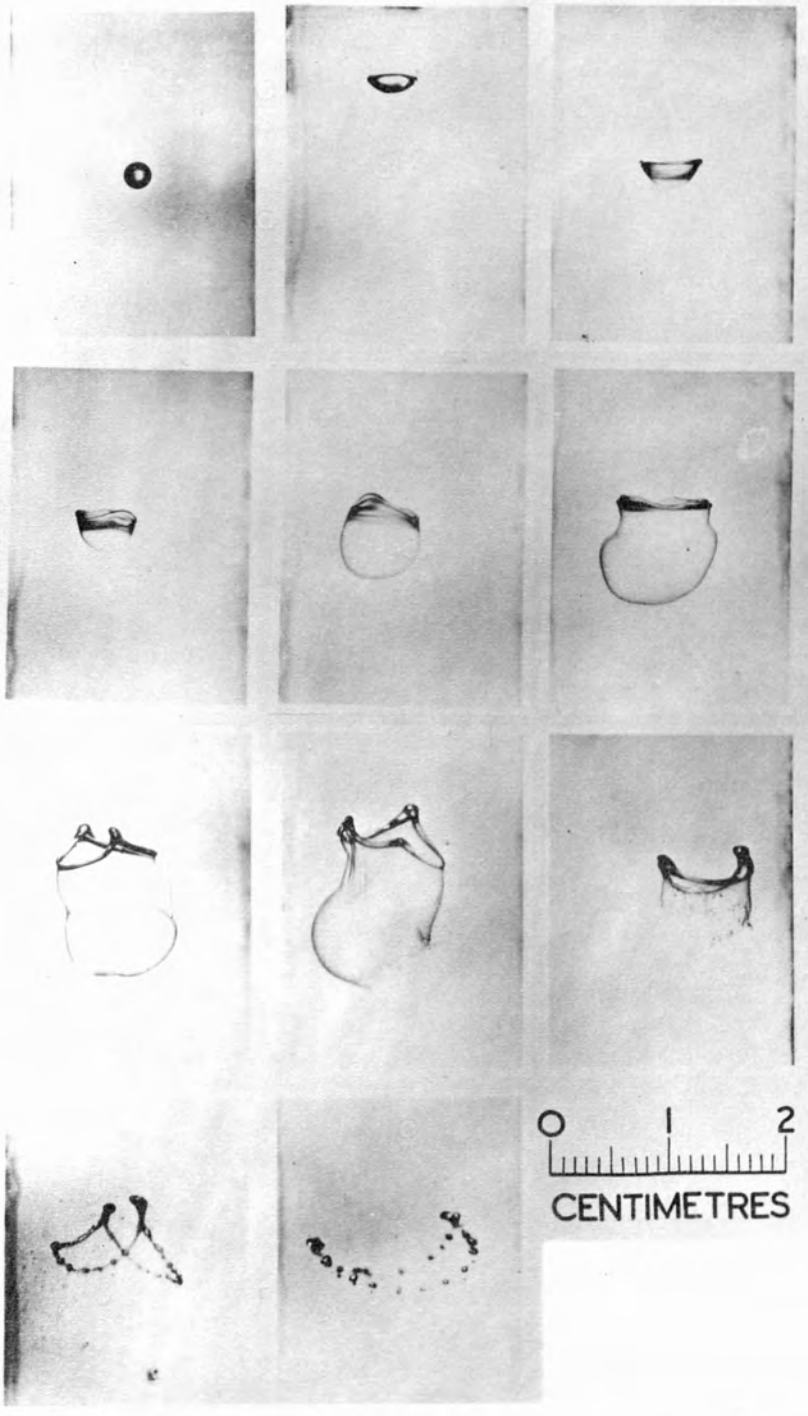

FIGURE 4-8.

STAGES OF BREAK-UP OF DROPS OF WATER.

DIAMETER OF DROP 2·2 MM.
VELOCITY OF AIR STREAM 24 M/SEC.

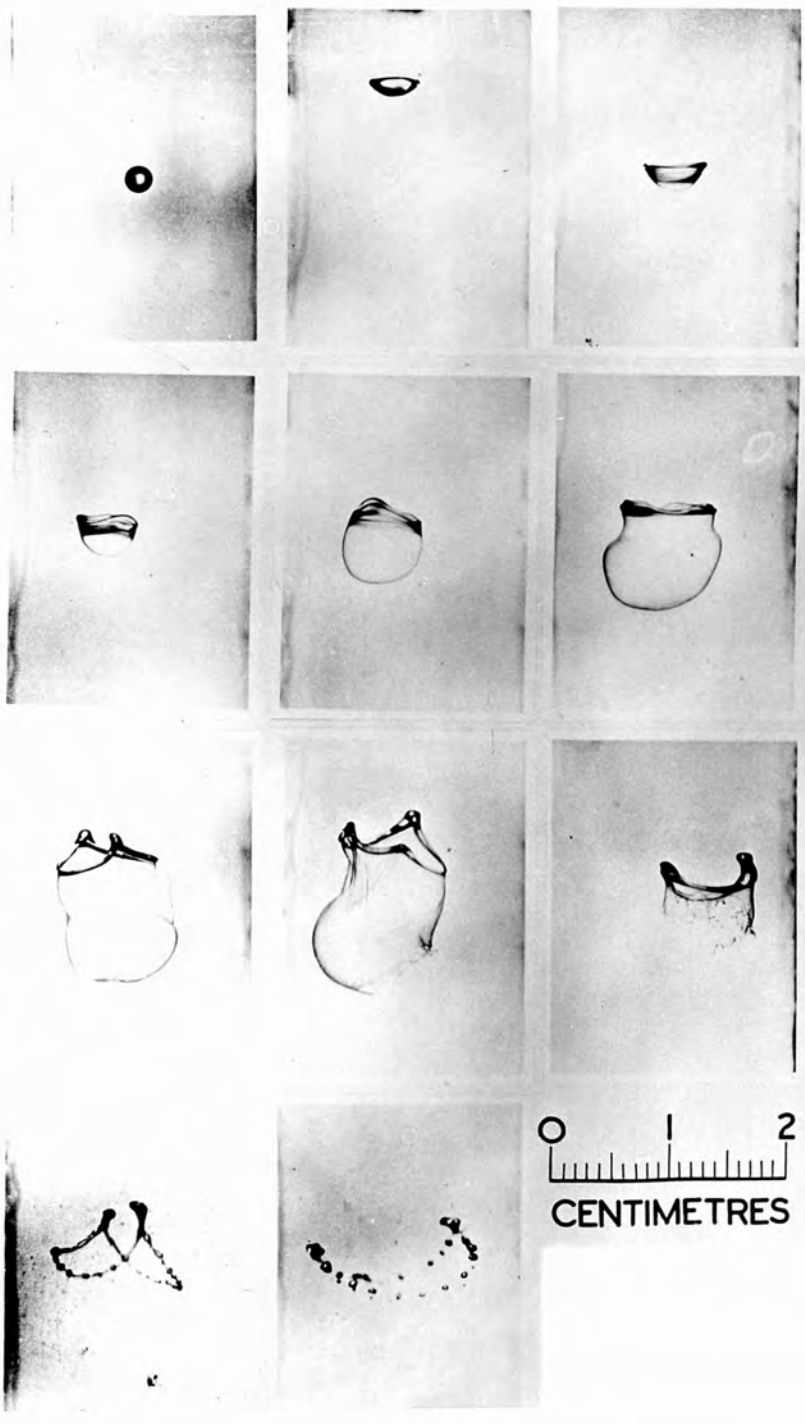

energy increases, the droplet velocity also increases but the droplet diameter decreases. Thus the critical velocity will be increased.

When droplets are subjected to high velocity transient air blast, where the velocity is very much greater than that critical for the drop size, a different disintegration mechanism operates[106]. The droplets become subject to a shattering process which causes the droplet to break-up by removal of liquid initially from the surface.

The mechanism for disintegration in the manner as shown in Fig.4.8 can be explained by normal fluid mechanics. Measurements of the distribution of pressure over a sphere in an air flow show that a positive pressure exists in front of the sphere and a reduced pressure at the sides and rear[107]. This tends to produce a deformation which is opposed by the force of surface tension[108]. The greatest pressure takes effect on the centre of the front of the drop, so this is where a depression would be likely to form.

The development of the bag, and the expansion of the ring diameter is likely to have been induced by vortex motion developed in the drop by frictional forces with the air.

Thomson and Newall[109] have found vortex action producing a more stable ring shape when studying liquid drops in liquids. The break-up of the ring into droplets may be explained in terms of Rayleigh's law concerning the stability of a liquid column[110]. Surface tension produces instability in a column if the length is more than eleven times the diameter. If the rim thickness is small compared to the diameter, this condition is approximately true.

Due to frictional forces, the drop must inevitably slow down, and for this reason appear to brighten. It is possible with hot wire droplets, that the brightening may be due to the drop getting hotter by a process

of oxidization. In this case, this process might also contribute to the explosion which terminates very many of the trajectories.

4.4 OTHER PHENOMENA PRODUCED BY EXPLODING WIRES

4.4.1 Damage Caused by Wire Debris

Surfaces impacted by flying wire droplets were examined microscopically, and interferometry was used in order to determine the effect of the impact. In most cases the damage to the surface was found to be negligible. In the case when a glass surface is held close to a low energy wire explosion, damage is produced by the action of the hot wire droplets etching the surface of the glass. At higher energies, where the individual droplets are smaller, negligible damage results from the blast of the exploding wire vapour. In order to determine the damage produced from the vapour, a comparative method was used. A portion of the surface under examination was protected from the blast by a metal sheet. After the explosion, when the layer of wire dust had been removed from the exposed part of the surface, the two areas on the surface were compared.

Fig.4.9(a) shows the impact crater created in glass by a drop of molten constantan from a wire with capacitor discharge energy $\sim 120\,J$. It can be seen that around the crater there is a complete absence of any hill of displaced material, showing that the action of the droplet was to remove the material by evaporation and not merely to displace the surface by force of the impact.

4.4.2 Fibre Production

When the Eureka wire was exploded at relatively high energies ($\sim 245\,J$), the debris from the exploding wire settled out of the atmosphere as a very fine dust. This dust is slightly cohesive, and under certain experimental conditions it was observed to settle in the form of long fibres.

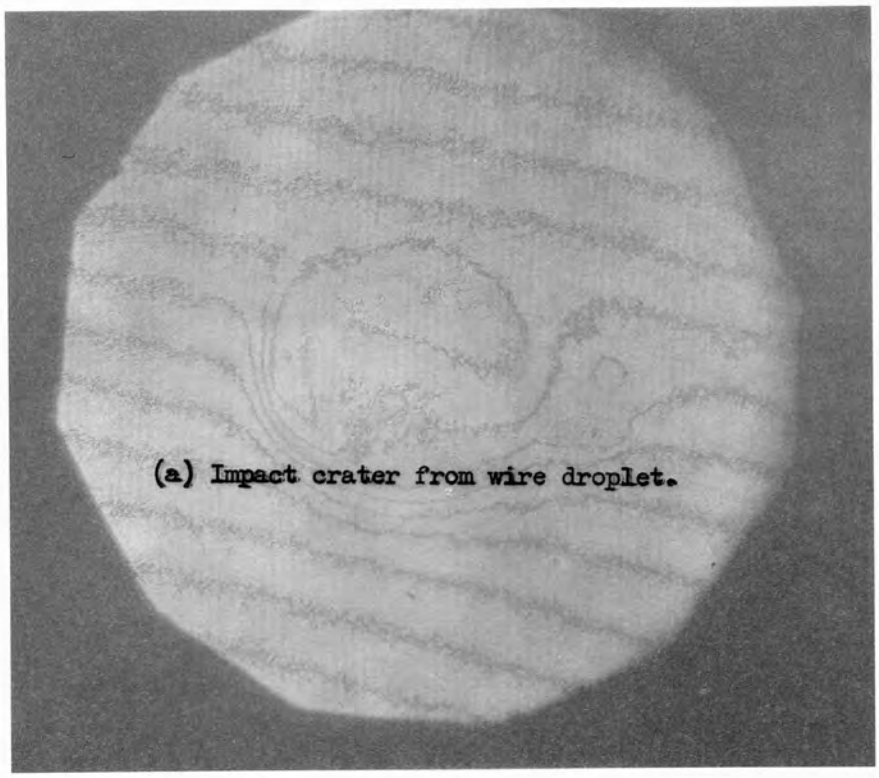

(a) Impact crater from wire droplet.

(b) Wire fibres.

FIGURE 4-9.

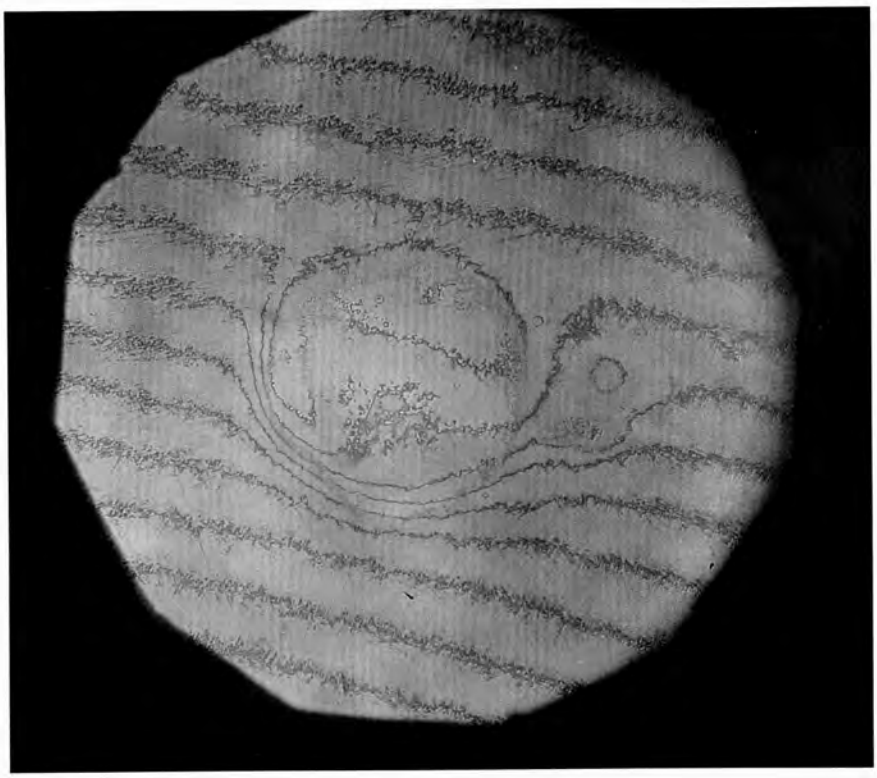

These observations were the bi-product of early attempts to explode the wire and transmit the pressure wave directly into a perspex disc by passing the wire through the disc in a 2×10^{-2} inch hole drilled through the surface. This method does not stop any light produced by the explosion from reaching the camera lens, and any effects due to birefringence in the plate are swamped by the surplus light. If the electrodes and disc are examined afterwards (see Fig.4.9(b)) the fibres are seen to stretch from the plate to the electrode and to the walls of the dural container. The diameter of the fibres is typically ~ 0.01 cms. The longest fibre shown here is ~ 0.9 cms long. The fragments on the surface of the perspex are from the area immediately around the hole where the surface has been shattered by the blast wave.

The mechanism for the formation of these delicate fibres is probably related to the presence of an electrostatic field around the disc and electrodes as the wire vapour settles. A chain of wire dust particles falling on the charged surface of the disc would be repelled from the surface. In this plate it can be seen that the fibres stand away from the surface and from a bridge connecting the surface to the sharp edge of the electrode, at which point the electric field was at its strongest.

Although the fibres were produced by some mechanism of this type, most of the dust from the wire settles out as a uniform layer over the exposed surfaces, The process is not very efficient, and fibres are only produced where the electric field was at a maximum, and the dust concentration likely to be at its highest.

4.4.3 Blast Induced Damage to Cylinders and Discs

Evidence of the power of, and destruction caused by the blast wave from an exploding wire can be seen in Fig.4.10(a). These cylinders were fractured when the initial energy in the storage capacitor was 610 J. The

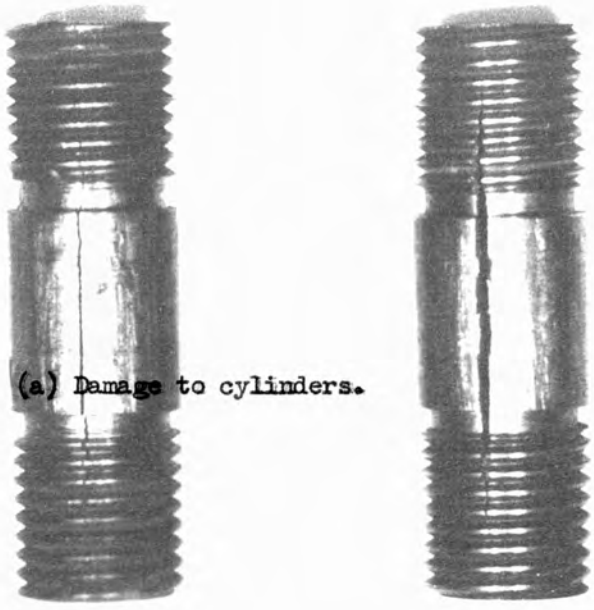

(a) Damage to cylinders.

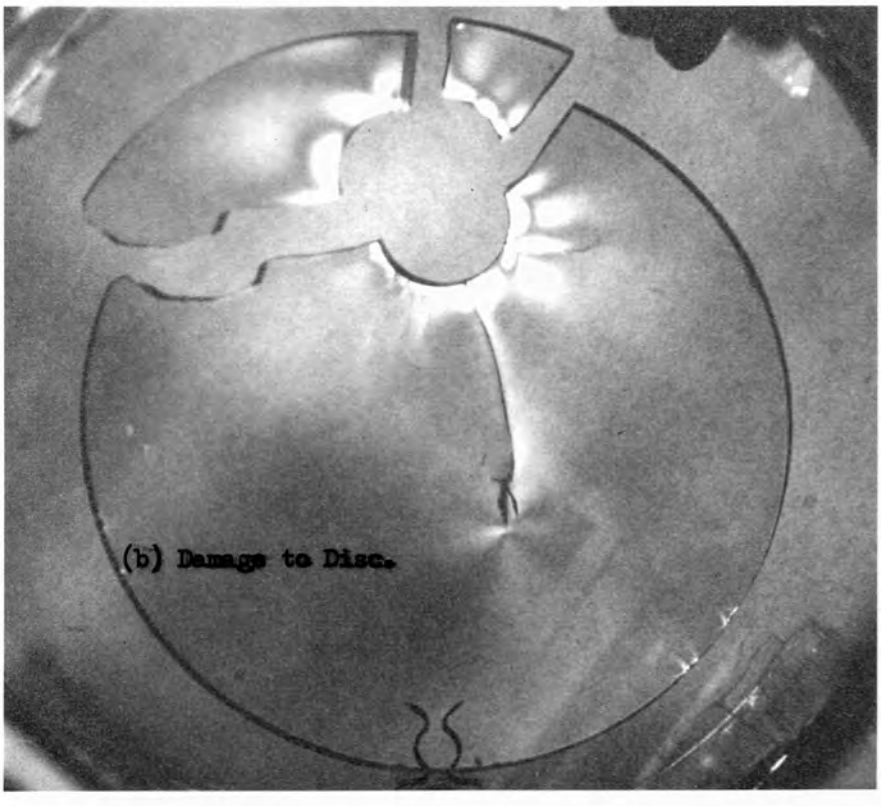

(b) Damage to Disc.

DAMAGE FROM EXPLODING WIRES.

FIGURE 4-10.

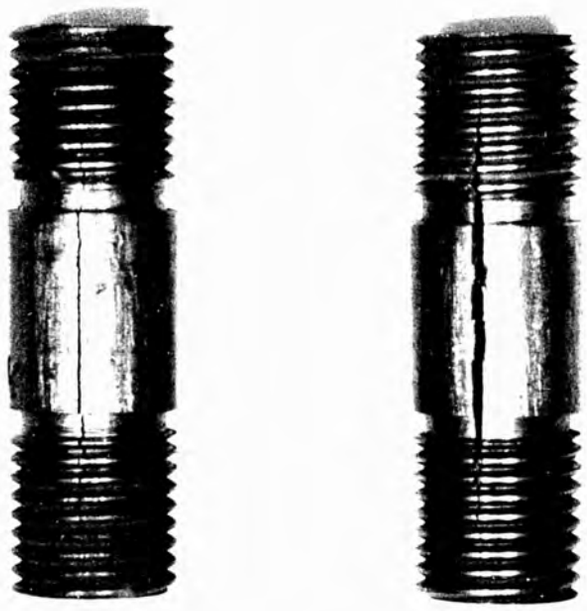

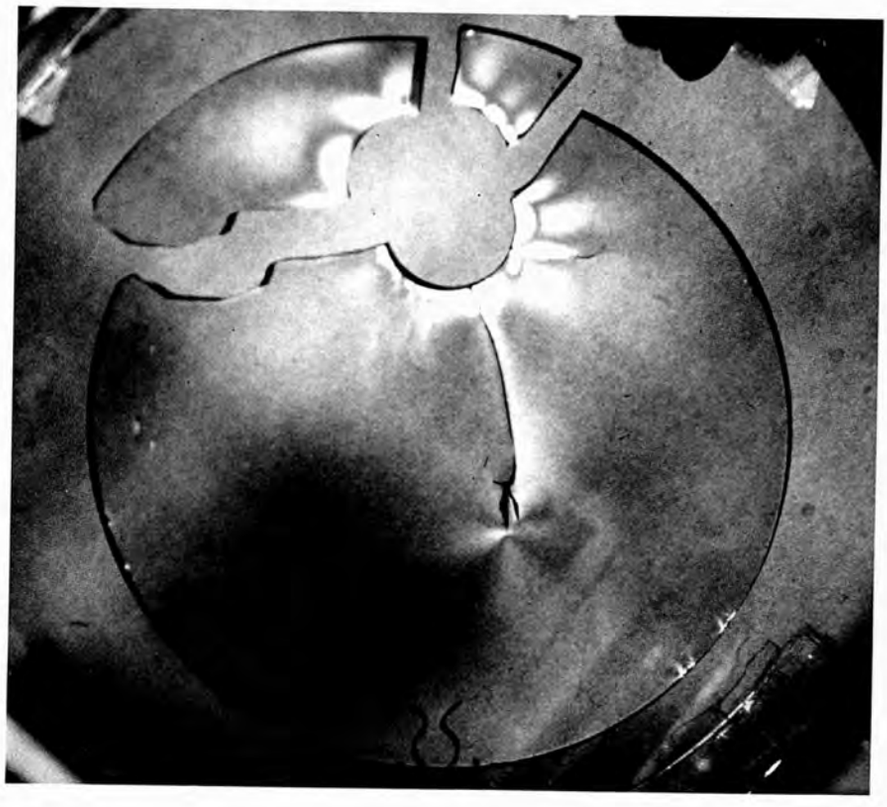

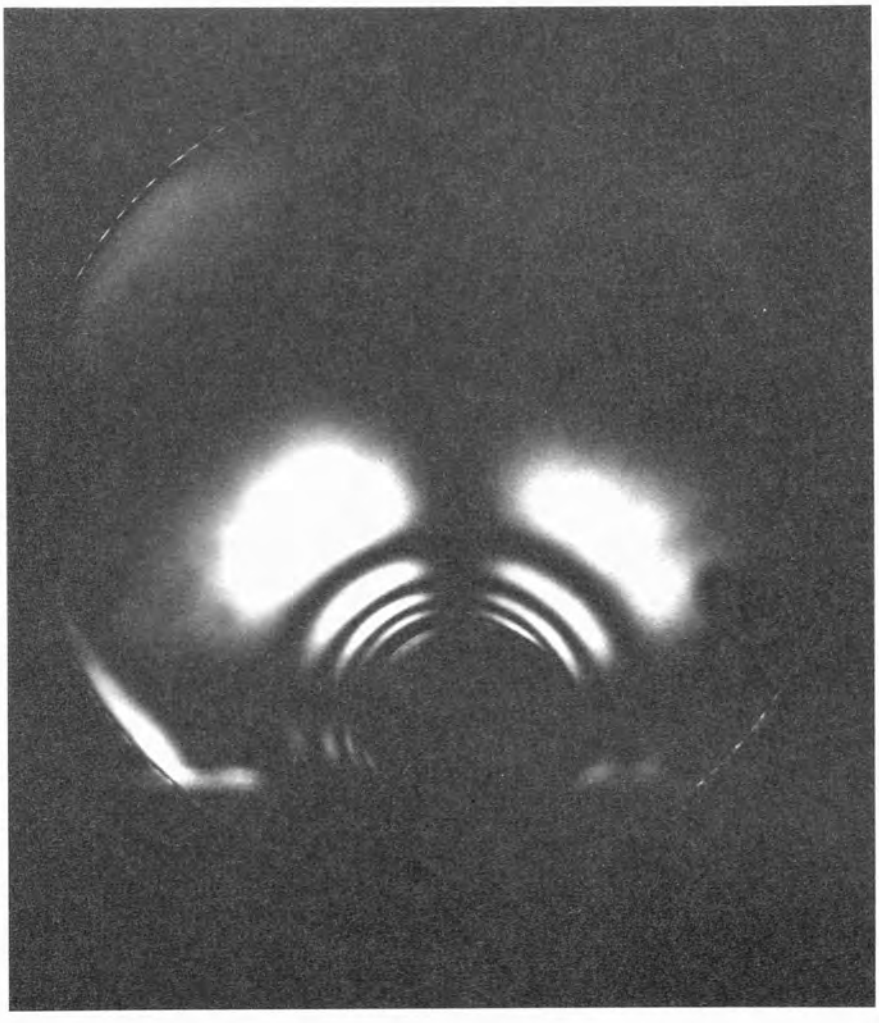

RESIDUAL STRAIN IN PERSPEX DISC.

FIGURE 4-11.

cylinders were made from an extruded mild steel bar from which the centre has been drilled out. Such a bar can contain a weakness along its length from flaws produced during the extrusion process. A cylinder constructed from an imperfectly made bar should split preferentially along the lines of weakness. Fig.4.10(b) shows the damage in the surrounding perspex disc resulting from the fracture of one of the cylinders. The photograph, taken in polarized light, shows the residual strain in the perspex after the fracture.

At lower energies, when the pressure was insufficient to fracture the cylinder, radial plastic flow was observed. It is this flow which, as mentioned in Section 3.4, produces the tight fit of the cylinder into the perspex disc. After a number of explosions, the plastic flow produces a residual strain in the perspex disc (see Fig.4.11). The effect of the strain in the disc produces no permanent damage, and it is only necessary to remove the cylinder in order to release this induced strain. If the hole through which the cylinder is positioned is then enlarged, the system can then be re-used as the perspex fully recovers elastically to its original strain free conditions.

4.5 TIME INTEGRATED PICTURES OF SHOCK WAVES IN A PERSPEX DISH

The optical and electrical systems used in this part of the experiment were described in Chapter III. It was found that in order to produce a visible strain pattern in the perspex disc, it was necessary to increase considerably the energy of the capacitor discharge when exploding the wire, from approximately 100J which was required to produce the explosions in the previous sections of this chapter to ~500J. This higher energy of discharge produced a faster explosion so that the possibility of a non-uniform explosion could be ruled out. The early observations had shown that explosions with more than ~150J in the capacitors, were cylindrically uniform

The increased energy produced a pressure wave sufficiently strong to pass through the steel cylinder into the plate. The resultant strain patterns in the disc can be seen in Fig.4.12; Fig.4.12(a) shows the background illumination of the strain-free plate when the flashlight alone was operated. It can be seen that very little background light is transmitted by the system when the disc is in this condition. When the wire was exploded, the flashlamp was triggered to fire a few microseconds before the start of the explosion, so that the complete stress history was photographed. As the plate settled into its stress-free condition again, no light could pass through the system, so that even if the light flash had been prolonged for longer than the millisecond of its duration, the resultant photograph would have remained unaltered apart from a decrease in contrast.

When taking the photographs, some difficulties were encountered in producing sufficient contrast on the photograph. The P.300 plates which were used did not have high contrast, and the use of H.P.3 did not lead to much improvement.

The five plates shown in Fig.4.12, 4.13 and 4.14(a) cover the energy range 320J→610J. The lighter areas are areas of greater strain. When interpreting the pictures it must be remembered that strain in the direction parallel to the polarization of the light does not produce optical rotation. This is demonstrated by the radial dark areas in Fig.4.11. In the plates, the plane of polarization is as indicated, at forty-five degrees to the diameter of the disc through which the wire passes. In spite of the great range of discharge energies used, the general features of the resultant strain patterns are common to all the explosions. There appear to be lines of maximum and minimum stress parallel to the edge of the disc at the '3 o-clock' and '9 o-clock' positions. In the mirror image position to the exploding wire these areas come together in a diffuse area of maximum stress. Axial symmetry across the diameter which includes the wire can be seen to exist in all these cases.

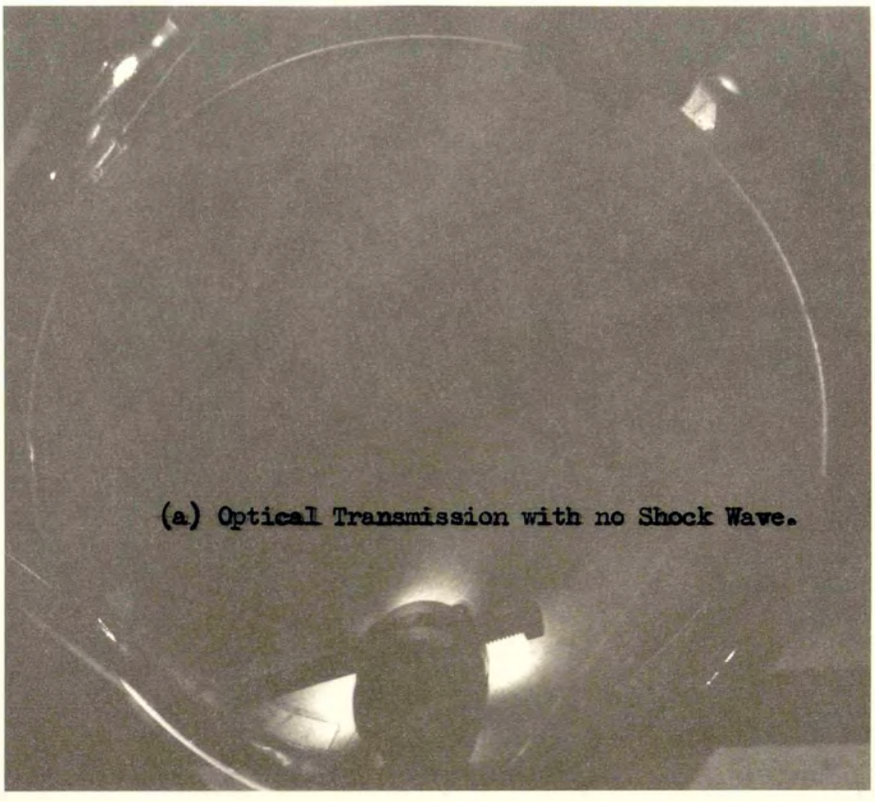

(a) Optical Transmission with no Shock Wave.

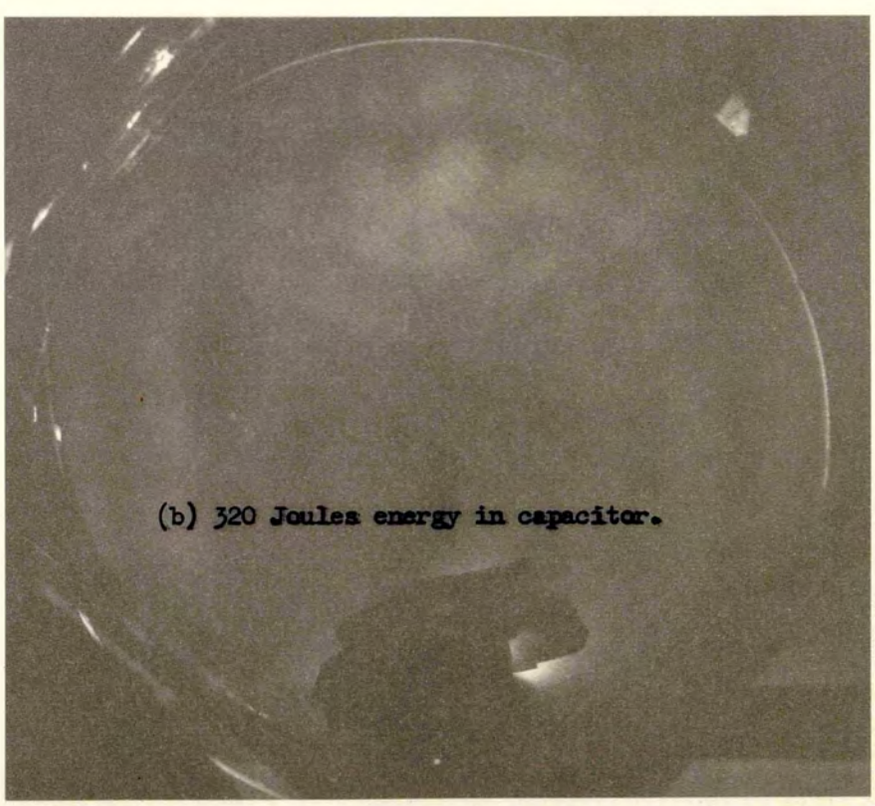

(b) 320 Joules energy in capacitor.

SHOCK WAVE STRAIN IN PERSPEX DISCS.

FIGURE 4-12.

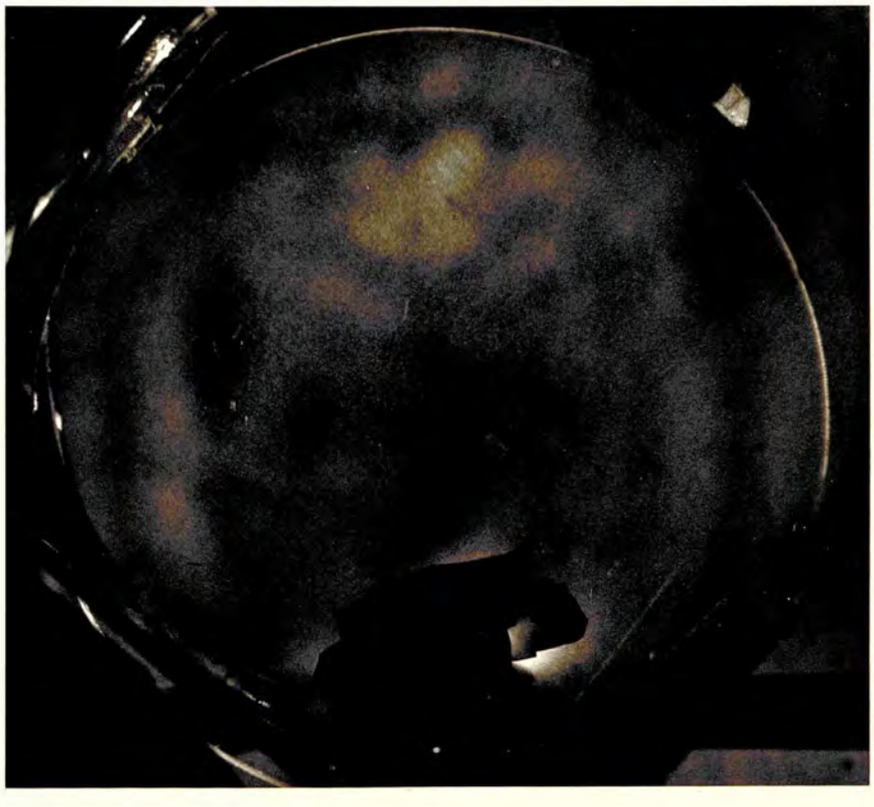

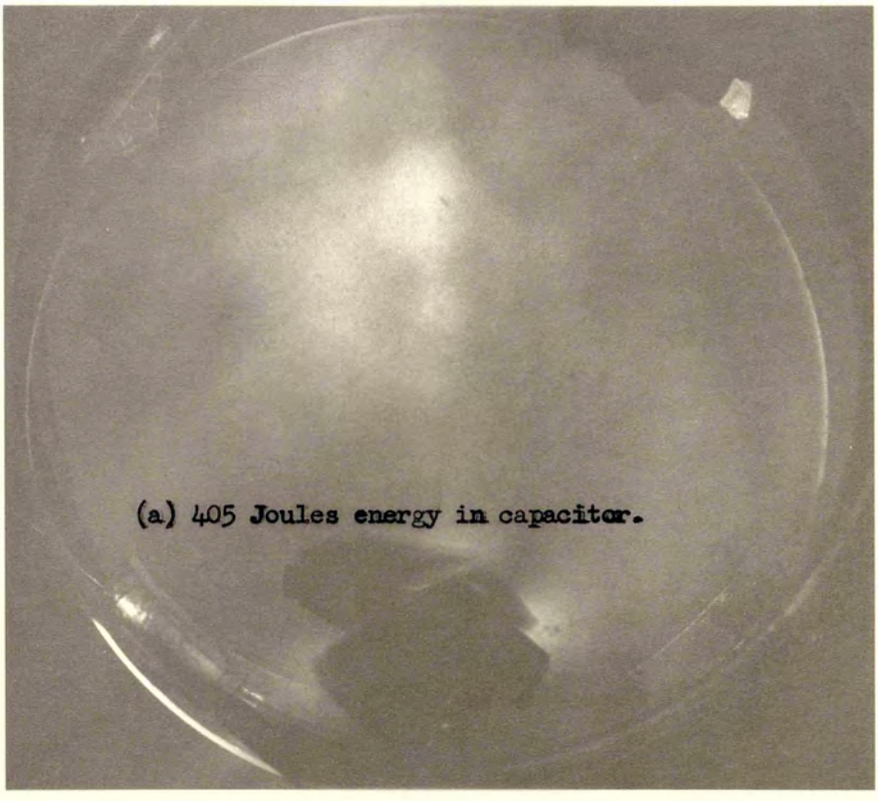

(a) 405 Joules energy in capacitor.

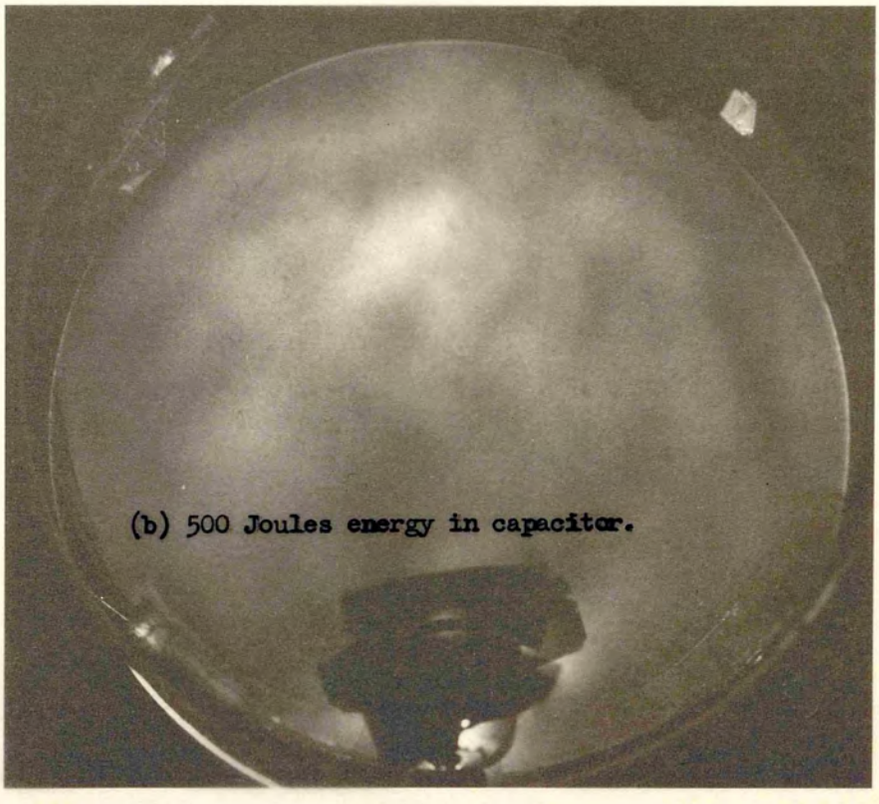

(b) 500 Joules energy in capacitor.

BI-REFRINGENCE IN PERSPEX DISCS PRODUCED BY SHOCK WAVES.

FIGURE 4-13.

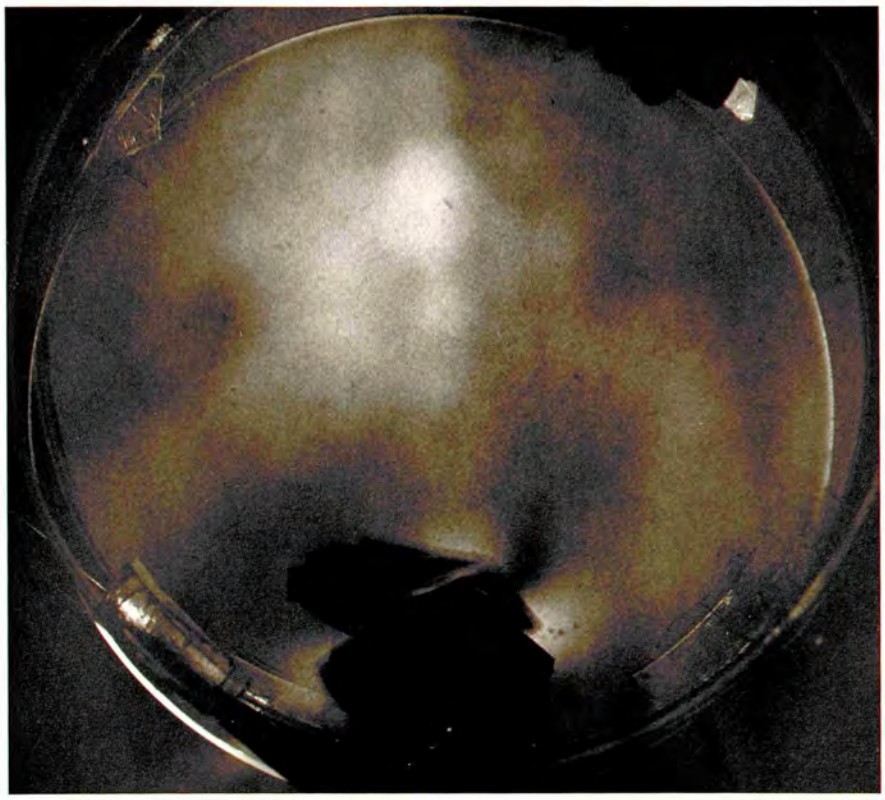

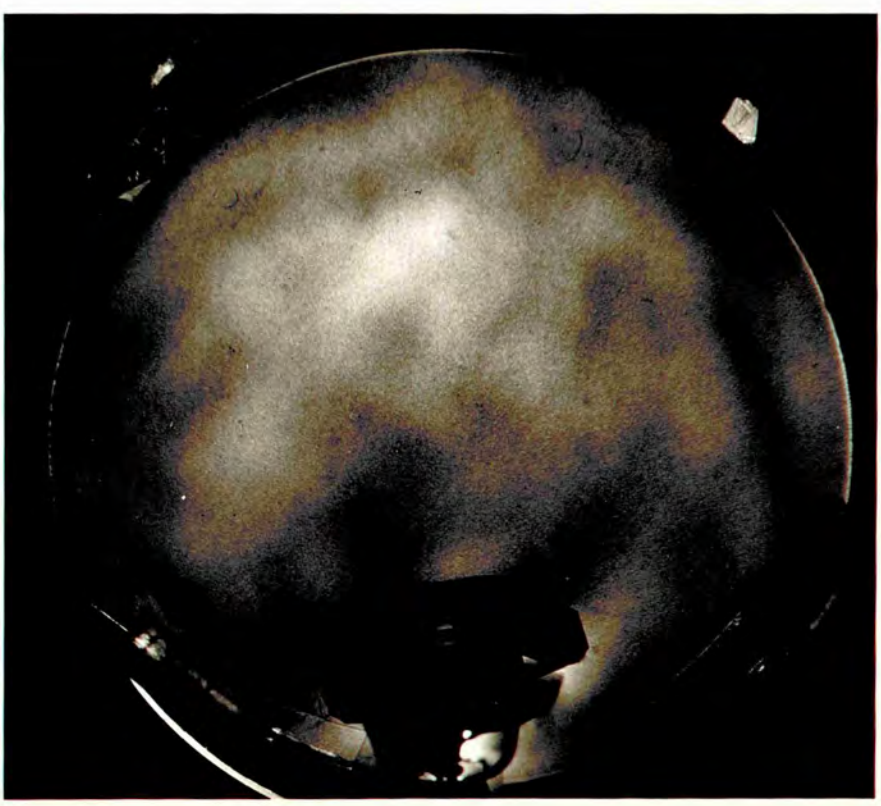

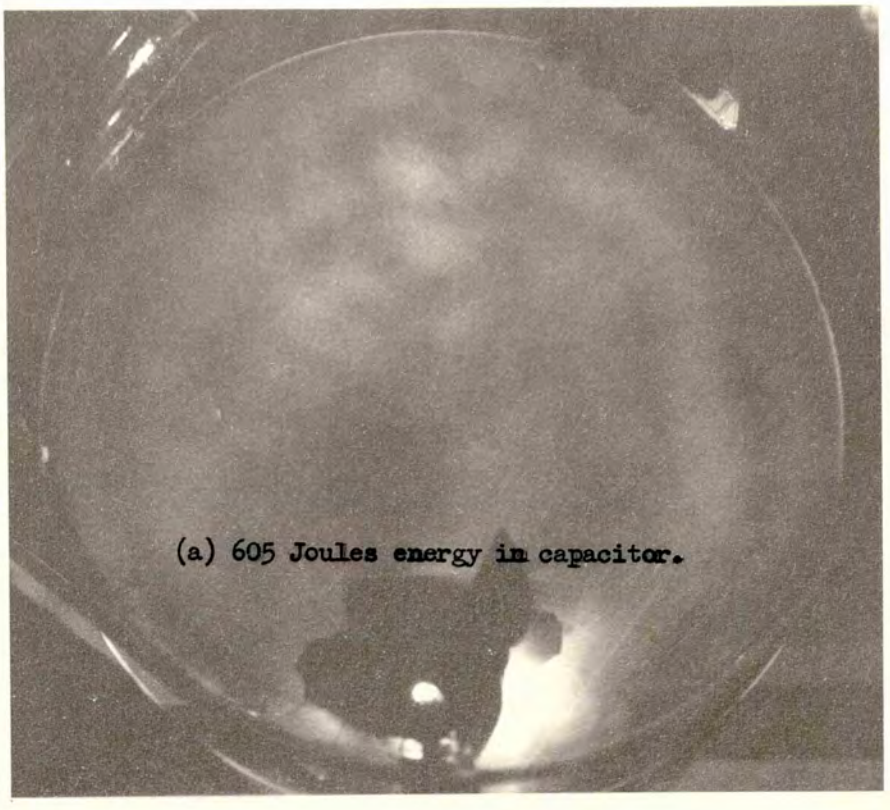

(a) 605 Joules energy in capacitor.

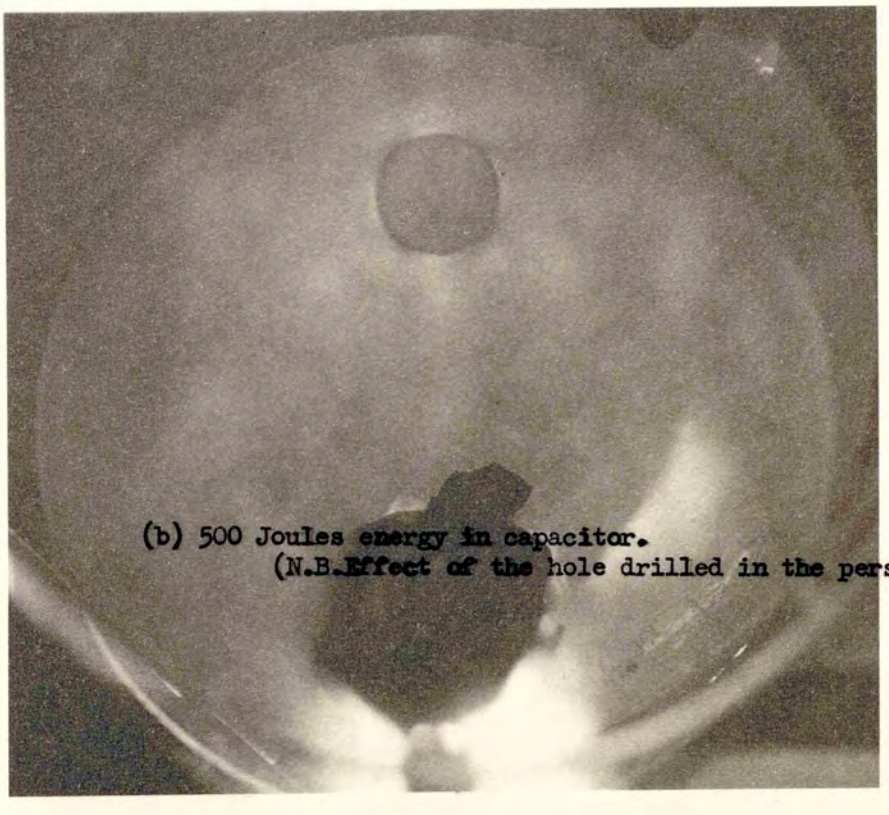

(b) 500 Joules energy in capacitor.
(N.B. Effect of the hole drilled in the perspex)

SHOCK INDUCED BI-REFRINGENCE IN PERSPEX DISCS.

FIGURE 4-14.

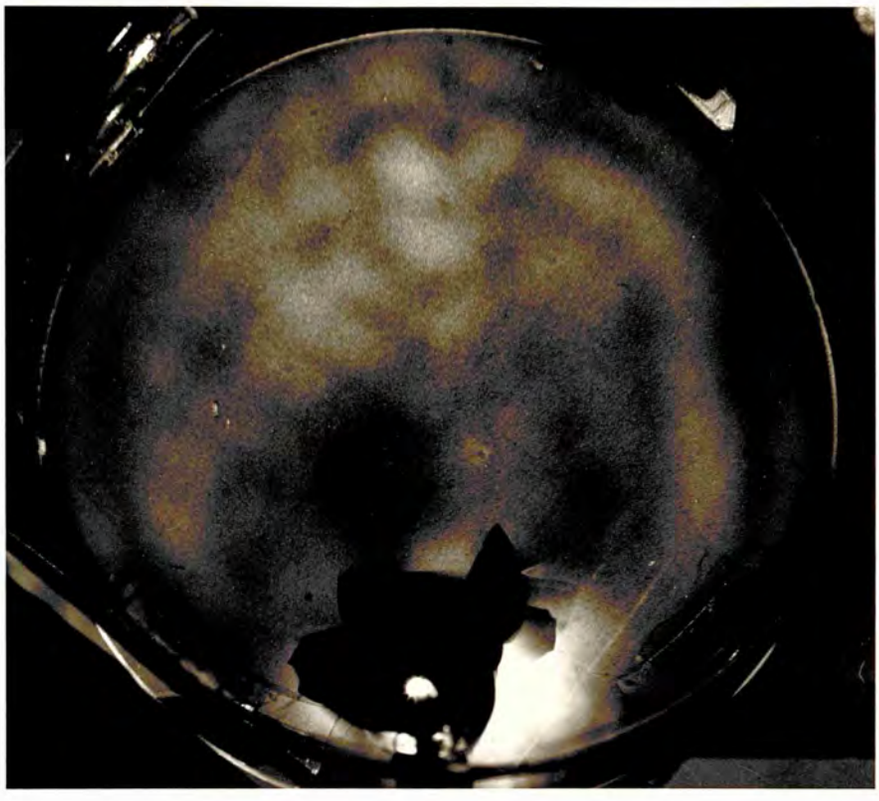

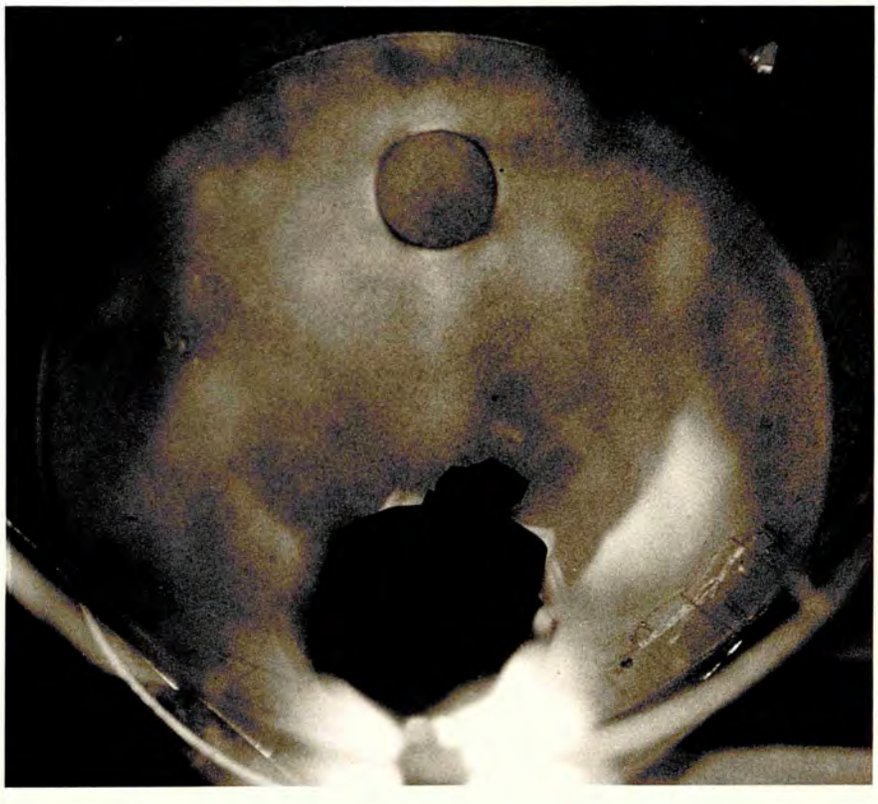

The main problem which these results create is that of determining whether the strain patterns are indeed time-integrated photographs of the shock wave paths, or merely the stress patterns created in the plate when it is set into oscillation by the force of the explosion. In this case the steel cylinder would initially provide the impulses, but would tend to act as a damping force during the period of the oscillations and would thus be situated at a node. Fig.4.14(b) however, shows the same main strain pattern with a hole drilled in the disc at the point where the maximum stress is expected. If the strain pattern was caused by oscillation this change in geometry should alter the outline of the pattern. As the change to the strain is not very great, it can be concluded that the stress was created by the action of a dynamic shock wave passed along the plate.

CHAPTER V

DEVELOPMENT OF A HIGH SPEED OPTICAL SHUTTER

5.1 REQUIREMENTS FOR A SHUTTER

The results of the initial studies with exploding wires and a single pulse of light with which to illuminate and photograph the shock waves show that such a system, whilst it shows the areas in the plate under maximum stress, gives insufficient information about the path of the shock wave. Although all the information is recorded on the photograph, interpretation is difficult and a high time resolution is required. Ideally, a series of short exposures ($< 1\ \mu s$) is needed so that a complete picture showing the development of the shock wave can be recorded.

Typical shock wave velocities in perspex are $\sim 5 \times 10^3\ m.s^{-1}$ (17), and thus to produce a series of exposures during which the wave has moved an appreciable distance, the separation between the exposures needs to be $\sim 1\ \mu s$, with the individual exposures themselves being more than one order of magnitude smaller than this. Ideally, about four or five exposures would be required so that the rate of change of velocity of the wave can be accurately measured as well as its path.

One of the fast image converter cameras which are at present available on the market is well suited to this. Such a camera was not obtainable, but adaptations of electro-optical shutter are equally suitable for such a situation, although a very much greater light intensity is required. High light intensities are fortunately available with the advent of the laser, otherwise it would be necessary to achieve the required intensity by using a single triggered flashlamp gated by the rapidly switched electro-optical shutter. The use of a laser has certain advantages, although it cannot be used for the photography of self-luminous events in the way that the image converting camera can be used.

The first advantage of a laser is its highly collimated beam which reduces the number of optical components required and makes for ease of alignment. Secondly, if a continuous laser is used, only a single device needs to be triggered in order to produce the rapid train of light pulses. The use of either the flashlamp system or a pulsed laser would require two triggering pulses; one to switch the light source, and the second to trigger the electro-optical shutter. Such difficulties can, of course, be overcome but the simplicity of a single continuous laser circumvents these problems altogether.

5.2 THE KERR CELL

The Kerr electro-optical effect was first observed by Kerr in 1895. It is the effect whereby many liquids under the influence of an electric field, behave as uniaxial crystals with the optic axis parallel to the line of the field. The observed birefringence can be calculated from the equation introduced by Kerr :

$$n_1 - n_2 = k\lambda E^2 \qquad \ldots (5.2.1)$$

From this we see that the angular phase displacement of the two polarizations of the emergent light = δ, where

$$\delta = 2\pi k L E^2 . \qquad \ldots (5.2.2)$$

The phase difference depends on the length of the interaction area, and on the strength of the applied field. If the incident light is initially polarized at 45° to the applied field with the analyser set at 90° to the plane of polarization, then the intensity of the transmitted light[111,112] is given :

$$I = I_0 \sin^2 (\pi k L E^2). \qquad \ldots (5.2.3)$$

The field required to produce a rotation of the plane of polarization by 90° (i.e, $\delta = \pi$) is given :

$$E = \frac{1}{\sqrt{2\pi L}} . \qquad \ldots (5.2.4)$$

The shutter is usually switched by a single square voltage pulse. The

most usual liquid used in the Kerr cell is nitrobenzene, this has a high resistance only when in a state of extreme purity. The Kerr constant for nitrobenzene is relatively large (2.2×10^{-5} e s u) , but more important for Kerr cell shutters, is the speed at which the liquid switched. For polar molecules, where the effect changes the moment of the molecules and where there is some re-orientation of the molecules, the delay between the application of the electric field and the observation of the Kerr effect may be of the order of a few seconds. For nitrobenzene the time taken to switch is $\sim 10^{-11}$ secs . In nitrobenzene the mechanism of the effect is slightly different, and the induced electric moment is caused by the applied field distorting the molecules.

Studies of extremely fast switching speeds have been made when the cell is switched by the electric field from a short high power optical pulse[113]. The cell is probed by a second beam with a frequency different from that of the switching pulse. As the switching and probe beams are coaxial, a filter is placed over the detector so that the switching beam is not detected. Mode-locked neodymiun lasers have been used to switch off the probe beam at the second harmonic frequency. By this method the very fastest relaxation times can be measured. The most rapid switching mechanism is the Kerr effect produced by distortion of the electron cloud within the molecules. This is the mechanism at work in carbon disulphide, where the relaxation time is of the order of 1.8 p.s.

5.3 METHOD FOR PRODUCING A NUMBER OF RAPID LIGHT PULSES USING A KERR CELL

Two methods are considered here for producing a number of rapid pulses. A d c - biased Kerr cell[114] can be made to operate giving a continuous modulation if a radio frequency signal is imposed on top of the d c. A large d c bias reduces the amount of power needed at radio frequency, but heating effects can be serious unless the nitrobenzene is very highly

purified. If impure nitrobenzene is used, the voltage required to cause electrical breakdown is considerably reduced. When the cell is filled, if any small air bubbles become trapped in the liquid, the bubbles can become agitated in the presence of the applied voltage, and cause electrical breakdown. If the equations for the transmitted light are modified to include the radiofrequency modulation on top of a d c bias the expression for $I_{max/mod}/I_o$ includes terms in 2ω as well as ω.

Modulation $> 50\%$ for the fundamental can be obtained from a suitable d c bias with r f modulation of only 15% of the d c extinction voltage; with the same r f voltage and at a higher d c bias it is possible to obtain second harmonic modulation $> 20\%$.

This technique, however, requires the use of an r f generator capable of producing $> 10^3$ V r f, and if the necessary purity of the nitrobenzene cannot be obtained, the current requirements are considerably increased. It is necessary in this case to produce a Kerr cell with a built-in cooling system, as the Kerr constant is temperature dependent. The second technique avoids some of these difficulties. In this technique, which was tested experimentally, a pulsed voltage was put into the cell. In this manner the cooling system was made redundant, and although a high breakdown voltage was still needed, the presence of residual conductivity in the cell was not as disadvantageous as would have been the case with the cell held at a constant d c bias.

We have seen that the transmitted light intensities is E^2 dependent ($I = I_o \sin^2(\pi k L E^2)$), thus if the voltage across the cell is raised above the value for the first minimum transmissivity, a number of further transmission maxima could be obtained. Thus if the cell is held at a very high voltage and rapidly earthed, the transmitted light will pass through a number of maxima to give a series of pulses. Obviously the application

of a single voltage pulse of this value will produce twice this number of pulses as the field rises and falls. Ideally the applied voltage would need to be parabolic in order to give a regular series of equally long pulses, but this is not a vital consideration.

In such a situation, the main problems that are encountered result from the compromise which is necessary in applying such a large voltage at speed. The required value of the applied voltage may be reduced if the length of the Kerr cell is increased, but this can only be done at the expense of increasing the capacitance of the Kerr cell. The ideal cell incorporates both these properties. A number of novel electrode geometries within the cell have been investigated with the view to reducing the capacity of the cell whilst producing a high field from a relatively low applied voltage.

5.4 PRODUCTION OF A HIGHLY NON-UNIFORM FIELD - THEORETICAL CONSIDERATIONS

We consider here the electric field between a single, thin charged wire at a distance (h) from an earthed conducting plane. The problem is best considered by the method of images, the thin line of charge has an electrical image at a distance (h) on the opposite side of the conducting plane.

Let each wire have radius (a) so that $2h \gg a$ (see Fig.5.1), and let the charge per unit length be $+\sigma$ and $-\sigma$ respectively. The field X_p at P due to one of the wires (see diagram) is given:

$$X_p = \frac{2\sigma}{\epsilon r} \qquad \text{(by Gauss theorem)} \quad .. \quad (5.4.1)$$

$$V = -\int X dr \,. \qquad \ldots \quad (5.4.2)$$

The potential at P due to one wire A is:

$$= -\frac{2\sigma}{\epsilon}\int_R^r \frac{dr}{r} = -\frac{2\sigma}{\epsilon}(\log_e r - \log_e R) \qquad \ldots \quad (5.4.3)$$

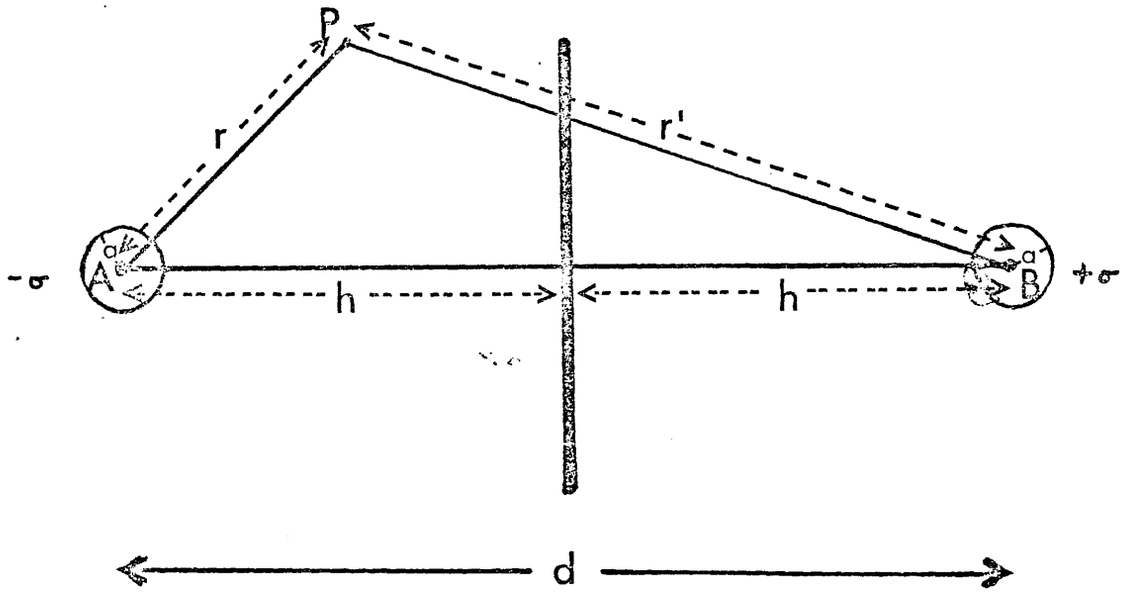

FIGURE 5-1.

Similarly, the contribution to the potential at P from wire B is:

$$\frac{2\sigma}{\epsilon}(\log_e r' - \log_e R) . \qquad \ldots (5.4.4)$$

Hence the combined potential at P,

$$V = \frac{\sigma}{\epsilon} \log_e \left(\frac{r'}{r}\right)^2 \qquad \ldots (5.4.5)$$

But

$$r'^2 = r^2 + d^2 - 2rd\cos\theta . \qquad \ldots (5.4.6)$$

$$V_p = \frac{\sigma}{\epsilon}\left\{\log(r^2 + d^2 - 2rd\cos\theta) + 2\log r\right\} \qquad \ldots (5.4.7)$$

The field E is related to V_p by:

$$E = -\nabla V_p . \qquad \ldots (5.4.8)$$

In rectangular cartesian coordinates with the origin at B, and AB = x - axis, $x = r\cos\theta$, $y = r\sin\theta$, $x^2 + y^2 = r^2$.

$$V_p = \frac{\sigma}{\epsilon} \log_e \left(\frac{y^2 + (x-d)^2}{x^2 + y^2}\right) \qquad \ldots (5.4.9)$$

$$\nabla V_p = - E_p = \frac{2\sigma}{\epsilon}\left\{\left(\frac{x-d}{y^2 + (x-d)^2} - \frac{x}{(x^2 + y^2)}\right)\hat{i} + \left(\frac{y}{y^2 + (x-d)^2} - \frac{y}{(x^2 + y^2)}\right)\hat{j}\right\}$$

$$\ldots (5.4.10)$$

$$|E_p| = \sqrt{E_{px}^2 + E_{py}^2} \qquad \ldots (5.4.11)$$

therefore

$$|E_p| = \frac{2\sigma d}{\epsilon}\left[(x^2 + y^2)\left\{y^2 + (x-d)^2\right\}\right]^{-\frac{1}{2}} \text{ e.s.u.} \qquad \ldots (5.4.12)$$

This expression gives the strength of the electric field at any point in the Kerr cell when a charge of σ per unit length is held on the wire.

The capacitance[115] per unit length is

$$C = \frac{\epsilon}{4\log_e (d/a)} \qquad \ldots (5.4.13)$$

Then the applied voltage r can quite easily be expressed in terms of σ.

The intensity of the light transmitted at any point in the cross-section of the Kerr cell is I, where:

$$I = I_o \sin^2 \left\{\frac{4\sigma^2 \pi k L d}{\epsilon^2}(x^2 + y^2)(y^2 + [x-d]^2)\right\} . \qquad \ldots (5.4.14)$$

Thus lines of equal values of E^2 (electrostatic isodynes) correspond to lines of equal Kerr switching. Lines of constant electric field ($\nabla E = 0$) are plotted corresponding to values of E so that $\delta = 2\pi, 4\pi, 6\pi \ldots$. In Fig.5.2 these graphs are shown for two values of the voltage (v). The isodynes in these figures correspond to areas where the minimum light is transmitted through the cell.

The graphs in Fig.5.2, which are for an electrode geometry consisting of a wire and a plate, can quite easily be extended to describe the experimental cell. In the experimental arrangement, the plane electrode remains in position as in the theoretically determined case. The thin wire electrode is replaced by a long razor blade with its edge towards the plane. On the razor blade, the strongest field is on the surface at the position of maximum curvature, i.e. the field is at the tip, the electrical image of the blade thus corresponds to the long thin wire with a line of charge producing a strong field along the razor blade tip. This is an idealized situation. Obviously the electrode mountings will produce some distortion to the isodyne structure in the region behind the tip of the blade. However, in the region between the razor blade and the plane electrode, this distortion will be very much less. As this region is the useful part of the cell, the equivalence of the razor blade and wire in this region makes this approximation taken in the calculation, a valid one.

The movement of the isodyne when an increasing voltage is applied to the system is such that a series of maximum and minimum light transmission fringes sweeps across the field of view. Using Fig.5.2(b) for a demonstration, the isodynes shown on this plate are for equal increasing increments of E^2 so that $E^2 = k$ on A and A′; 2k on B, B′; 3k on C, C′ and 4k on D. As the field is increased, an isodyne starting as a small circle (D) just around the position of the knife-edge (Y) expands radially outward. As the voltage is further increased the isodyne distorts and

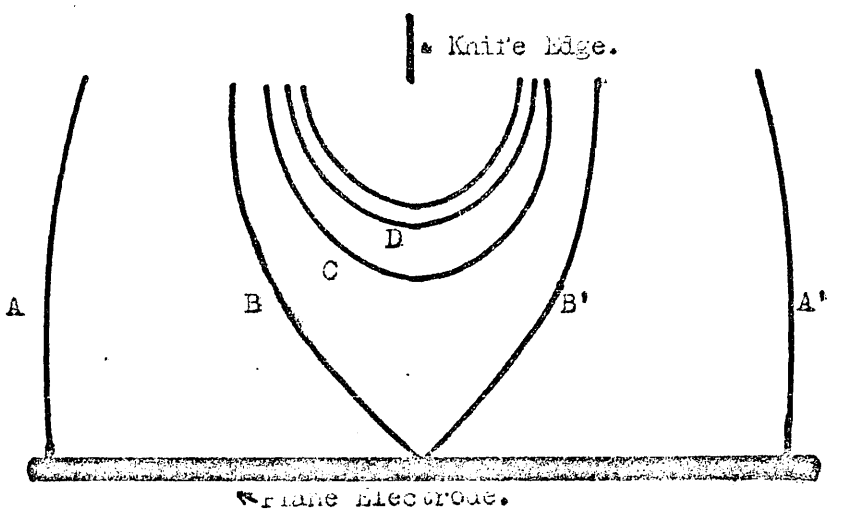

(a)

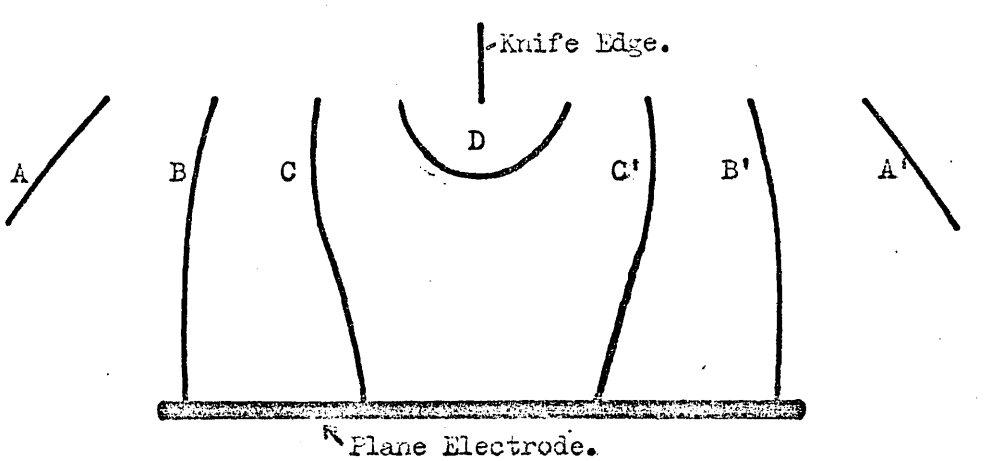

(b)

LINES OF EQUAL FIELD AROUND A KNIFE EDGED ELECTRODE.

FIGURE 5-2.

divides into two separated lines (C and C′) so that it makes contact normally with the earthed plate (X). The two halves of the isodyne moves outward across the surface of the plate (B B′) and finally separate from it (A,A′). From these graphs it can be seen that the area of most uniform field is the region just off the surface of X and immediately opposite Y, for it is here that the isodyne spacing is at a maximum. The area with the strongest electric field is just off the tip of the knife-edge Y, but at this point the isodyne spacing is very small and the radial rate of change of (E) is at its highest.

At the tip of Y the field is at its maximum and it is here that electrical breakdown of the dielectric will take place preferentially. This can be avoided if (Y) is replaced by a conductor whose surface is situated along the line of one of the isodynes. As these are approximately cylindrical around the point Y, the use of a cylindrical electrode will produce approximately the same isodyne configuration across the rest of the field of view.

5.5 DESCRIPTION OF EXPERIMENTAL KERR CELL

A number of Kerr cells were constructed to take advantage of the high fields created in the highly non-uniform situation described in the previous section.

(1) A Kerr cell was constructed in which one of the normal electrode plates had been replaced by a knife edge. This electrode was made from two razor blades mounted in contact and end to end. This produced an edge 7.2 cms long. The razor blades, whose edge radius of curvature was 50 nm were made of stainless steel with a nickel edge coating. The plastic surface coating normally put on these blades was not present in this case.

The electrode configuration had the usual plane cathode, the anode was positioned with the edge facing the cathode and parallel to it.

A beam of plane polarized light was passed through the cell parallel to the knife edge and with the plane of polarization making an angle of 45° to the surface of each of the two electrodes, these surfaces being at right angles to each other. The knife edge anode was fixed on a moveable mount so that the electrode separation in the cell could be adjusted. A photograph of the cell is shown (Fig.5.3).

Within the region between the electrodes, the electric isodynes for this geometry are identical to the lines computed in the previous section, the greatest field being just above the surface of the knife edge. It is at this point that any breakdown in nitrobenzene is likely to take place. The cell was constructed from high density polythene, the end windows were sealed on to the cell by the means of metal tie-bars running the length of the cell. These bars served to pull the glass down on to the knife-edged ridges which had been turned on the end of the body of the cell. This rendered the system liquid-tight. The cell was mounted on a horizontal table which could be adjusted in all directions and rotated about a vertical axis. Filling the cell was facilitated by two filling holes in the top of the cell. These holes were tapped so that a specially made funnel could be screwed down into the cell through one of the holes. The second hole acted for pressure release. The holes were afterwards sealed by means of stainless steel screw stoppers. In assembling the cell it was necessary to take care to protect the sealing ridges on the ends of the polythene. These were liable to damage and thus allow the leakage of nitrobenzene from the cell. When the cell was dismantled it was necessary to remake the ridges before the cell could be refilled, as the deformation produced by the pressure as the windows were pulled tight, was permanent.

(2) A bi-cylindrical Kerr cell was constructed. This cell had several improvements over the knife-edged cell. The two electrodes were parallel cylinders and thus the positions of the lines of constant electric field were in essence the same as for the knife-edged Kerr cell (see Fig.5.2).

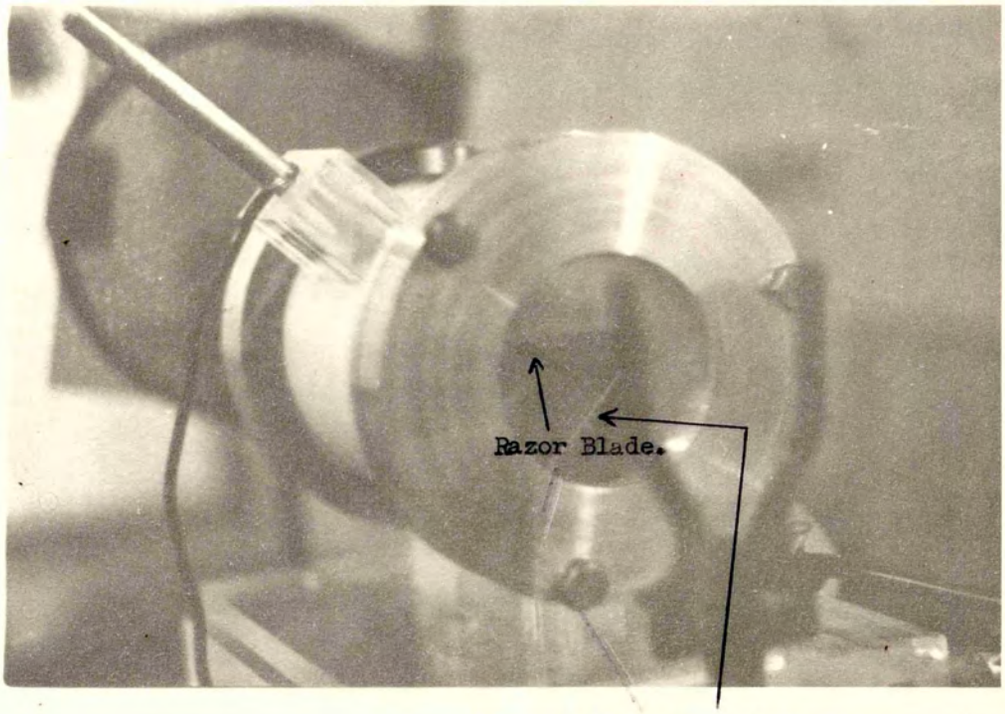

KNIFE-EDGED KERR CELL.

FIGURE 5-3.

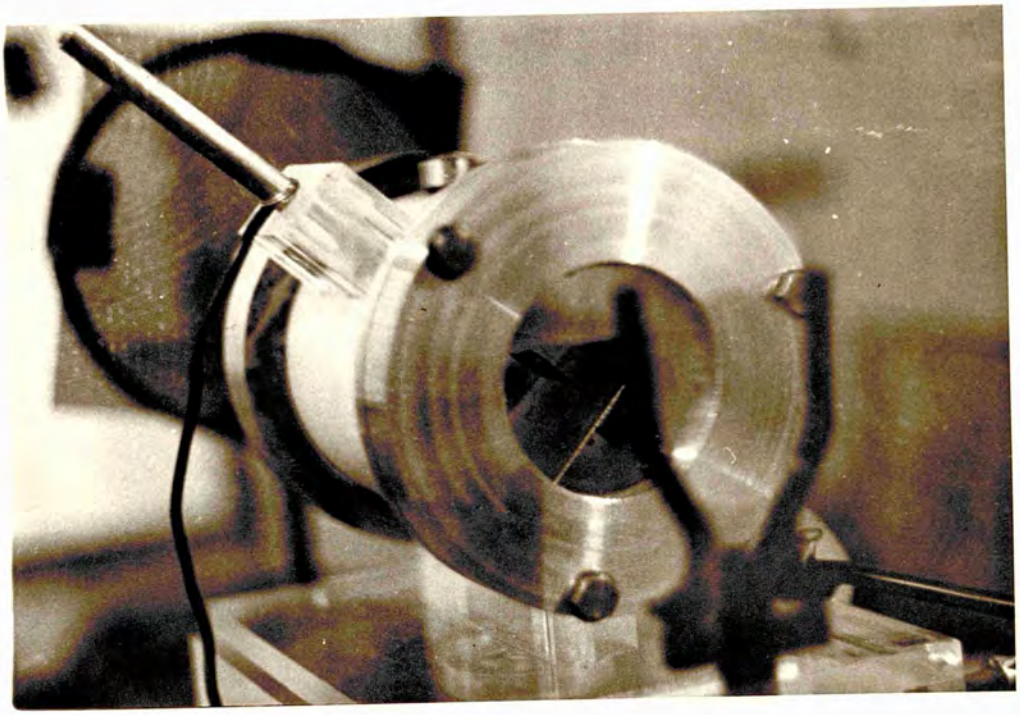

As the area of very high electric field immediately at the tip of the razor in the knife-edged cell had been liable to give rise to electrical breakdown in the nitrobenzene, this problem no longer existed. The larger radius of curvature of each of the cylinders (0.4 cm) made the most intense electric fields unobtainable. This, however, was of no disadvantage as the area of extremely high field at the razor edge was too small to use. This cell was constructed of PTFE ,, the stainless steel cylinders and end caps were cleaned electrolytically and sealed on to the ends of the PTFE body by cooling the PTFE in liquid nitrogen and force fitting the ends while the body was still in a state of contraction. This produced a completely leak-proof fit. The end windows were fitted to the end caps by being screwed on to a PTFE knife edged sealing ring which was sunk into the steel endplates. The PTFE provided a far better seal than the high density polythene used in the previous cell, and no difficulties of leakage were encountered.

The area of the cell used for Kerr switching was the area around the mid-point between the cylinders. At this point the field is at its most uniform.

The length of the cell was 12 cm which was larger than the knife-edged cell and had the advantage of reducing the field required to produce a given rotation of the polarization of the probing beam. The volume of the cell was cut to a minimum thus reducing the amount of nitrobenzene required. The distance between the cylinders could be chosen and altered when the end caps were placed on the cell. By rotating one of the end caps, the cylinders moved closer together. The maximum distance between the cylinders was 1.0 cms .

5.6 SOME ADVANTAGES AND DISADVANTAGES OF THE MODIFIED KERR CELLS

The advantages of these cells stem from the non-uniform field distribution, and with the knife-edged cell it is possible to produce fields several times greater than would be possible if the same controlling voltage were to be applied to a conventional Kerr cell. Unfortunately the area of very high field is exceedingly small, and the most useful part of the cell is further away from the edge of the razor blades. Indeed, the strong field right at the tips of the blades can be a positive disadvantage because when applying to the cell a voltage which is high enough to produce an effective field in the useful area of the cell, the field at the tip of the razor blade can exceed the breakdown voltage. The modification using cylindrical electrodes solves this problem.

The area of the cell where the field distribution is at its most uniform is midway between the electrodes, but uniformity extends only over a very small region. This is why it is necessary to use a highly collinated laser beam, because any part of the beam off the axis of the cell is switched by a slightly differing amount. At the midpoint between the electrodes of the cylindrical cell the field strength per unit applied voltage is identical to that in a conventional plane electrode Kerr cell. In terms of field strength there is no advantage in using cylindrical electrodes. There is, however, a second advantage which we have not yet considered and that is the reduced electrostatic capacity which is a property of these cells. Hence there is a greater ease of applying a rapidly changing controlling voltage pulse to these cells.

The effectiveness of the cell as a shutter for optical imaging is reduced because of the small useful area of the cell's cross-section. The cell is more useful for switching an illuminating light source, as a distortion in these wavefronts does not effect the final imaging in a

camera. This restriction leads to the result that if the cell is to be used in a photographic system, it cannot be applied to the photography of self-luminous events.

The advantages of a system whereby the Kerr cell is triggered to pass a series of light pulses when only a single voltage pulse is applied, are clear. A single pulse may easily be applied by, for example, a capacitor discharge; whereas if one voltage pulse per light pulse was required, a more refined system would be needed. The shaping and the separation of the switched light pulses can be adjusted by changing the shape of the applied voltage pulse. A regular, uniform series of pulses is not always an advantage. In the case of accelerating motion, more accurate measurements of the acceleration may be determined if the light pulses are spaced so as to produce a more rapid switching as the motion speeds up. In the case of a slowing shock wave, for example, the reverse is the case. As the wave slows down a greater time gap between the adjacent pulses is an advantage. This is the shape of the output when the applied voltage is produced from a capacitor discharge.

5.7 EXPERIMENTAL INVESTIGATION

The experimental investigation into the modified Kerr cells was divided into two parts:

(i) An investigation of the field structure in the cell as demonstrated by the Kerr effect;

(ii) The examination of the optical switching properties of the cells.

(i) The field structure in the knife-edged Kerr cell was thoroughly examined. The apparatus (Fig.5.4) used, consisted of a Universal Laboratories He-Ne laser with an output power of 2-3 mW, giving plane polarized light at 632.8 nm wavelength. The beam of light was broadened to 2 cm diameter by use of a microscope objective, and collimated so that the beam

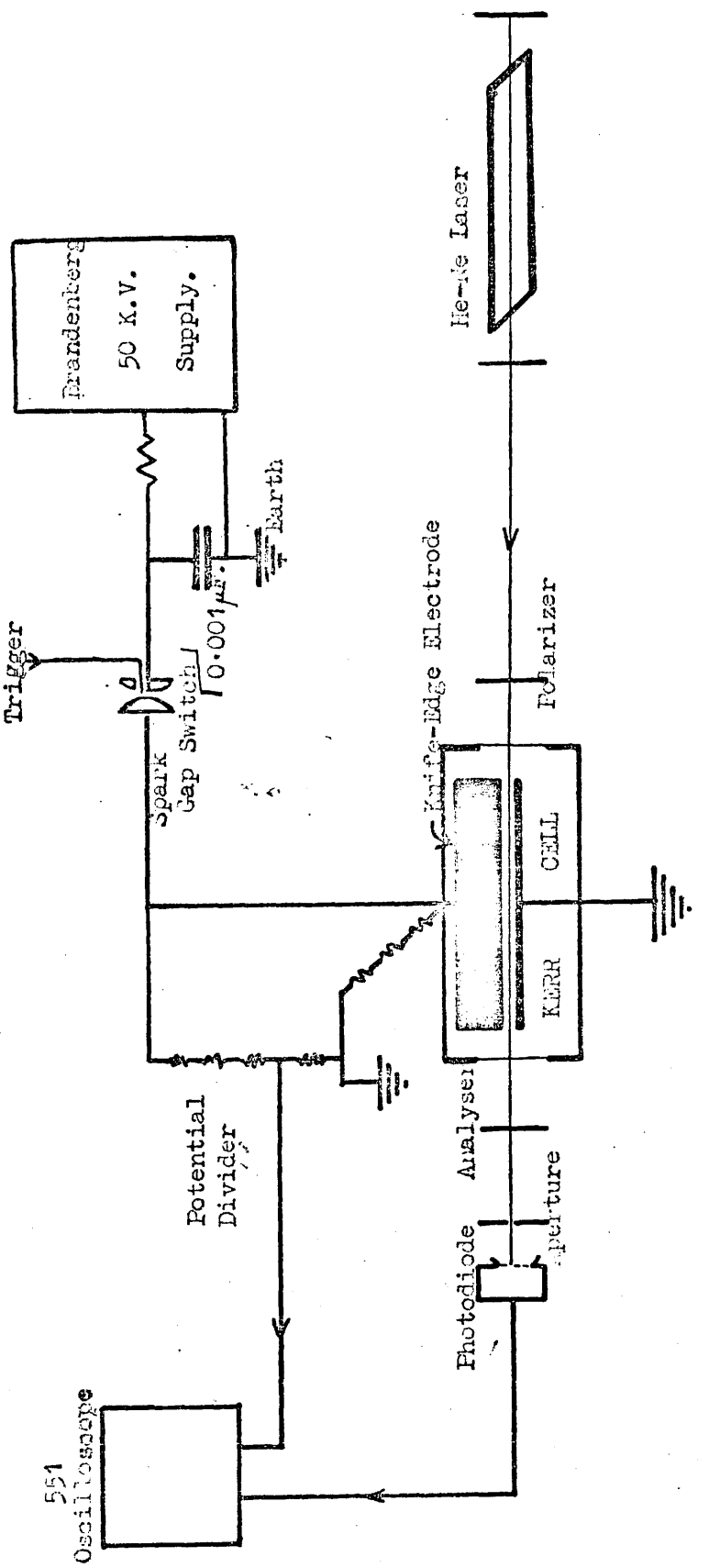

KNIFE-EDGED KERR CELL: TRAIN OF TRANSMITTED LIGHT PULSES.

FIGURE 5-4.

passed down the cell illuminating the complete cross-section of the cell including the electrode structure. Initially the resistance of the cell was measured for differing separations of the electrodes. It was found that the resistance of the cell could be increased by applying the voltage with a gradual build-up over the period of a few hours until the maximum voltage was reached. This apparently results in the removal by electrolysis of some of the contaminants in the nitrobenzene[114,116]. The build-up in voltage has to be slow in order to minimize the effects of heating in the cell.

The voltage across the cell was held at a number of chosen values from $0 \rightarrow 22$ kV while shadow-graph photographs of the areas of maximum and minimum transmission were taken. The pictures thus obtained show the static field set up in the cell for any particular value of the applied voltage. The angle which the polarization of the incident light makes with the applied field does not affect the positions of the transmission maxima and minima on the voltage versus transmission curve. The result of rotating the direction of the applied field from the ideal angle of $\pi/4$ to the plane of polarization is a decrease in the absolute value of the maximum intensity of the transmitted light. At the ideal angle, the ordinary and extraordinary rays are of equal magnitude. Rotation of the field alters their comparative amplitudes, so that when the field is strong enough to produce a phase difference of π between the E- and O-rays, the amplitude of the resultant wave, resolved in the plane of polarization of the analyser, is reduced.

Fig.5.5 shows the structure of the field around the electrodes as shown by the Kerr effect. As the voltage is increased, the transmission of light first becomes visible in the areas where the light polarization is optimum, but with higher voltages, the dark fringes (areas where the phase difference is $0, 2\pi, 4\pi, \ldots$) can be seen to correspond to the electrostatic isodynes as plotted in Fig.5.2 for a line charge and an

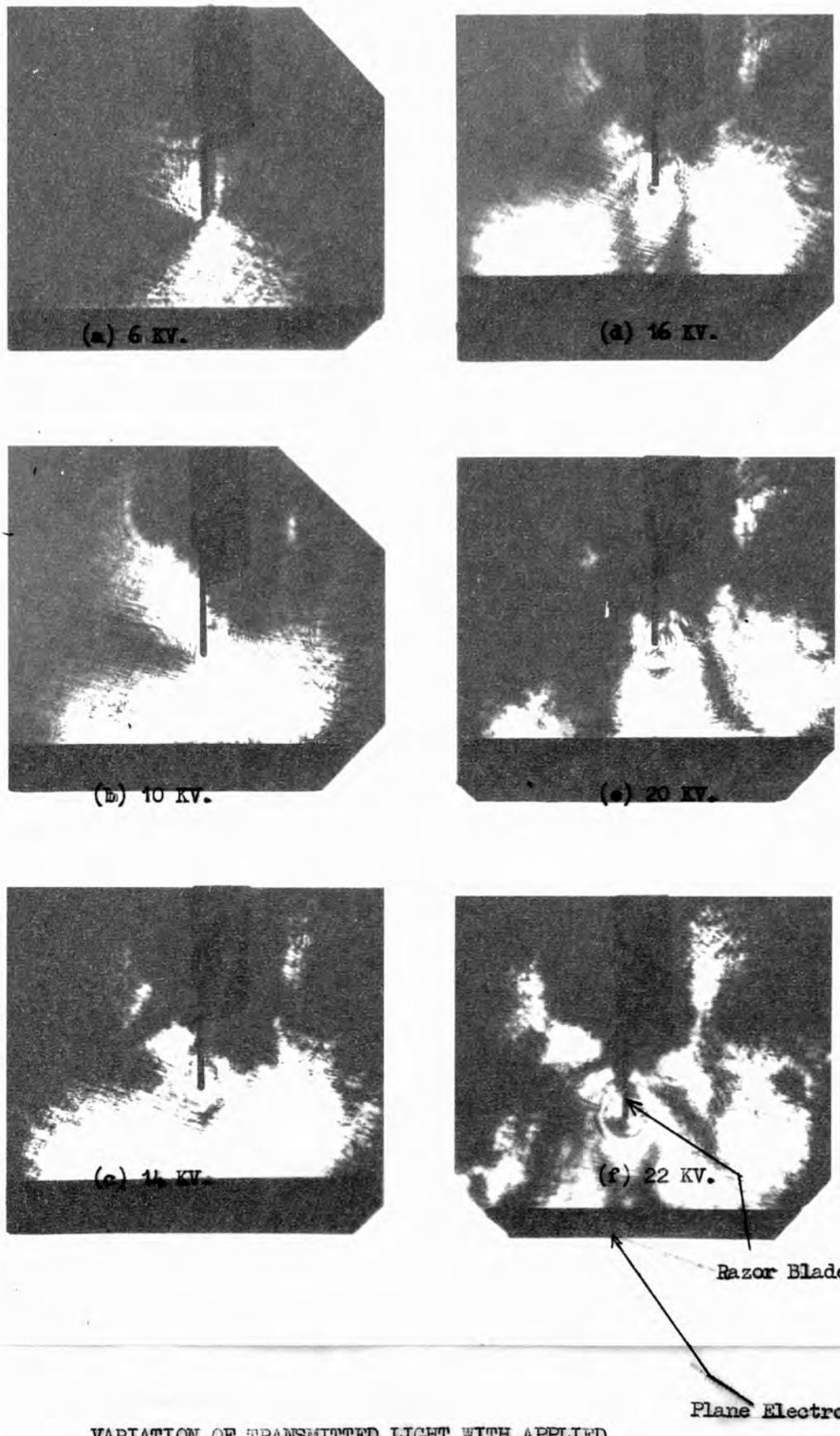

VARIATION OF TRANSMITTED LIGHT WITH APPLIED VOLTAGE ACROSS THE KNIFE-EDGED KERR CELL.

FIGURE 5-5.

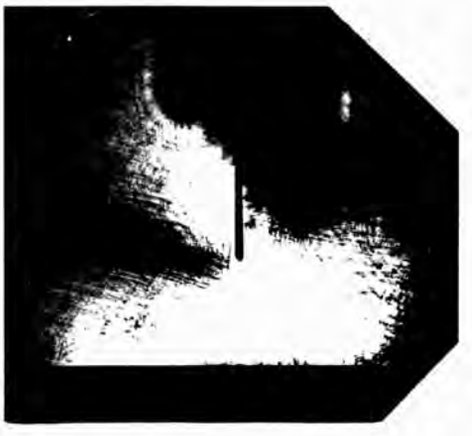

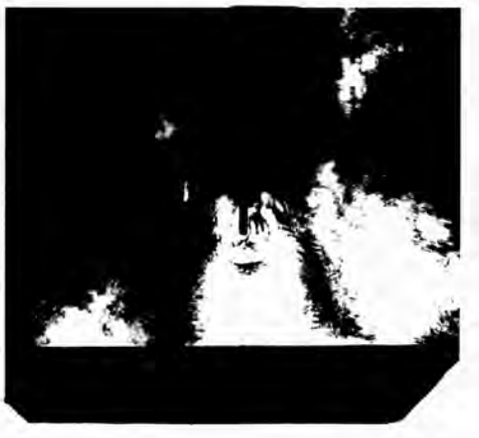

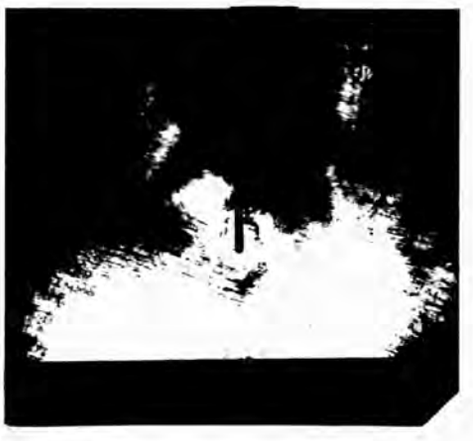

earthed plate. The correspondence of these photographs to the theoretically predicted isodynes is not completely accurate. The theoretical calculation is for an infinite line charge and an infinite plate. In the practical, observed case the razor blade does not approximate precisely to a line charge and the field is further distorted by the bulk of the mounting for the razor blade. Nevertheless, over the area in which we are interested – that is the fairly narrow area between blade and plate, ignoring the edge effects – the field is as expected. In the configuration where the electrodes take the form of cylinders, these approximations do not all apply. When a voltage of 22 kV is applied to the cell, a phase difference of up to 8π could be detected by counting across the contours of the E^2 isodynes. These very high fields induced a flow in the liquid which resulted in a distortion of the images of the electrodes. For this reason the silhouettes of the electrodes have been super-imposed on the photographs so that the electrode positions are clearly defined. The induced flow did not effect the stability of the isodynes. The use of a He-Ne laser as the illuminating source, resulted in the need for exposure of $\gg 1$ sec, and it can be seen that the positions of the isodynes must have been stable over that period of time. If the cell were to be used as a switching device, obviously a very much more powerful light source would be needed in order to permit photography with the device.

(ii) The optical switching properties of the cell were examined by putting a pulsed voltage across the cell. The circuit is shown in Fig.5.4. The voltage was applied by the rapid discharge of high voltage capacitors across the cell. The voltage at any time was measured through a potential divider and displayed on a Tektronix Type 454 oscilloscope. The rate of discharge was governed by the value of a second resistor in parallel with the cell. As the resistance was reduced, the rate of discharge increased. The system was switched by the spark-gap switch described

in Chapter III, consequently the voltage rise time was very fast whilst the period of the discharge could be varied from $\mu s \rightarrow ms$. As the spark-gap switch was triggered, the amount of radio noise created by the triggering system swamped any signal which was detected at that time, but the noise is short-lived, and the subsequent voltage and optical transmission changes could be displayed clearly.

During this part of the experiment, the He-Ne 2 milliwatt laser beam was used to probe a chosen area of the cell's cross-section. For this purpose the beam was not expanded and the chosen area was thus defined by the beam's width. A second advantage of using the unexpanded beam was the greater power per square centimetre cross-section available. The detection system - the PIN diode - was working at the limit of its sensitivity and so a maximum efficiency had to be obtained within the probed region of the cell. The photographs of the oscilloscope recordings are shown in Fig.5.6. As is shown, the cell voltage follows the expected exponential form as the capacitor discharges. The rate of switching is at its greatest when $d(V^2)/dt$ is greatest, i.e. not only when dV/dt is maximum but also the absolute value of V. These two maxima both coincide during the early part of the discharge. The extent of the switching modulation depends on the width of the probe beam, and if a broad beam is used the modulation decreases as a greater number of isodynes are crossed by the beam. From the photographs it can also be seen that as the speed of the discharge is increased, so also the contrast between the maximum and minimum transmission decreases. At the limit shown, the effect of the field produces less than a 10% modulation on the transmitted light. It was not possible to determine whether this is due to a distortion in the detected signal or whether it is a failure of the cell to operate correctly at this speed. Difficulty was experienced in producing these transmission curves due to the very low light levels involved, and the detector was working at the

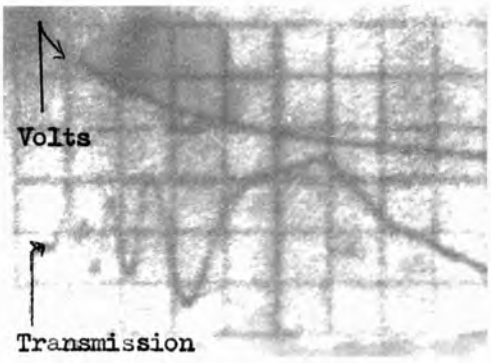

500 μsecs/div.

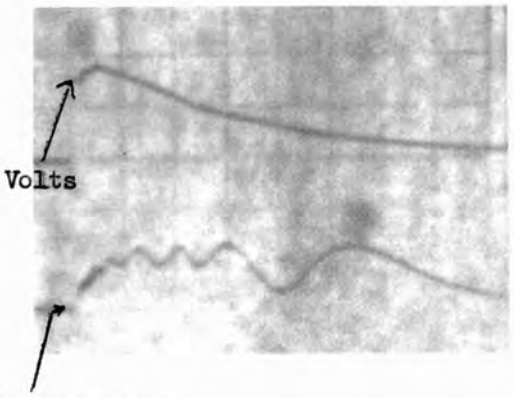

200 μsecs/div.

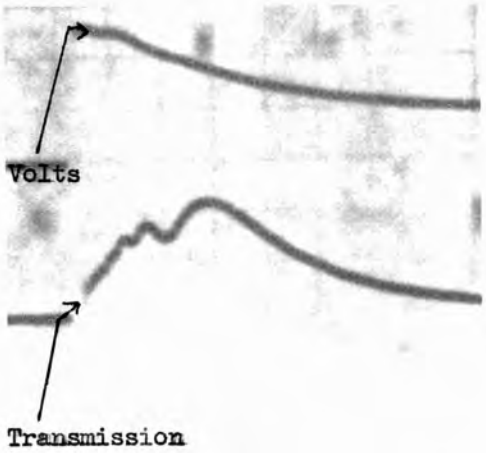

10 μsecs/div.

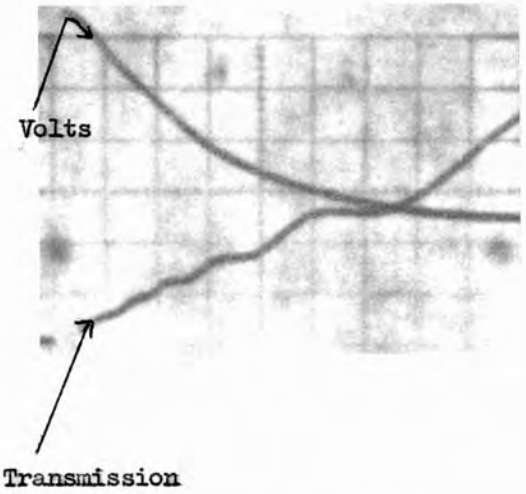

5 μsecs/div.

VOLTAGE AND OPTICAL TRANSMITTIVITY PLOTTED AGAINST TIME.
(KNIFE-EDGED KERR CELL.)

FIGURE 5-6.

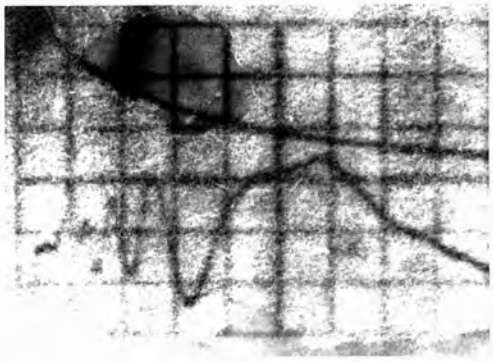

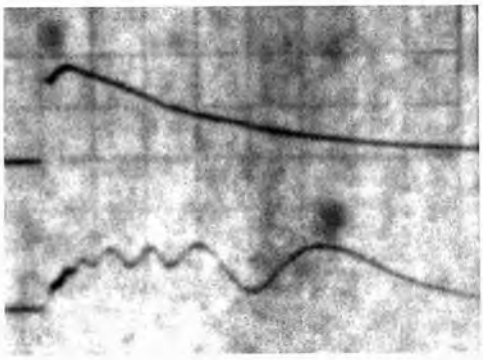

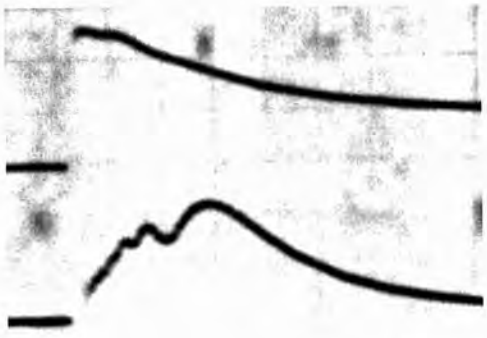

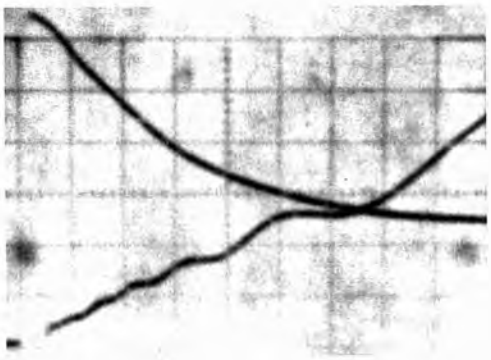

limit of its sensitivity, which may be the reason for the low percentage light modulation. On the other hand a second possible cause for the slow speed of the cell could be the presence of impurities in the nitrobenzene.

If a more powerful light source had been available at the time, the investigation of the very fast switching rates would have been greatly facilitated. However, the results do show that this principle has promise as a fast device utilizing the high fields and the reduction in capacitance which results from this geometry.

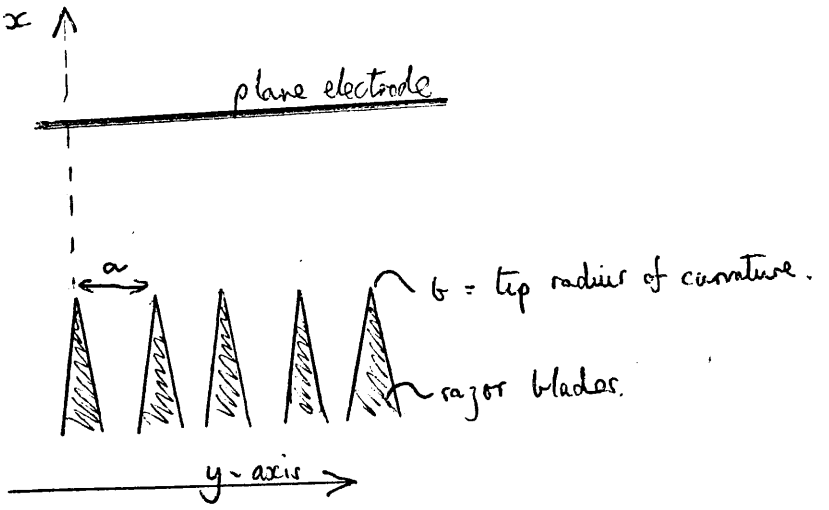
x
plane electrode
a
b = tip radius of curvature.
razor blades.
y - axis

CHAPTER VI

INVESTIGATION INTO THE ELECTROSTATIC FIELD NEAR A RAZOR BLADE STACK ELECTRODE

6.1 INTRODUCTION

In this chapter we look in more detail at the electrostatic field configuration set up between a plane conductor and the edges of a stack of razor blades. The razor blades are stacked so that the blade locating holes are collinear, and so that the edges of the blades all lie in a plane which is parallel to the plane conductor and separated from it by a distance of 7 mm. The separation of adjacent blade edges is 0.1 mm.

A probing light beam is directed across the stack so that it passes through spatially periodic regions of high and low field intensities when a potential difference is maintained between the electrodes. The theory consists of an extension of the isodyne computation from section 5.4. The field at a point due to a wire and a plane electrode has been given:

$$E = \frac{2\sigma d}{\epsilon}\left[(x^2+y^2)\left\{y^2+(x-d)^2\right\}\right]^{-\frac{1}{2}} \text{ esu .} \qquad \ldots (6.1.1)$$

It has been shown in Chapter V that this equation is approximately true in the region between the electrodes, but that the distortion caused by the electrode mounting cannot be described by the equation.

In this case the electrode consists of a stack of 1,200 razor blades side by side. The very close proximity of neighbouring blades further reduces the area of non-uniform field. The useful region of the cell is such that $x < a$ where a is the thickness of one razor blade.* The field is at a maximum when $x = b$ and $y = 0, a, 2a, 3a, \ldots$ when the x-axis is defined as the perpendicular from the end razor blade to the face of the plane electrode, and b is the tip radius of curvature.

* see diagram opposite

6.2 POSSIBLE MECHANISMS AT WORK IN THE CELL

6.2.1 Thermal Effects

The thermal effects in the cell are directly related to its resistance. As every effort was made to increase the cell's resistance these effects should be at a minimum. Nevertheless, at the tips of the razor blades the leakage current across the cell is channelled through the regions of strongest field. The obvious result of the high current concentration is the heating of the liquid at the razor blade tips, and an array of high and low temperature lines will be set up by the field. The resulting expansion of the liquid along the tips leads to lines of low density. If the field were to be held on the array for any length of time a convection current would be set up. This current can be minimised if the blades are positioned above the plate so that the low density regions will already be at the top of the cell.* The relaxation time for a thermal grating when it is optically induced is $\sim 10^{-7} - 10^{-8}$ secs.[117]. This is many orders of magnitude faster than the fields applied to the cell in this investigation, and so would not limit the speed at which the cell switches in this case. Other thermal effects, such as a variation in the ambient temperature are far too slow to be worth considering here. We should note, however, that some of the other mechanisms which we are considering, (e.g. Kerr effect), are temperature dependent.

6.2.2 Electro-striction

The electrostrictive forces in the liquid can be calculated from the field and the dielectric constant of the material.

For the two liquids under consideration, the dielectric constant K_e is ~ 81 for water and ~ 37 for nitrobenzene. These are the static values. At optical frequencies K_e for water falls to 1.8. The large static value is due to the reorientation of a permanent dipole moment in water, but the rotational inertia is too great to follow the optical

* NB opposite way up to Fig. 61.

response. What is required for a fast response, is the presence of an induced electronic dipole moment in the liquid. The excess pressure in a parallel plate condenser due to the applied electric field is $p - p_o$, where

$$p - p_o = \epsilon_o \frac{(K_e - 1)E^2}{2} \quad . \qquad \ldots (6.2.1)$$

(Symbols are explained in App.II.) This is calculated from the force experienced by the dipoles in the non-uniform field at the edge of the capacitor. The force on the dipole is :

$$F = (P \cdot \nabla)\underline{E} \quad , \qquad \ldots (6.2.2)$$

where P is the dipole moment of the liquid.

In this case $K_e \gg 1$, therefore

$$p - p_o = dp \simeq \epsilon_o \frac{K_e E^2}{2} = \frac{K_e E^2}{8\pi} \quad . \qquad \ldots (6.2.3)$$

Compressibility of the liquid

$$C = \frac{1}{V} \cdot \frac{dV}{dp} \qquad \frac{dV}{V} = C\,dp \, , \qquad \ldots (6.2.4)$$

$C = 5 \times 10^{-4}$ bar^{-1} for water. Therefore

$$\frac{n - n_o}{n_o} = \frac{dV}{V} = Cdp = \frac{K_e E^2}{8\pi} \times 5 10^{-4} = \frac{\Delta n_a}{n_{ao}} \quad . \qquad \ldots (6.2.5)$$

This shows the relationship between the incremental change in refractive index and the value of the field. This is an E^2 dependent effect and therefore any modulation of the probe beam due to this effect will be at twice the frequency of the applied field. This is a fast effect, relaxation times $\sim 10^{-9} - 10^{-10}$ secs are recorded for optically induced electrostriction.

6.2.3 Kerr Effect

The Kerr effect has already been generally covered in section 5.2. It too has an E^2 dependency. As the polarization of the incident light is important in this case, its effect is minimised by making the polarization of the incident light either parallel to perpendicular to the faces

of the electrodes. The Kerr effect is the most rapid of the effects considered here, as it is the result (in nitrobenzene which has a high Kerr constant) not of molecular reorientation but of electron cloud distortion effects. The relaxation time in this case is $\sim 10^{-11}$ to 10^{-12} seconds. In water, on the other hand, the Kerr effect can be ignored as this liquid has a very much lower Kerr constant.

6.2.4 Slower Effects

Under this heading come effects with relaxation times several orders of magnitude greater than in the previous section. Convection currents due to heating by the electric field have been referred to in section 6.2.1. These can cause a gross distortion of the beam and lead to defocusing. The relaxation time for this effect can be of the order of several seconds. A second slow effect is produced by the presence of air bubbles in the cell. Like the convection currents, this effect also incorporates the bulk transport of liquid, and this is the reason for the slow relaxation times. The liquid acts as though there are regions of abnormally high compressibility at the points occupied by the bubbles. This is due to the distortion of the bubble. If the bubbles collect along the tips of the razor blades in the stack, the maximum deformation takes place nearest the tip. At the liquid/air interface there is a high change of refractive index, so that any alteration to this geometry effects the direction of the probing light beam. Electrostrictive distortion of these bubbles would bend the beam in the following manner. In the absence of an electric field, approximately spherical bubbles collect along the tips of the blades. When the electric field is applied, the greatest field is at the tips, and the fall-off is higher (see Fig.6.1(a)) in the x-direction than in the z-direction. The bubble will thus experience a stronger force in this direction and will be distorted, Fig.6.1(b) and (c), to an elongated shape. This produces a change in position of the liquid/air interface with the result that the probe is deflected up towards the razor blades.

(a) Electrostatic Isodynes near a Razor Blade Stack Electrode.

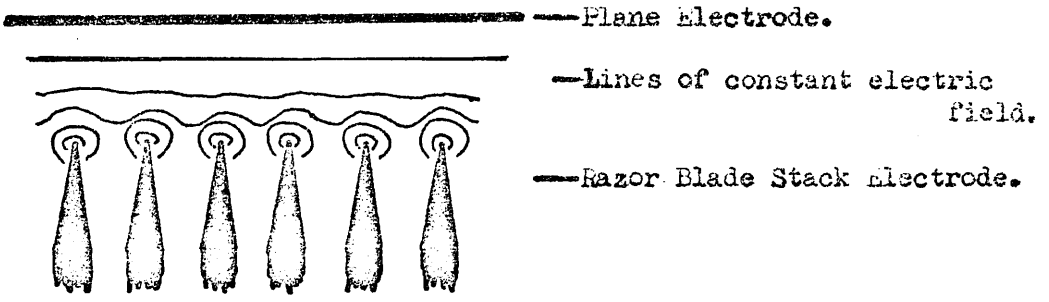

(b) Air Bubbles at the Razors' Tips.

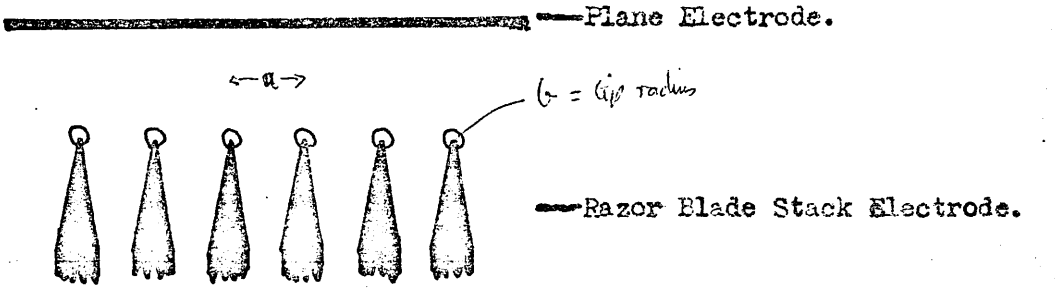

(c) Bubble Distortion by an applied field.

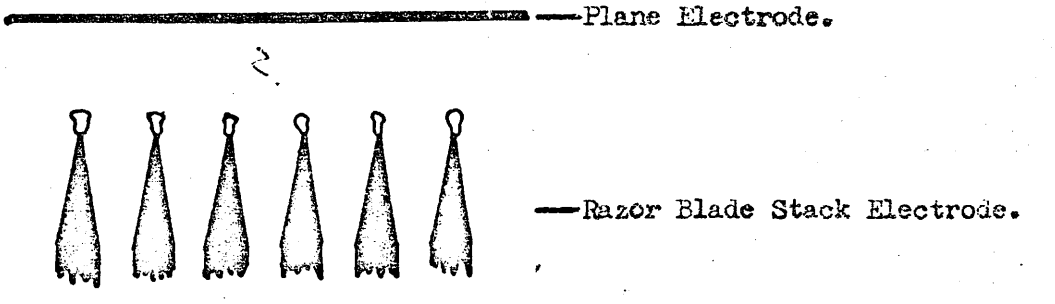

HIGHLY NON-UNIFORM ELECTRIC FIELD, RAZOR BLADE STACK.

FIGURE 6-1.

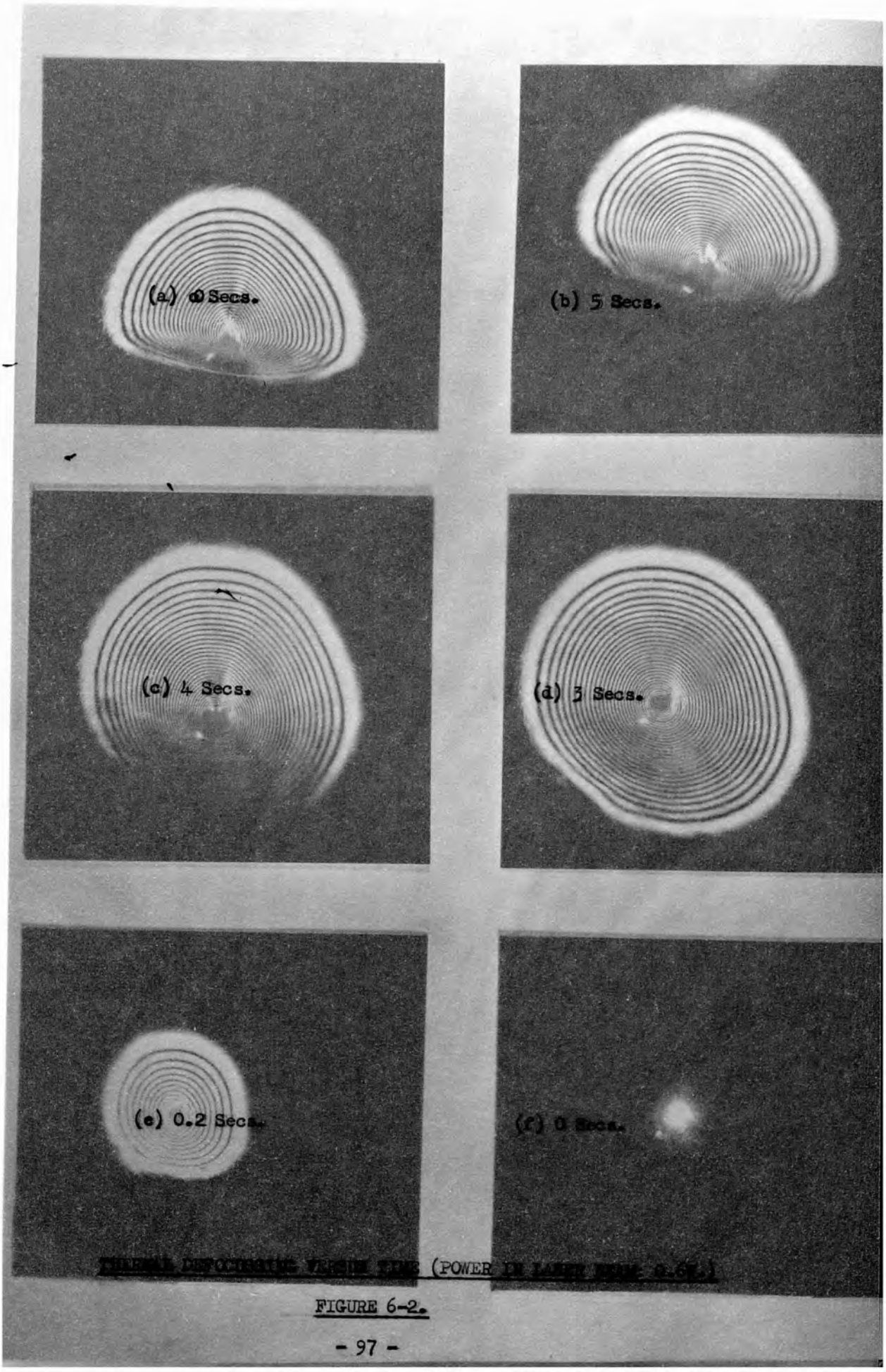

THERMAL DEFOCUSING VERSUS TIME (POWER IN LASER BEAM 0.6 W.)

FIGURE 6-2.

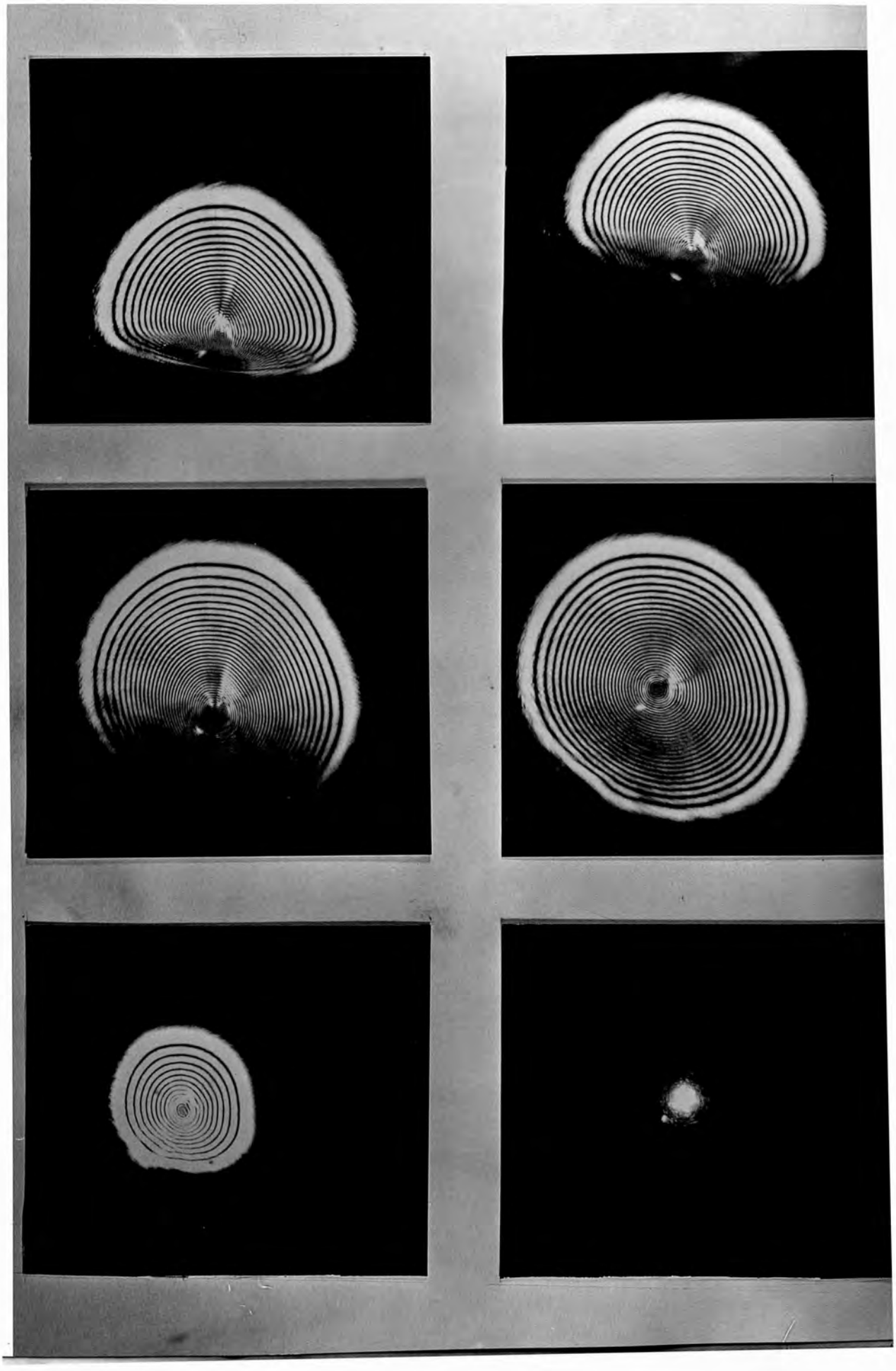

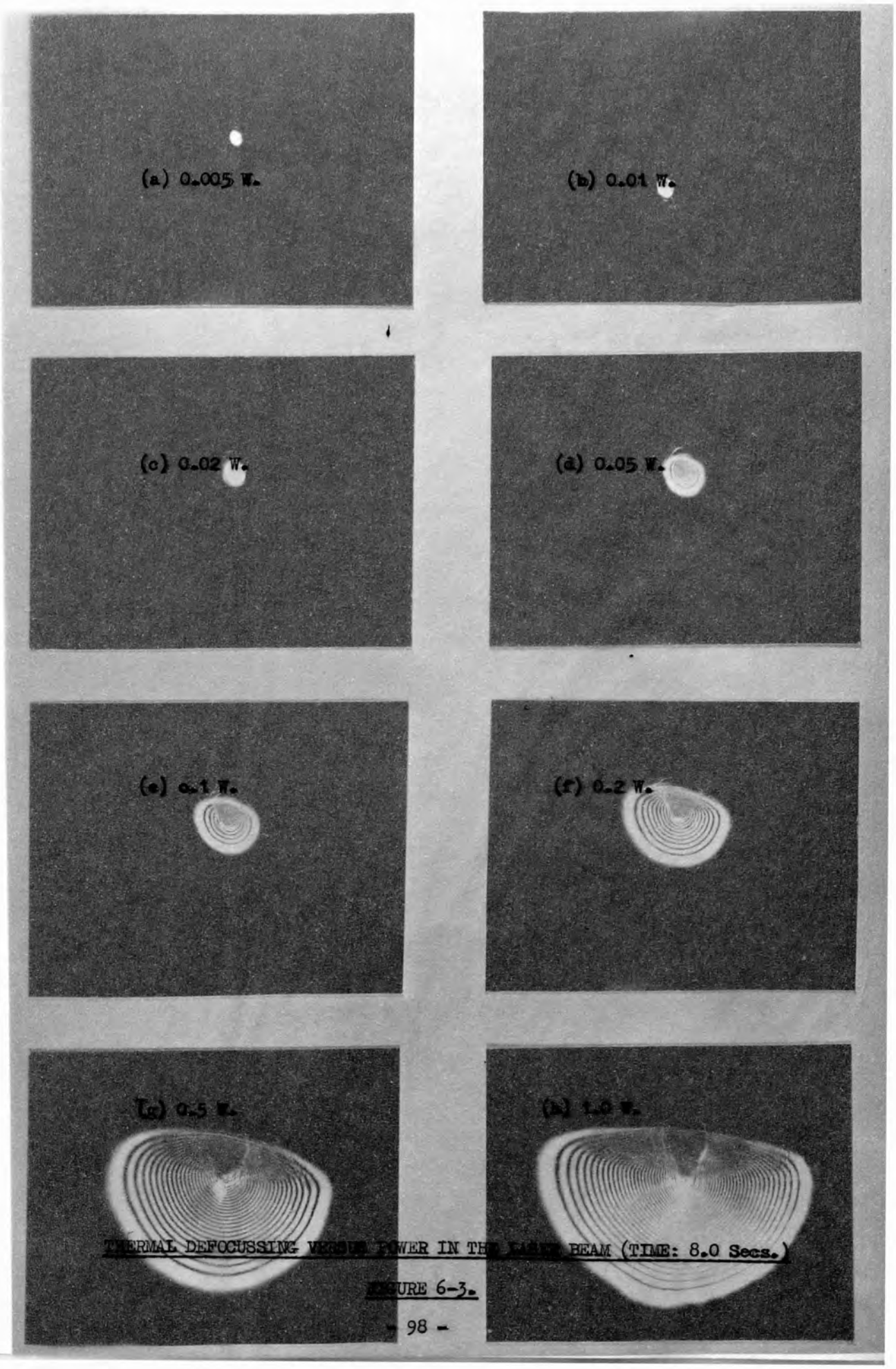

THERMAL DEFOCUSSING VERSUS POWER IN THE LASER BEAM (TIME: 8.0 Secs.)

FIGURE 6-3.

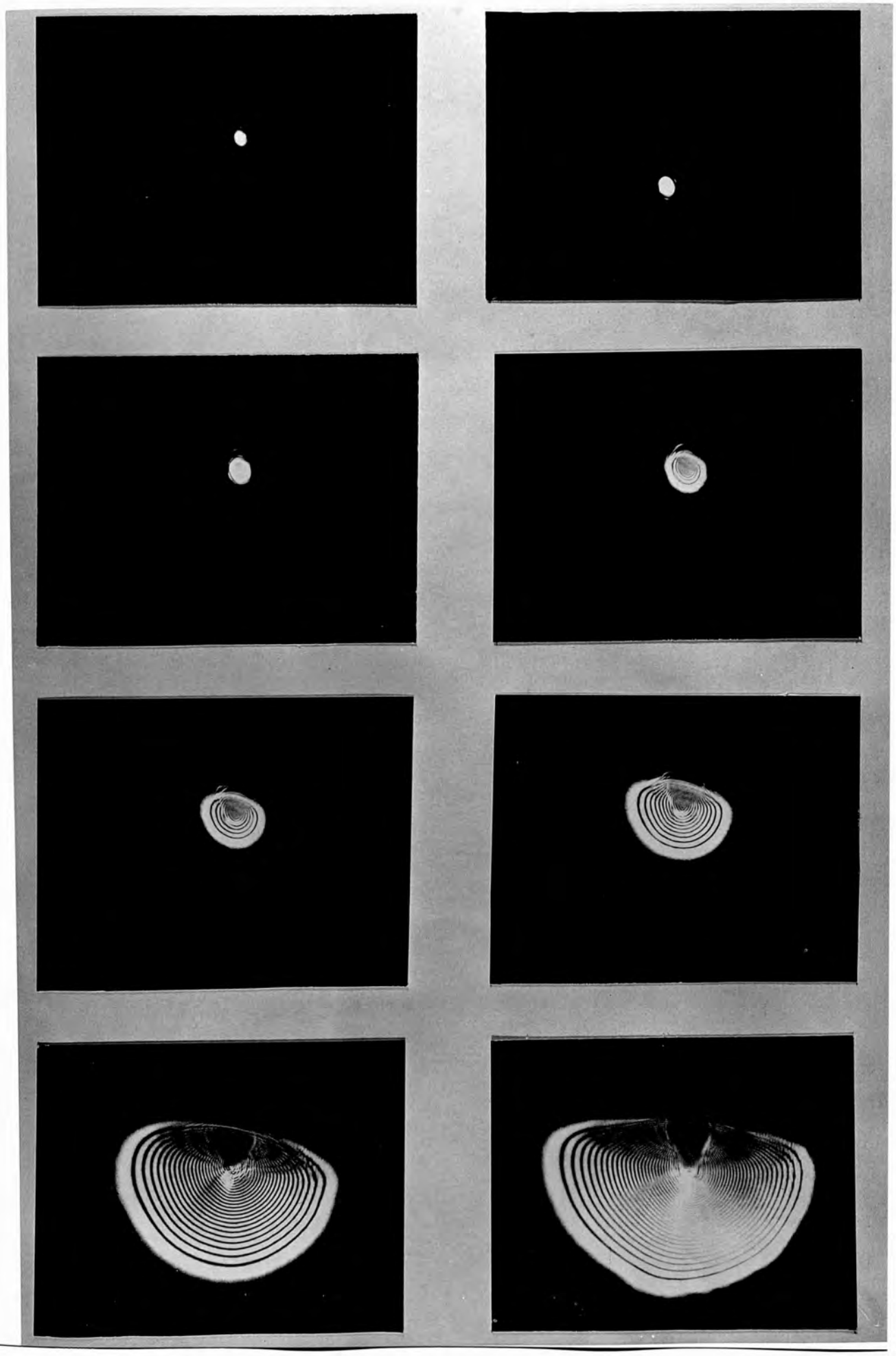

6.2.5 Thermal Defocusing

This is another slow effect. Thermal defocusing is dependent on the rate of absorption of energy from the probe beam, and thus is increased when a longer cell is used. The heating of the beam produces a region with a radial refractive index gradient in the beam cross section. The beam is deflected away from the axis and produces a series of interference rings around the original axis[118,119]. The effect builds to a maximum in four to five seconds, after which a convection equilibrium is established. Cool liquid is drawn in from beneath a horizontal beam. The liquid heated by the beam leaves from the top. When the equilibrium is established, the maximum angle of the defocusing can be related to the incident beam power. The interference rings distort because the refractive index gradient is no longer symmetrical about the axis. In nitrobenzene which has a coefficient of absorption (at 514.5 nm) of $\sim 0.05\ cm^{-1}$ the effect is readily observed and can only be minimized by reducing the beam power to $\sim$ mW. In water, however, the coefficient of absorption at 514-5 nm is approximately zero, and so very much greater power may be used without exhibiting this effect. The build up of this effect is shown in Figs.6.2 and 6.3 for different values of power in the argon laser beam passing through nitrobenzene.

6.3 INTERACTION OF ARGON LASER PROBE BEAM WITH PHASE GRATING

For constructive interference by Bragg reflection:

$$2D\cos\theta = \frac{m\lambda}{n_o} \quad \text{(Bragg equation)} \quad .. \quad (6.3.1)$$

In the case of the razor blade stack, the reflection takes place at a maximum where there is a maximum rate of change of refractive index. Unfortunately the rate of change of refractive index depends not only on the distance across the induced phase grating, but also there is a dependence on the distance from the tips of the razor blades. Near the tip of each razor blade, the electric field is at a maximum. A probe beam which

is directed across the tips of the blades in the razor stack, would pass through a region of rapidly increasing refractive index followed almost immediately by a similar region of rapidly decreasing refractive index. This would happen as each razor blade tip is passed. The grating spacing, however, is determined by the distance between adjacent blade tips. The result of the double change in refractive index at each blade, is a double grating. The first grating corresponds to regions of rapidly increasing refractive index, and the second grating corresponds to regions of rapidly decreasing refractive index. On reflection from the second grating, the light undergoes a phase change. The relative positions of the two gratings varies across the gap between the two electrodes, so that different parts of a probe beam would see the two gratings with different spatial separations.

In the case of the experimental razor blade stack, $D = 10^{-1}$ mm. If the wavelength of the incident light is 600 nm then the first order of maximum Bragg reflection occurs at an angle of incidence $\theta_o = 89^\circ\ 52'$ (1.568 radians).

As the length of each razor blade in the stack is only 3.6 cm such an angle of incidence would not be possible if the beam is to cross more than one plane of high refractive index. Even with an angle of incidence $\theta_o = 74^\circ$ a maximum of about fifty planes would be traversed. This angle corresponds to $\sim 120^{th}$ Bragg maximum.

As the angle for successive Bragg maxima has a cosine dependency, the angular spacing between adjacent maxima increases for small θ_o. When θ_o is $\sim 7^\circ\ 3'$ the Bragg order is 440. The angular separation of adjacent orders is $\sim 58'$ at this angle compared to $\sim 10'$ for lower orders. The complete interaction region (all 1,200 razor blades) is only full used when $\theta < 11^\circ\ 30'$.

Bragg reflection is a multiple beam interference effect, the spacing of the grating thus plays a very important role, and any irregularities in this spacing would have a large result on the possibilities of detecting Bragg reflected light. It is on this criterion that the razor blade stack failed as it was not possible to produce a regular spacing to within a fraction of a light wavelength accuracy.

If the required regularity in spacing were to be obtainable, the angular width of each maximum would be of the order of a few seconds of arc, which would lead to a very small intensity in the reflected light.

However, as the Bragg conditions could not be adequately fulfilled, the backscattered light would have a fairly uniform dispersion. An increase in the backscattered light should be detectable when the field is applied across the razor blade stack cell.

In the case of diffraction, the limiting criteria are not as stringent as those for Bragg reflection. Some diffraction of the transmitted part of the probe beam should be produced by the induced structure in the liquid in the cell. Any such coarse diffraction should be observable as more light is deviated in the forward direction than can possibly be backscattered from the grating. This diffraction of the transmitted beam should produce a large number of closely spaced orders.

6.4 EXPERIMENTAL SYSTEM

The design of the cell containing the razor blade stack was based on knowledge gained from the non-uniform Kerr cell. A photograph of the experimental cell is shown in Fig.6.4(a). The body of the cell was made from PTFE and the end windows were sealed with PTFE O-rings.

The cell was built in order to study both Bragg angle reflection and diffraction from the induced field structure in the liquid. The cell could be filled either with nitrobenzene or de-ionized water. In order to avoid contamination of the liquid, the electrodes and mountings were made from stainless steel which had been electro-polished to provide clean rustless surfaces. As the figure shows both electrodes were mounted on to the same end of the cell so as to afford greater ease of access.

Bragg reflection studies required the elimination of strong reflecting surfaces and a wide angular aperture. For these reasons the front window of the cell covered the whole cross section and was offset as approximately the Brewster angle.

The cell was mounted so as to facilitate adjustment along all three orthogonal spatial axes as well as rotational adjustments around the two axes perpendicular to the direction of the probing light beam (Fig.6.4(a)).

The electrodes were mounted with the razor stack uppermost in order to minimize any convection currents caused by heating along the tips of the razor blades.

For the greater part of the experiment, the cell was filled with de-ionized water. The water was circulated around a system designed to remove any air in the cell and to deionize the water. A peristatic pump was used so that the minimum number of contaminating surfaces was brought into contact with the liquid. As Fig.6.6 shows, the water was circulated through a reflux system so that the air was driven out of solution, and then passed through a cooling condenser before entering the permutit de-ionizer. It was then recirculated through the cell containing the razor blades.

An argon ion laser (by Coherent Radiation Laboratories) capable of producing a maximum of one watt output in the 514.5nm green line was

(a) Razor Blade Stack Cell.

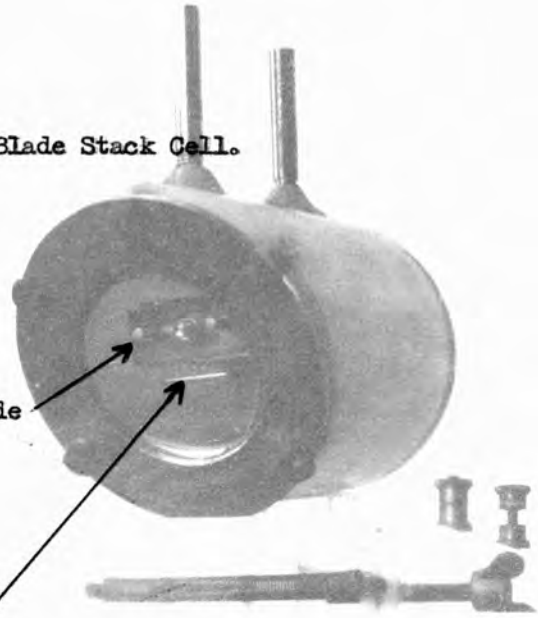

(b) Modulation of Diffracted Light.

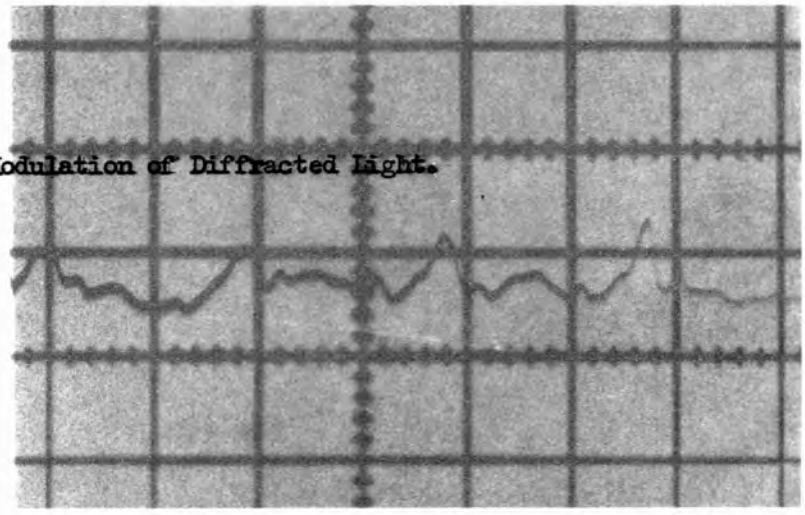

5 μ secs. per division

THE RAZOR BLADE STACK CELL.

FIGURE 6-4.

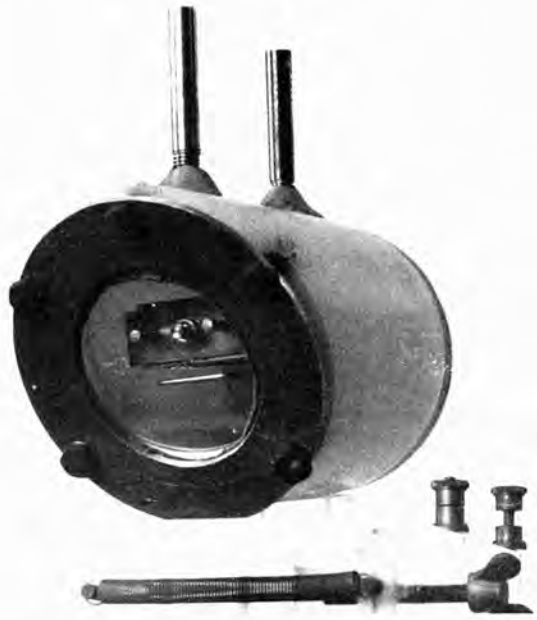

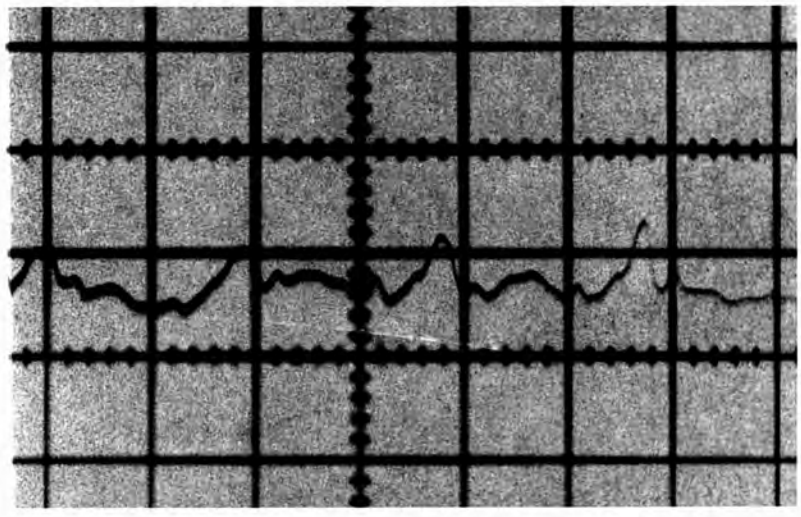

used as a probe. This power is great enough to produce a large thermal defocusing effect in nitrobenzene[118]. The maximum power in the light beam was kept to 0.5W so that the thermal defocusing effects in water could be ignored. It was necessary to keep the cross-section of the probe beam to a minimum so that the maximum power could be passed through the region of highest field variation near the tips of the blades without much light being scattered off the adjacent edges.

The electrode separation was 5.0mm, The system for applying a field in the cell was kept as simple as possible. A mains frequency transformer supplying 7.0kV across the cell was wired directly to the electrodes. This made for simplicity in detecting any effects produced by the field. A PIN photodiode was used in conjunction with a Tektronix 551 oscilloscope to detect the diffracted light.

6.5 INVESTIGATIONS INTO THE EFFECT OF THE FIELD STRUCTURE

The investigations were divided into two main parts:

(i) Study of light reflected back from the structure.

(ii) Observations on the effect of the electric field on transmitted light.

(i) The cell was filled with nitrobenzene. An electro-photonics dye laser, producing 20kWs at 590nm, was used to probe the interaction region (Fig.6.5). The beam of light was directed across the tips of the razor blades at an angle almost perpendicular to the high field lines. The laser output varied widely from shot-to-shot, so a correlation was sought between the intensity of the incident light pulse, and that of the corresponding back-reflected pulse. The incident beam was slightly divergent so that more than one Bragg maximum was included in the angle of divergence. For the angle of incidence used (~140 mrads) the angular separation of the Bragg maxima is ~17mrads, and the angular width at half reflectivity was ~0.13mrads thus with 100% reflectivity

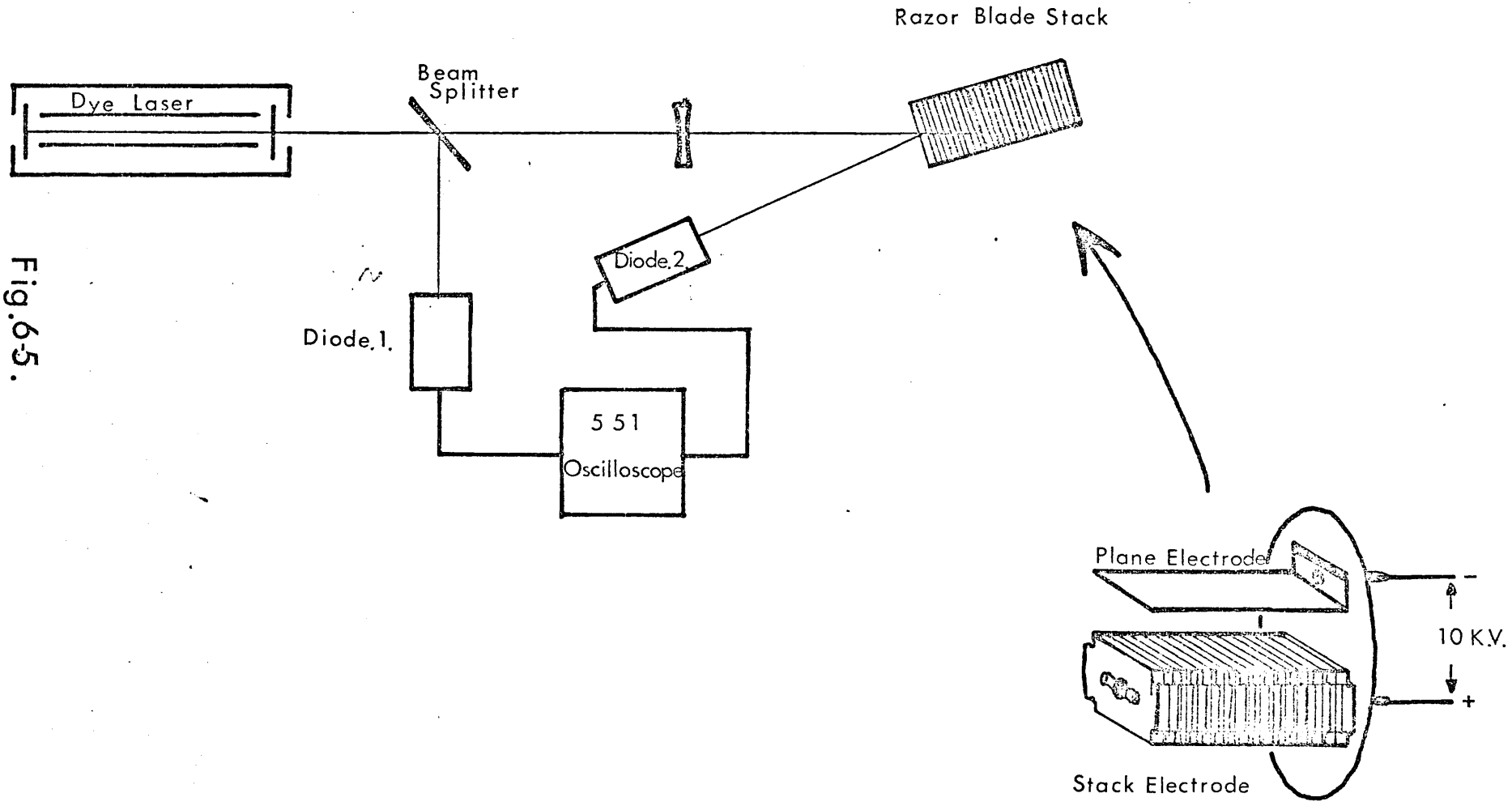
Razor Blade Stack
Beam Splitter
Dye Laser
Diode.2
Diode.1.
5 5 1
Oscilloscope
Plane Electrode
10 K.V.
Stack Electrode

Fig.6-5.

0.76% of the incident beam would be reflected. The back scattered light was focused on to a photodetector by a second cylindrical lens. There was some slight evidence for an increase in the back-scattered light when a voltage of 7kV was applied to the nitrobenzene filled cell, but this could not be validated statistically. There was a mean increase of 9% in the intensity of the back-scattered light when the electric field was applied. However, over the range of measurements taken, there was a very wide range in this intensity. This was due in some measure to the direction of the incident beam varying from shot to shot. These problems could be avoided by using a continuous probe system with a modulated voltage supplied across the cell.

(ii) Observations on the transmitted light. The cell was set up as in Fig.6.6. The probe beam was the 514.5nm argon line. The intensity of the incident light was held constant and a changing field was applied to the cell. When the argon laser was used to probe the cell, a limitation on the incident power had to be imposed because of thermal defocusing.

The narrow aperture between the electrodes led to a distortion from the normal ring fringe structure produced by this effect.

In nitrobenzene the thermal defocusing led to an extremely strict limitation on the beam energy used. This was mainly due to the length of the cell (12 cms). Because of this restriction, nitrobenzene was not used in the cell during the diffraction observations as these required a high energy in order to produce enough diffracted light for any measurements. When a pulsed laser is used this power restriction does not apply.

For water, the absorption of the argon laser light is low enough for there to be no appreciable defocusing, even at powers of 0.5W. Thus, deionized water rather than nitrobenzene was used for the experiments in which high power was needed from the argon beam.

FIGURE 6-6

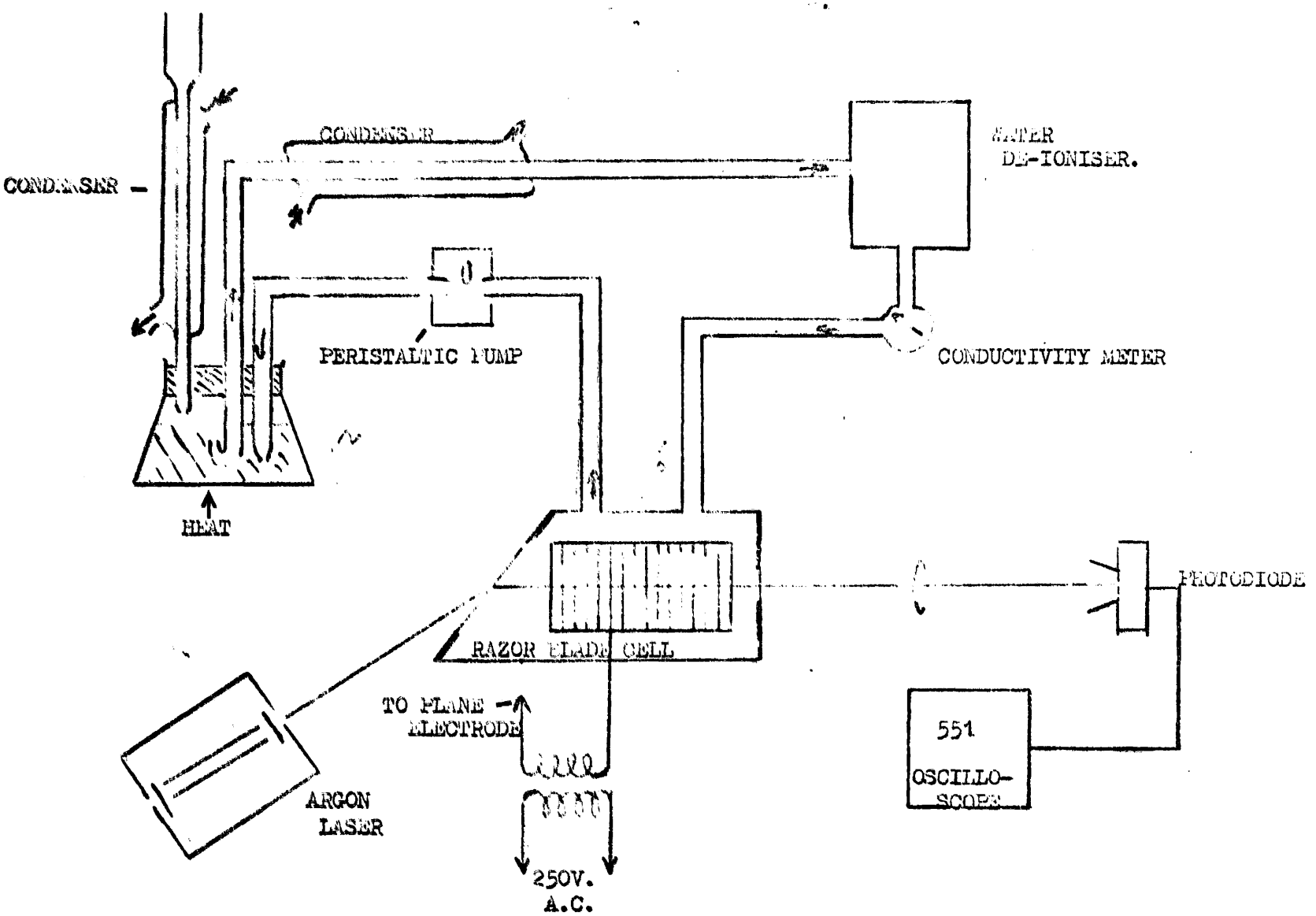
CONDENSER
CONDENSER
WATER
DE-IONISER.
PERISTALTIC PUMP
CONDUCTIVITY METER
HEAT
PHOTODIODE
RAZOR BLADE CELL
TO FLAME
ELECTRODE
ARGON
LASER
551
OSCILLO-
SCOPE
250V.
A.C.

It was found that even without the application of an electric field, there was enough scattered light diffracted from the tips of the razor blades, for a signal to be registered by the photodetector which was monitoring the diffracted light. When the 3,500 V, 50 Hz potential difference was applied to the cell, there was an increase in the diffracted light intensity accompanied by a modulation at 100 Hz . Fig.6.4(b) shows this intensity modulation.

In the diffraction pattern produced from the stack of razor blades, the individual lines are so closely spaced as to merge into an almost continuous band. As the field was held on the cell for some seconds, thermal convection currents produced some distortion of this diffraction pattern.

6.5.1 Beam Deflection

On the application of an electric field, considerable beam deviation was observed ($\sim$ 10 mrads) in the direction towards the razor blades. As the field was held on, the beam remained steady and did not oscillate at the 50 Hz of the voltage applied to the cell. On removal of the field, considerable distortion of the beam took place. This was produced by the convection current which had been hindered by the electro-strictive effects during the period of the field's application. The beam deviation was produced solely by electro-strictive distortion of the air-bubbles. Any thermal effects would tend to bend the beam in the opposite direction, as the temperature is at a maximum on the blade tips. When the air-bubbles were removed from the system, some slight beam deflection might still be expected from the electrostriction within the liquid. The electrostrictive forces in this case would produce an array of cylindrical lenses each contributing towards the deviation, and thus the maximum deviation is again produced near the blade tips. When removal of the air-bubbles from the

cell was achieved by boiling the circulating water, the remaining deflection effect was not great enough to be observed. On application of the field, the air bubbles in the cell were seen to distort and 'stand away' from the edges of the blades. The rise time for the phenomenon was $\sim 10^{-1}$ secs as there was a bulk transport of liquid involved in this process.

The reason why beam deviation due to the electro-strictive forces within the cell in the absence of any air bubbles could not be observed, is clear from section 6.1. The regions of very high field were restricted to areas where $x \sim b$, so the only part of the beam likely to be deflected is the part less than 0.01 mm from the surface of the stack. In this case the beam is pulled on to the electrode and reflected from the tips to produce an increase in the amount of light in the diffraction pattern. If beam deviation were to be looked for, the razor stack would need to be modified so that its surface has a convex cylindrical curvature and the deflected beam follows the main contours of the surface, passing through all the regions of maximum field.

The beam deflection was found to be independent of the polarization of the probe beam, however it was found that there was a polarization dependency of the diffracted light. The diffraction was at a maximum when the electric vector was parallel to the tips of the razor blades.

The investigations show that the razor blade stack electrode geometry has potential as a fast switching device because of the relatively low voltages required to produce the high fields at the blade tips. Some further work could be done looking for the effects of beam deviation produced by a modified stack so that the electrostrictive effects could be fully studied. A defect of the present system lay in the lack of precision in the spacing of the blade edges. This would particularly effect the efficiency of Bragg reflection, but would not greatly perturb the coarse diffraction properties.

CHAPTER VII

DIRECT PRODUCTION AND OBSERVATION OF SHOCK WAVES BY A Q-SWITCHED RUBY LASER

7.1 OUTLINE OF THE TECHNIQUE USED

We have seen already in Chapter II the mechanisms whereby shock waves can be generated in liquids by a ruby laser. Such generation can often be the bi-product from the interaction when another effect is being studied, and as such is liable to pass unnoticed or to be ignored. In view of the general destructiveness of shock waves it is an advantage to observe the dynamic situation rather than just to examine the final results.

Laser induced shock waves can be generated either by the absorption of light by a suitable particle or surface, or by the breakdown of the liquid itself when the laser beam is focused. When the beam is focused down, the very high electric field in the focal region produces a stimulated Brillouin effect in the liquid[120,121], and thus gives rise to a spatially modulated refractive index structure in the form of a phase grating. From the structure some of the incoming radiation can be reflected back into the laser with a frequency shift. This difficulty, which is inherent when high powered lasers are focused into liquids, can cause damage within the active medium of the laser. A more detailed account of the stimulated Brillouin scattered process is given in Appendix I.

The photographic technique adopted in this work involved the frequency doubling of part of the ruby beam and the introduction of a delay path into this beam[28,122] so that the fundamental and second harmonic are finally combined in the interaction cell with a delay of 50→100 ns. The second harmonic wave was used as the photographic flash, and the fundamental beam was used to produce the shock waves. The use of a variable delay path in the second harmonic could enable a series of pictures to be

built up showing the movement of the shock waves. This was possible because of the high repeatability of the experiment. The strength of the shock waves produced by the laser varied negligibly from shot-to-shot.

7.2 EXPERIMENTAL DETAILS

The experimental arrangement can be seen in Figs.7.1 and 7.2. In Fig.7.1, the light source was a Bradley 351 ruby laser which was passively Q-switched by a cryptocyanine in methanol solution dye cell. This produced a giant pulse at 694.3 nm wavelength with a power of ~80 MW for 20 - 30 ns.

The pulse of light from the laser was first passed through a beam splitter which divided the beam into two, so that 75% was directed through a potassium dihydrogen phosphate (KDP) crystal. The remaining 25% was made to converge through a 5 cm cube water-filled cell, the focal point lying beyond the cell. The beam was given a 12 foot path delay before reaching the cell, so that there was a delay time of 24ns before the leading edge of the back-scattered pulse re-entered the laser. By this time the high power of the output pulse was thought no longer to be in the laser. The back-scattered pulse from the cell was caused by the partial focusing of the incident ruby laser beam producing a stimulated Brillouin scattering effect. This is the electrostrictive action whereby the high optical fields produced in the liquid give rise to a forward-going hypersonic wave, and a backward-going frequency shifted optical wave. The delay in the return path of the beam to the laser was meant to ensure that the mechanical stress induced in the laser rod by non-linear optical interactions between the two intense optical waves of different frequency, would be minimized. The returning light again passed through the beam splitter and thus suffered a second decrease in intensity. Consequently, a maximum of 6.25% of the out-going beam could be returned in this way. Damage to the ruby should not have taken place. Unhappily this was found not to be the

case, and there was eventually a mechanical failure in the crystal which curtailed further experiments. The damage, however, may equally well have been the result of pumping the ruby too hard.

The 25% portion of the laser pulse was monitored by a photodiode in conjunction with a Tektronix 454 oscilloscope and a 549 storage oscilloscope. The latter was used as an easy method of monitoring the pulses while the laser was being aligned. It was set at a slow scanning speed and registered each laser pulse so that the strength of the cryptocyanine dye solution could be adjusted until only one single Q-switched pulse was produced at one firing. The 454 oscilloscope was set at 50 ns per cm tracing rate so that individual pulses could be monitored, but a train of Q-switched pulses would not be detected.

In the water-filled cell, the laser beam interaction was observed by means of the 75% portion of the light pulse which passed straighat through the beam splitter (A) and was frequency doubled in the KDP crystal. The KDP crystal had been cut so that phase-matching between the fundamental and second harmonic beams took place when the fundamental was incident normally onto the front face of the crystal. The alignment was easily made with a He-Ne laser beam directed through the system and reflected from this surface. The second harmonic light which was in the near ultraviolet range, was observed by projection on to a fluorescent screen. Final adjustments to the position of the crystal were made so that the maximum second harmonic light was detected. At this point the efficiency of conversion was $\sim 25\%$.

This beam was cylindrically asymmetric so a correcting lens was positioned beyond the frequency doubling crystal in order to collimate the beam. The beam was sent around an 86 foot delay path (Fig.7.1) before being directed into the interaction cell where it was used to photograph the effect of the fundamental beam.

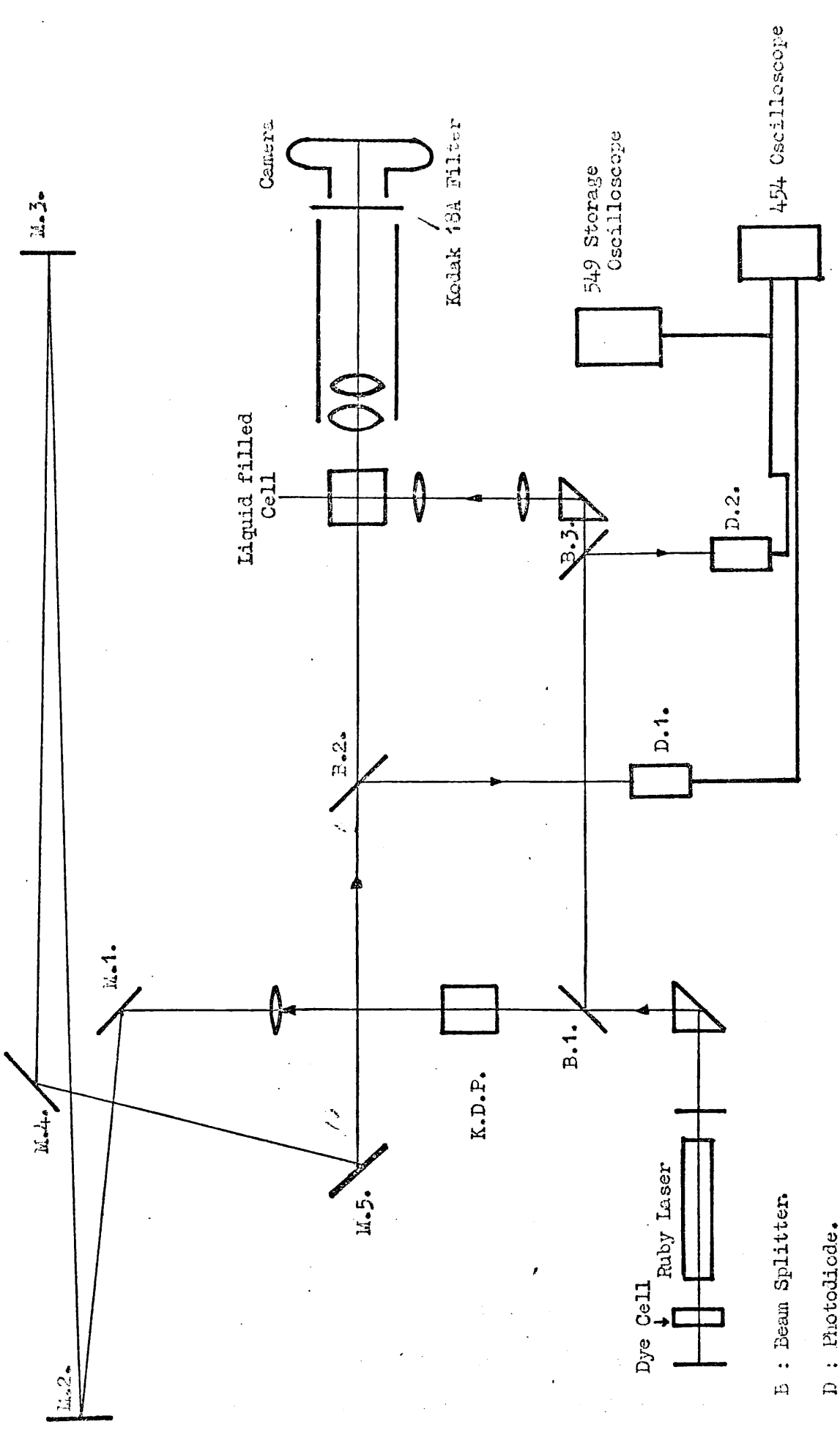

PHOTOGRAPHY OF LASER-INDUCED SHOCK WAVES BY FREQUENCY DOUBLED LIGHT.

FIGURE 7-1.

The long path lengths involved created extreme difficulties of alignment. The second harmonic light has a refractive index different from that of the fundamental, and alignment of the entire system using the HE-Ne laser was impossible for this reason. The method used required the laser to be fired with the frequency doubled beam being detected on a suitable flourescent screen, and adjustments being made to the optical components inbetween laser shots. The procedure was made more difficult by the direction of the output beam from the ruby altering as the laser rod warmed up. Thus it was necessary to be sparing in the use of the laser. Front-coated aluminium mirrors were used throughout the system in order to avoid any losses at these surfaces. In spite of these precautions the second harmonic beam underwent a considerable loss of power before reaching the interaction region. This beam was also monitored on the Tektronix 454 oscilloscope.

The shadowgraph technique was used to produce photographs of the shock waves. The probe light passed through the cell in a parallel collimated beam illuminating an area with a diameter of 3 mm. A 35 mm camera was used with a 40 cm extension tube. The length of this tube made it necessary to reverse the camera lens so that it could be focused on to the object from a very small distance. This system produced approximately a 20:1 object to image ratio on the film, so that a pre-selected area of the illuminated region could be photographed at a high magnification.

The ruby light at the fundamental frequency was filtered out of the system using a Kodak Type 18A filter, this completely masked all red light scattered from the cell, but permitted the transmission of the ultra-violet second harmonic light into the camera. Some of the fundamental frequency light reflected directly off the metal target was so intense as to pass through the filter and be recorded on the Tri-X pan film (400 A S A). (See Fig.7.3(a)).

FIGURE 7-2.

LASER INDUCED SHOCK WAVES - DOUBLE PHOTOGRAPHIC LIGHT PULSE.

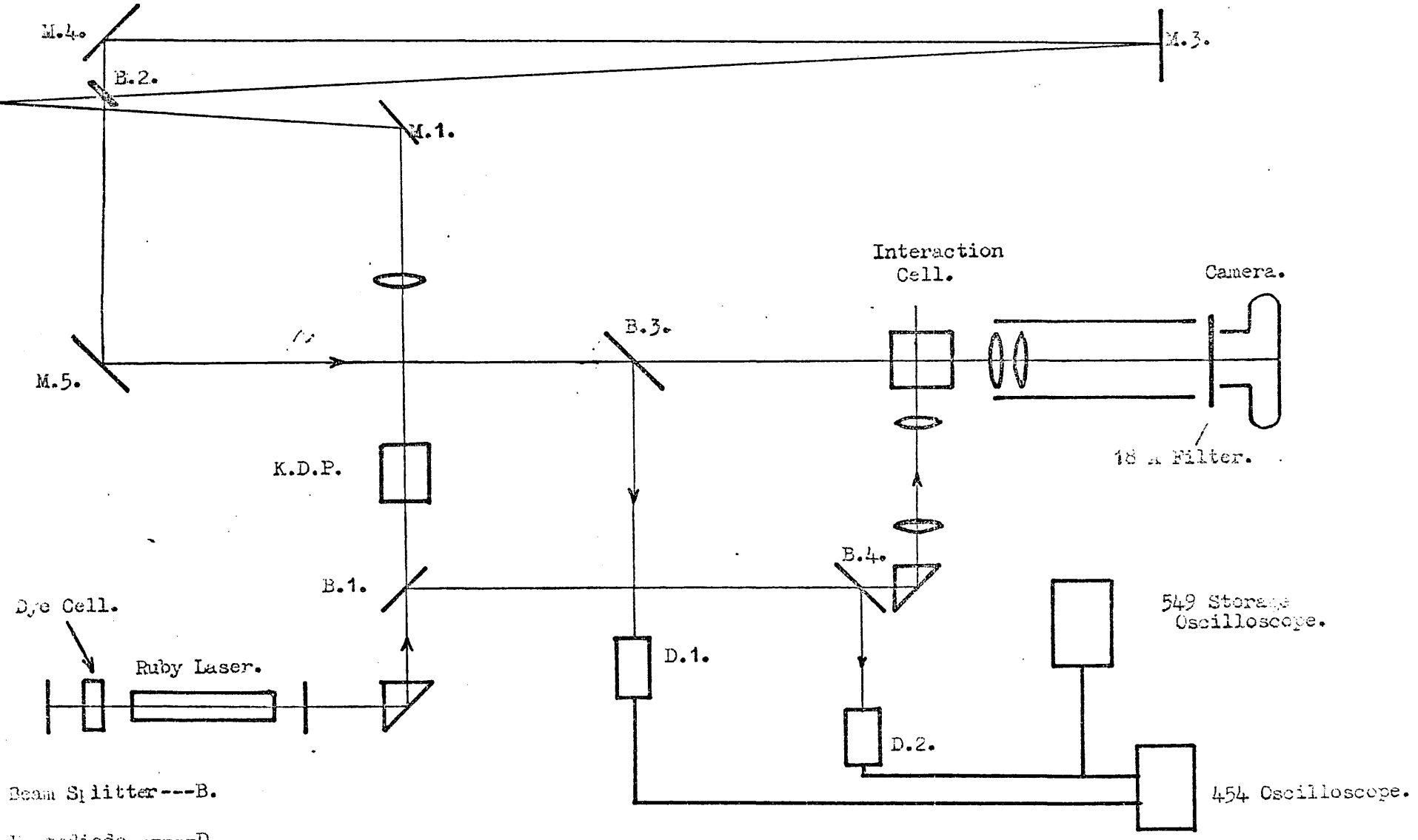

Fig.7.2 shows the alternative path delay system. In this case the second harmonic beam was reflected from beam splitter (D) which sent 25% of the light around a shortened path before reaching the water cell. The remaining light was directed around a greatly increased path length before reaching the cell. After allowing for the losses along the path, and an additional power loss in this beam due to a second pass through the beam splitter, the intensities of these beams were approximately equal. The problems of alignment were very much greater with the longer path length, and no great success was achieved in photographing both beams on the same film.

7.3 RESULTS OF INVESTIGATIONS

Figs.7.3→7.11 show the waves produced in the manner described above reference photographs are also shown to indicate the exact location of the incident fundamental frequency ruby beam (Fig.7.3(b), 7.8(b), 7.11(b)) and to show the background illumination from the frequency doubled beam in the absence of the shock-producing fundamental (Fig.7.5(a)).

Fig.7.4(b) is a low magnification photograph which gives an overall indication of the action of the fundamental beam. The remaining plates is this series are of the order of 50:1 magnification as indicated on the individual plates.

Three different time delays have been used for this photogrpahy:

(a) 86 ns delay path. (Figs.7.3(a), 7.4(a), 7.5(b) and 7.6(a).

(b) 48 ns delay path around the shortened optical path where the beam is reflected by beam splitter (B.2) in Fig.7.2. This delay is used in Figs.7.7 and Fig.7.8(a).

(c) A second exposure from the Fig.7.2 arrangement. The delay is 105 ns from the beam of light transmitted by the beam splitter (B.2) and reflected from (M.3) and (M.4). (See Figs.7.9, 7.10(a) and 7.11(a).)

Oscilloscope recordings showing the incident light pulses are shown in Fig.7.8. The difference in the optical path length to the detector, and the length of the leads to the oscilloscope displaces the first pulse by 30 ns .

On some shots with the Fig.7.2 arrangement, evidence of a third frequency doubled pulse was obtained. This pulse had travelled twice around the sub-circuit (M.3→M.4).

Unfortunately although both the two main photographic light pulses are monitored here, great difficulty was experienced in passing enough light around both optical paths to produce double exposure photographs. Indeed, this was not achieved before the crystal in the laser was damaged and further experimental work had to be curtailed.

The target wire at which the fundamental frequency beam was directed, was Nickrome 32 S WG (0.274 mm diameter).

The mechanisms of shock wave production that can be seen in the photographs presented here are :

(a) Absorption of light energy causing the evaporation of carbon particles in the liquid.

(b) Evaporation of material from the exposed face of the target.

(c) The electrical breakdown of the liquid.

(d) Reaction in the wire produced by the evaporation of material (ablative pressure).

In Fig.7.5(b) it can be seen that the shock wave produced from the surface of the wire follows the contours of the front face. This is true also in Fig.7.4(a) where an acoustic wave is produced. Thus from these plates it can be assumed that the shock wave facing the incoming beam is cylindrically shaped for a uniform wire. Figs.7.3(b), 7.8(b) and 7.11(b) shown the width of the fundamental beam. This was focused on to a point just beyond the liquid cell, so the whole width of the wire was intensely irradiated.

The explosion of carbon particles can be seen. In Fig.7.6(a) an average shock velocity 1.7×10^3 m.s^{-1} is produced. This wave appears to be perfectly spherical even from particles as large as 0.1 mm diameter.

The breakdown of the liquid can be seen in Fig.7.8(a), this can be compared to Fig.7.8(b) which shows the bright flashes of light produced by the action of the fundamental beam in that region.

The mean velocity of the spherical waves in Fig.7.5(b) is 1.9×10^3 m. s^{-1} compared to 2.2×10^3 m.s^{-1} for the cylindrical wave. A similar result is produced from Fig.7.6(a).

Figs.7.7 and 7.8(a) show no evidence of a forward travelling shock wave, however in Figs.7.4(a) and 7.5(b) such a wave is clearly visible. Thus, it seems that after the 48 ns delay in the former cases, this wave is still within the wire. Whereas by the time 86 ns have elapsed (Figs. 7.3(a) and 7.5(b)) the wave has emerged on the far side.

Figs.7.9 and 7.10(a) also show a forward-going shock wave. These photographs were aimed at showing a double exposure (48 ns and 105 ns delays). However, examination of the backward-going wave indicated only a single image. Thus, the double wave which has passed through the wire must have been produced by a bifurcation of the wave and not a double exposure. If a double exposure had taken place, this wave would have had to have moved subsonically inbetween the two exposures to account for the appearance of the transmitted wave.

The velocity of the forward going wave is very much higher than the backward going wave leaving the surface of the wire $\sim 10^4$ m.s^{-1}. This wave is produced as a reaction to the evaporated material from the surface (ablation pressure), and so travels radially inward. There will be a power distribution within the shock wave front so that maximum pressure is produced from the section of the wire surface which faces the laser radiation normally. The more obliquely oriented regions will receive relatively less energy per unit area.

As the wave moves towards the centre of the wire, it will accelerate ($u = \varphi_1 \frac{(\eta)}{R}$). However, the whole of the wave will not reach the centre simultaneously. The slower parts of the wave front which are travelling at an angle to the direction of the laser beam will reach the centre just after the region reaches an intensely shocked state. The bifurcation of the transmitted wave is probably due to such an interaction.

Attempts were made to study such a wave. This wave-form can be produced by placing a target, with a semi-cylindrical groove running across its width, in front of the fundamental beam. The second harmonic light was directed along the groove, parallel to the surface; unfortunately the work had to be curtailed due to fracture of the ruby crystal, before a good photograph could be taken. Fig.7.11 shows the results obtained. Fig.7.11(b) shows the cross-section size of the fundamental, but in Fig.7.11(a) it can be seen that the plane was not aligned truly parallel to the second harmonic, so a series of interference fringes was produced by reflection from the face of the target. Unfortunately the region of interest is obscured so that no significant measurements can be made on that part of the shock wave which can be seen, but it does appear that this wave has moved considerably further in the time, than the equilavent outward going wave produced from the surface of the wire. Thus the acceleration of the wave is demonstrated to have taken place due to the decrease in the radius of the wave as it focuses itself during its movement away from the surface of the target.

Further work with this technique would have taken place if the damage to the ruby in the laser had permitted. However, this work shows that the technique provides a convenient way of studying shock waves on the microscale.

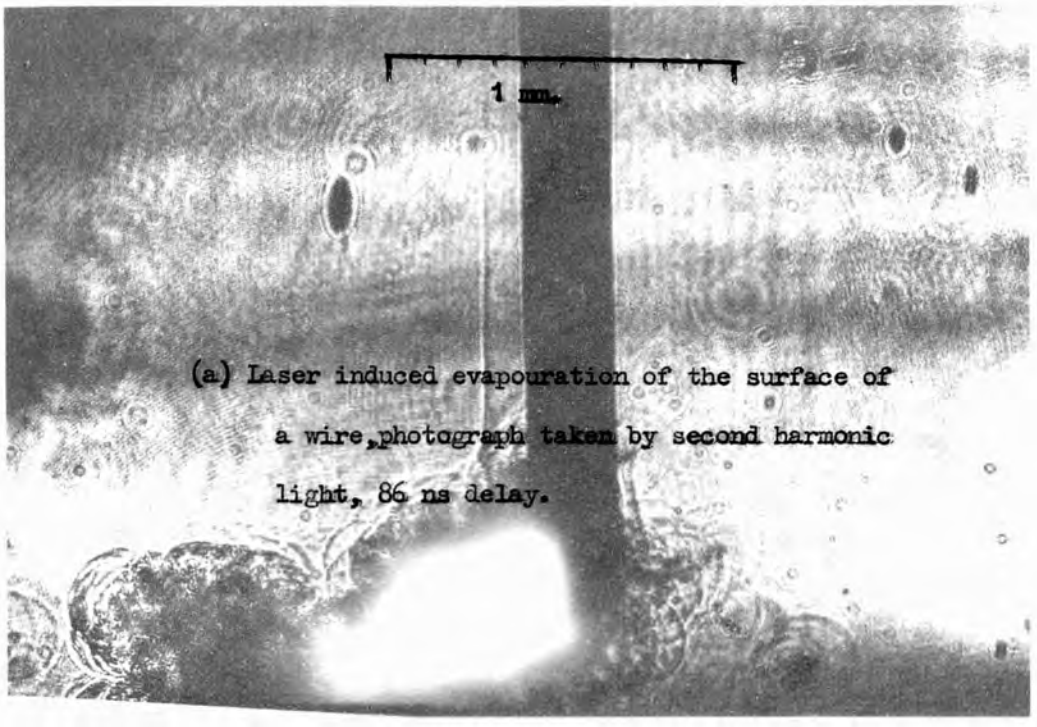

(a) Laser induced evapouration of the surface of a wire, photograph taken by second harmonic light, 86 ns delay.

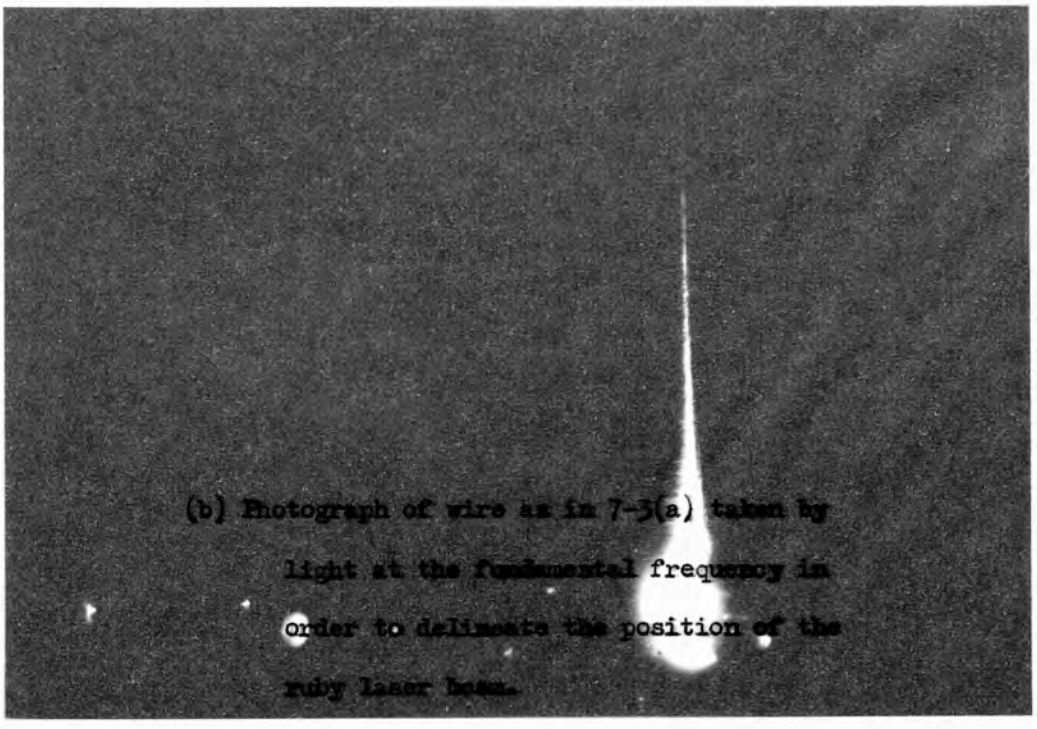

(b) Photograph of wire as in 7-3(a) taken by light at the fundamental frequency in order to delineate the position of the ruby laser beam.

FIGURE 7-3.

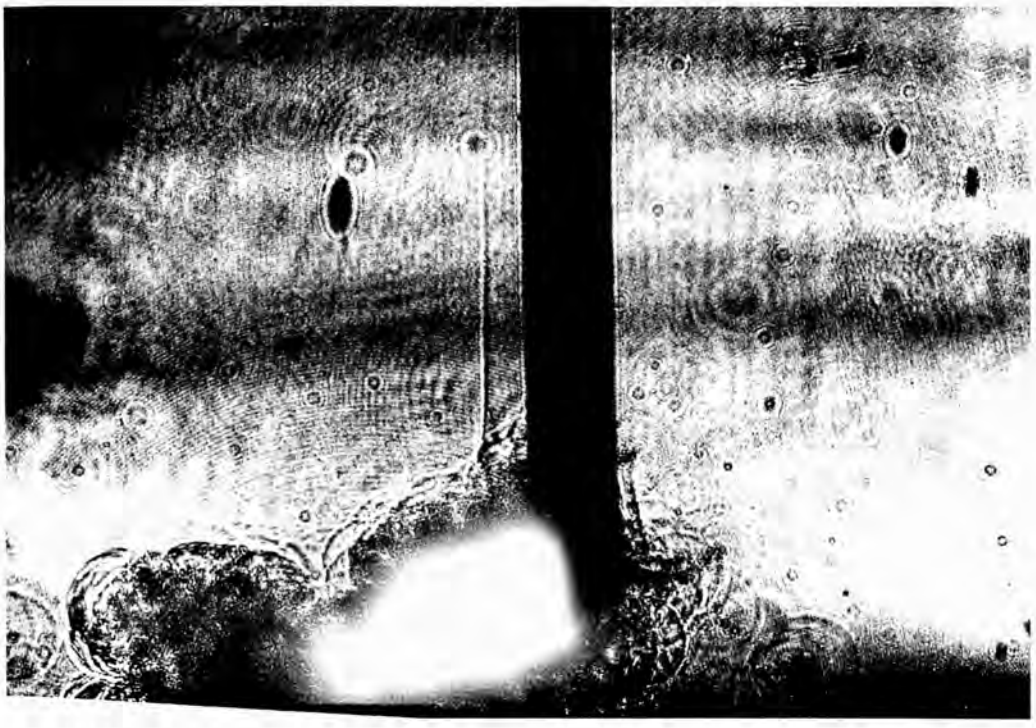

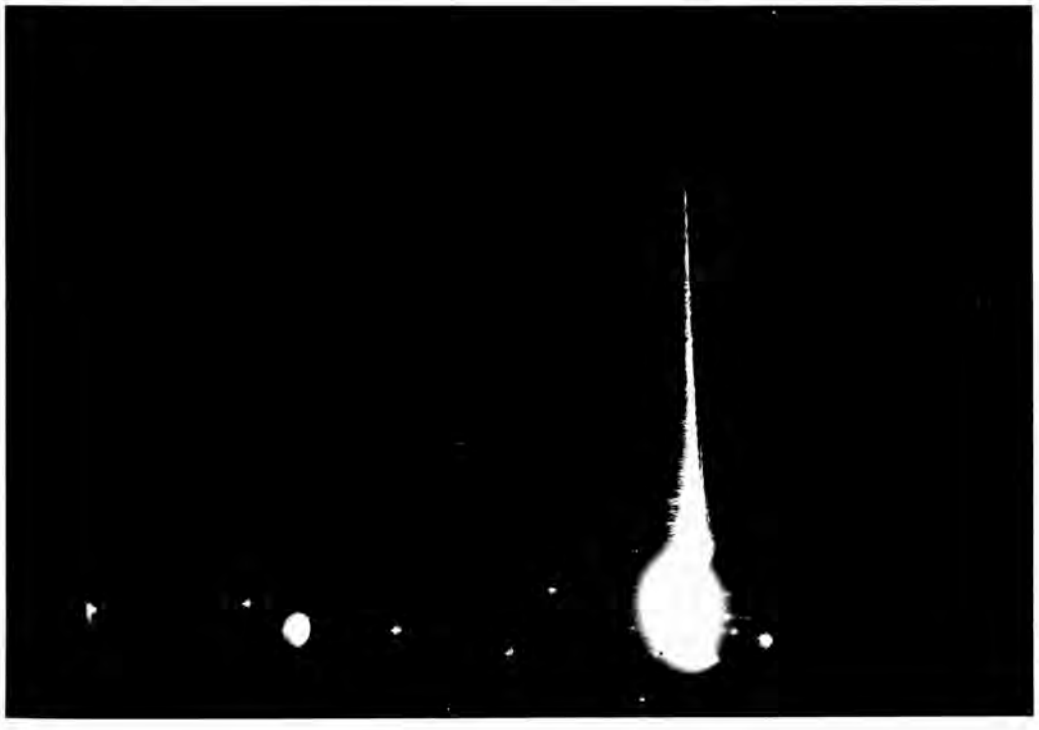

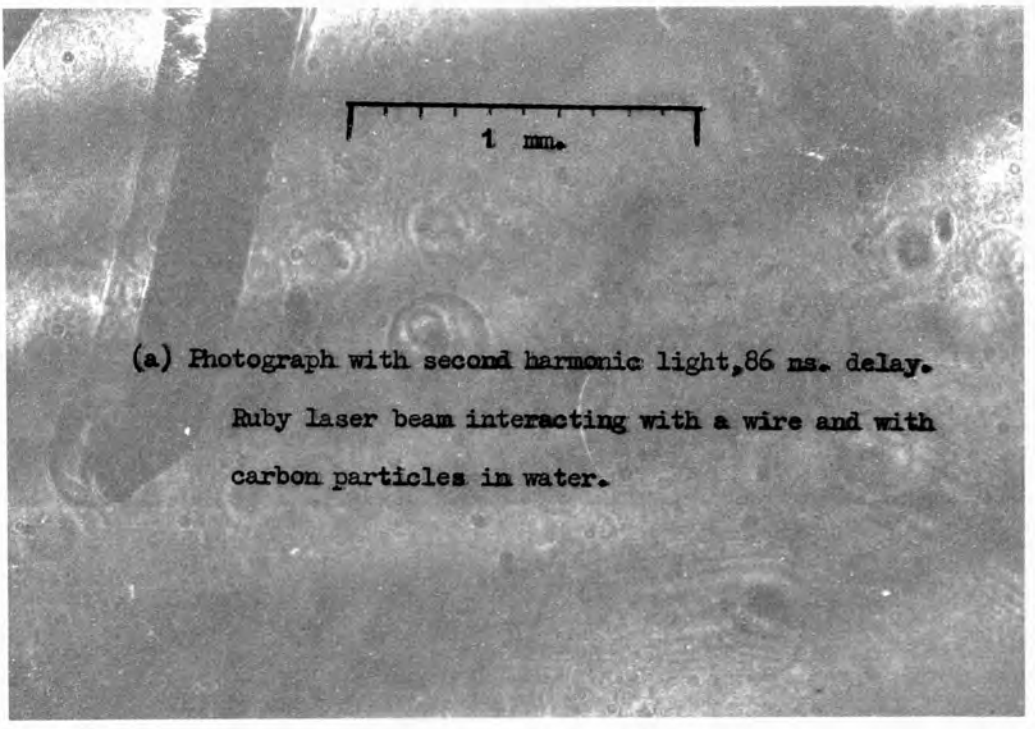

(a) Photograph with second harmonic light, 86 ns. delay. Ruby laser beam interacting with a wire and with carbon particles in water.

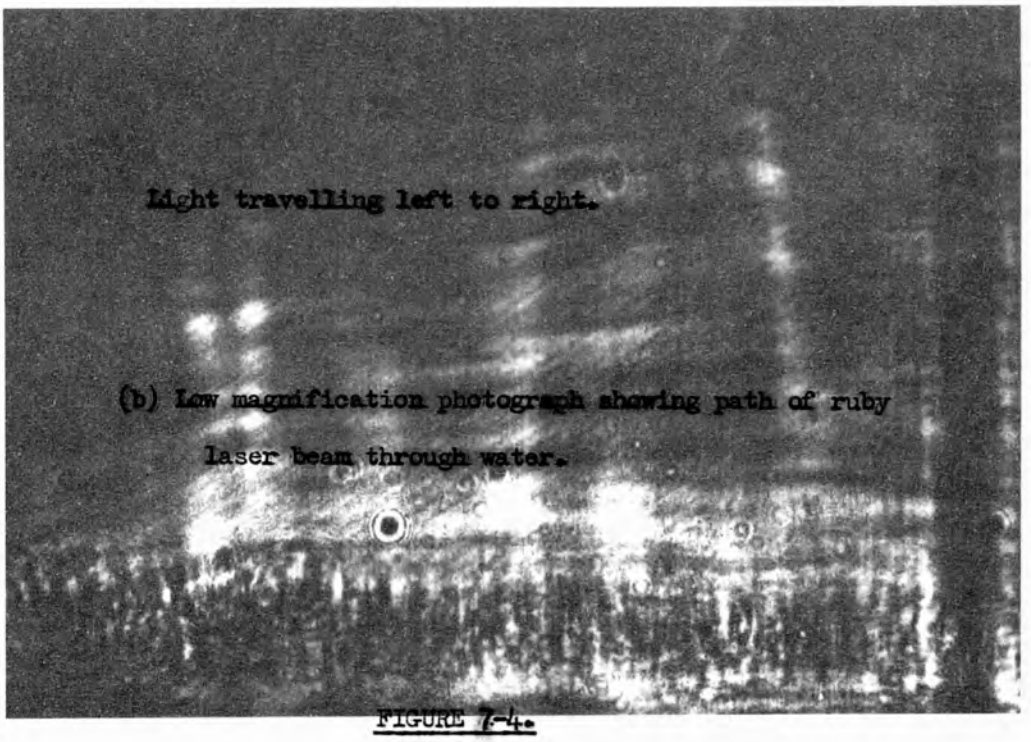

(b) Low magnification photograph showing path of ruby laser beam through water.

FIGURE 7-4.

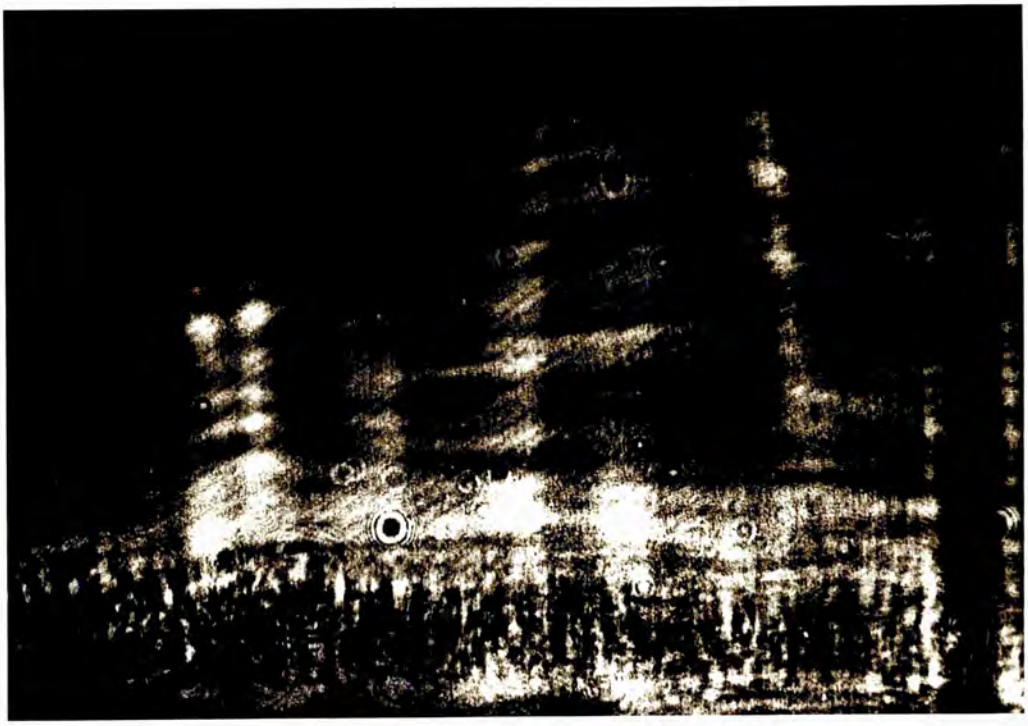

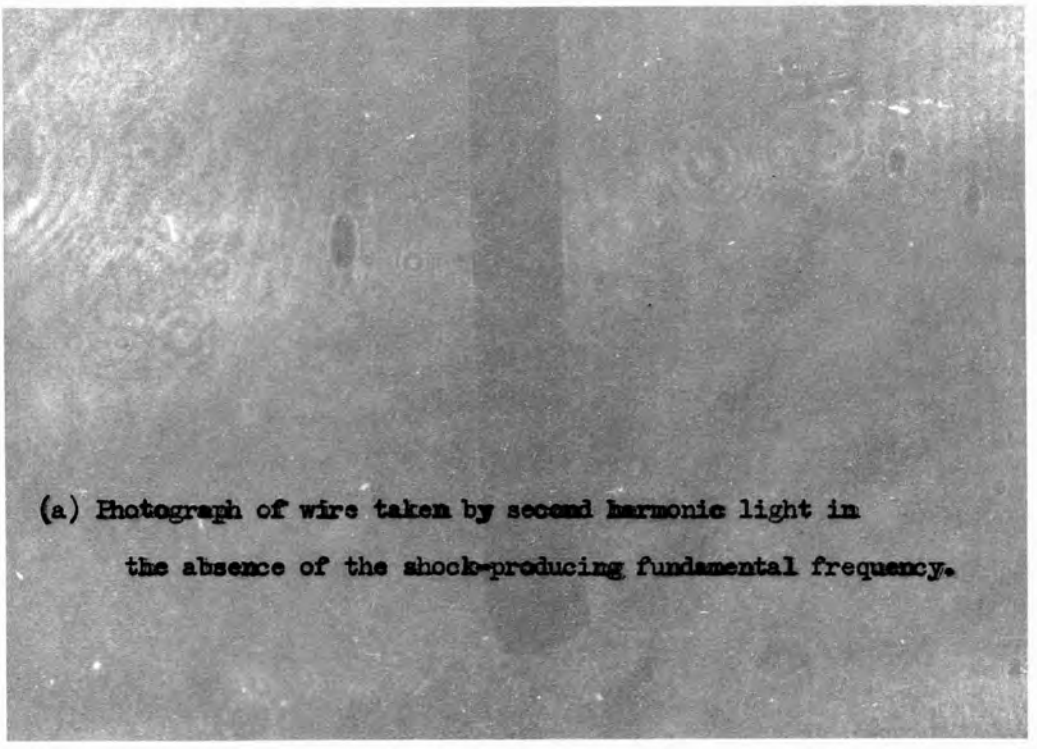

(a) Photograph of wire taken by second harmonic light in the absence of the shock-producing fundamental frequency.

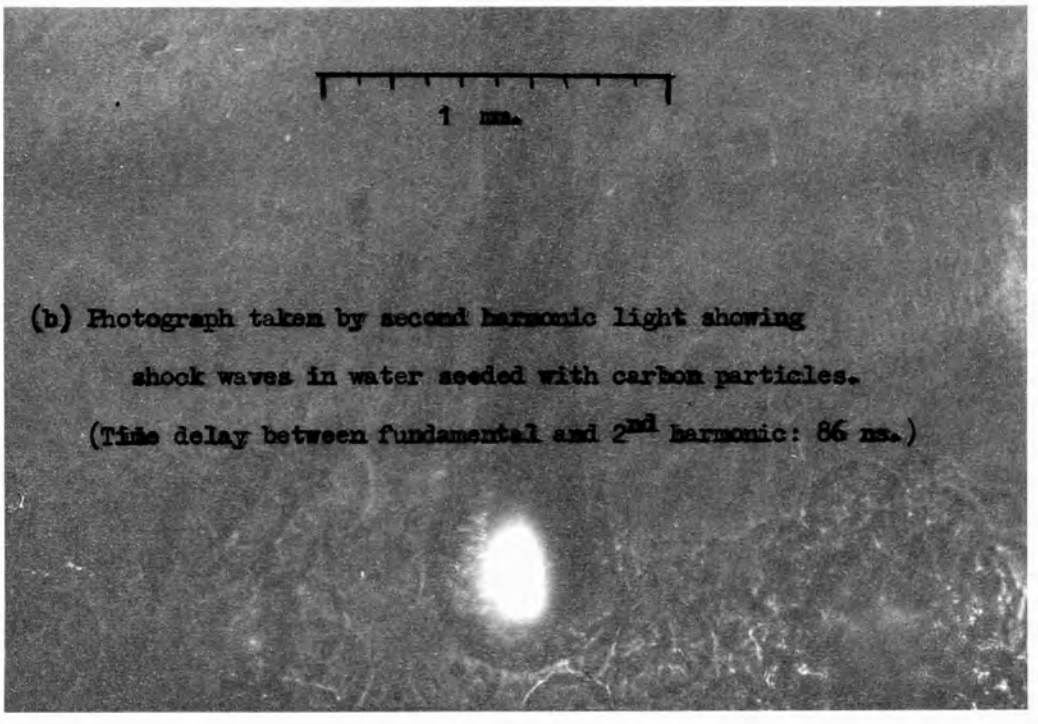

(b) Photograph taken by second harmonic light showing shock waves in water seeded with carbon particles. (Time delay between fundamental and 2nd harmonic: 86 ns.)

FIGURE 7-5.

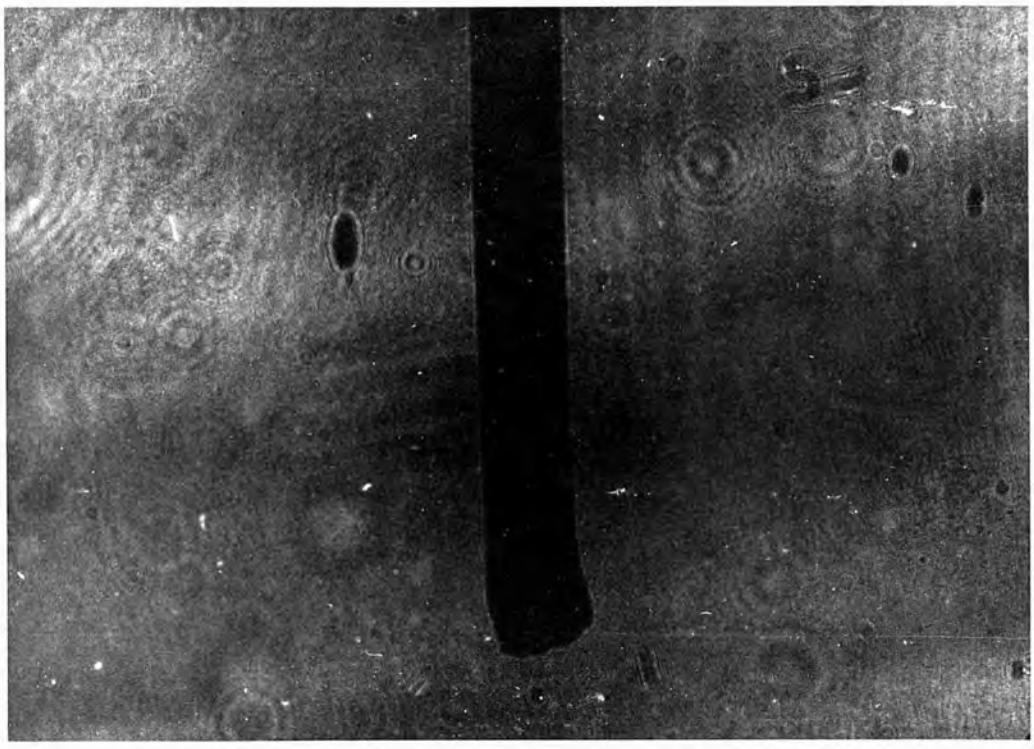

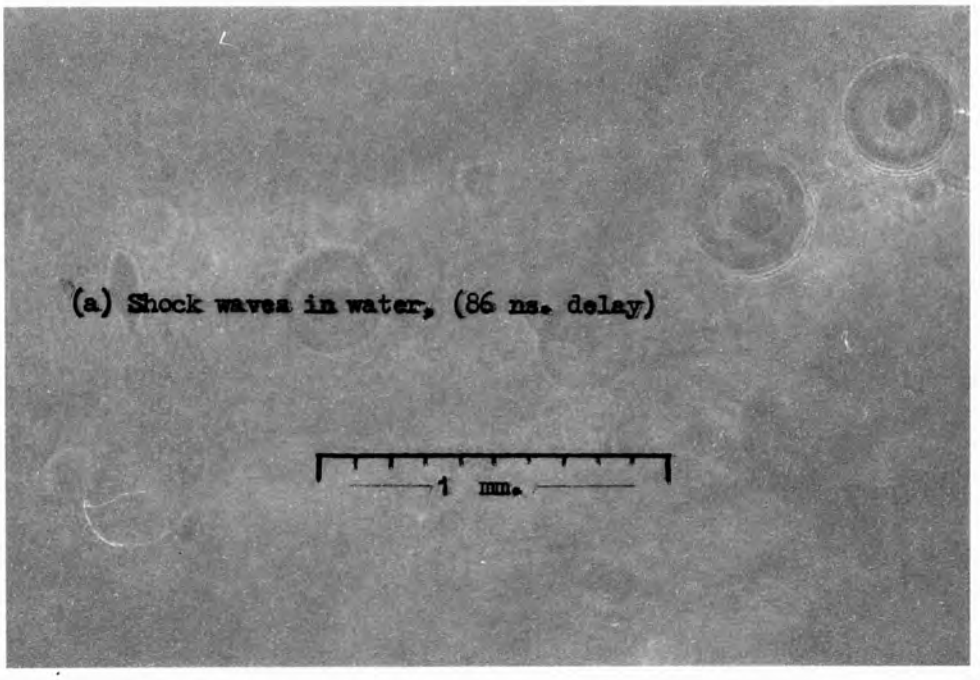

(b) and (c) show time delay between fundamental and 2nd harmonic light pulse

2nd harmonic is displaced due to 30 ns. delay line.

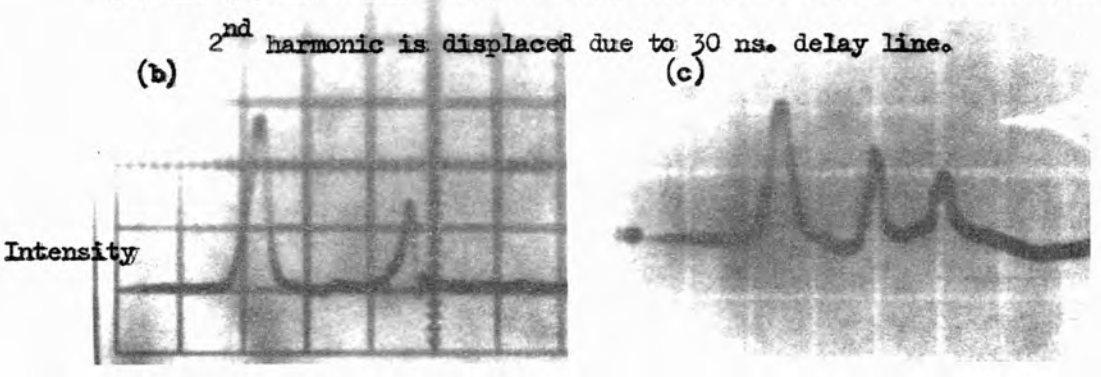

FIGURE 7-6.

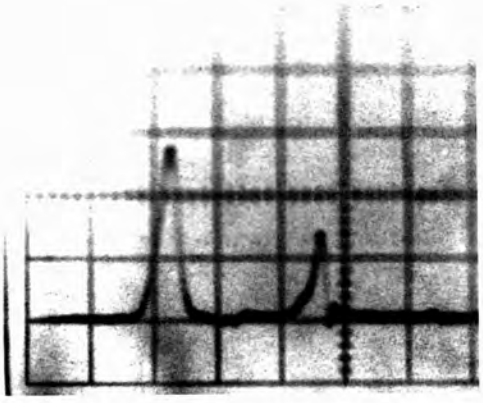

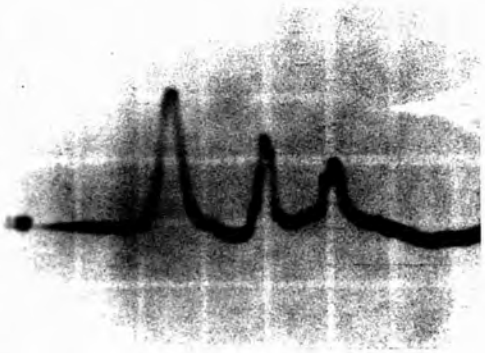

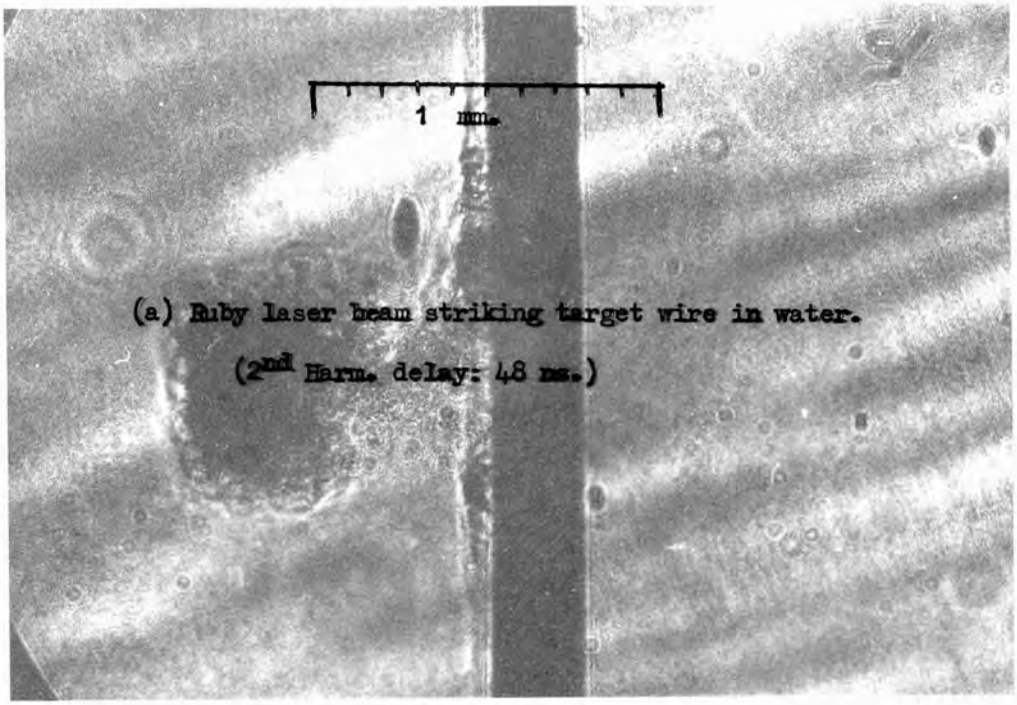

(a) Ruby laser beam striking target wire in water.
(2^{nd} Harm. delay: 48 ns.)

(b) Ruby laser beam striking target wire in water.
(2^{nd} Harm. delay: 48 ns.)

FIGURE 7-7.

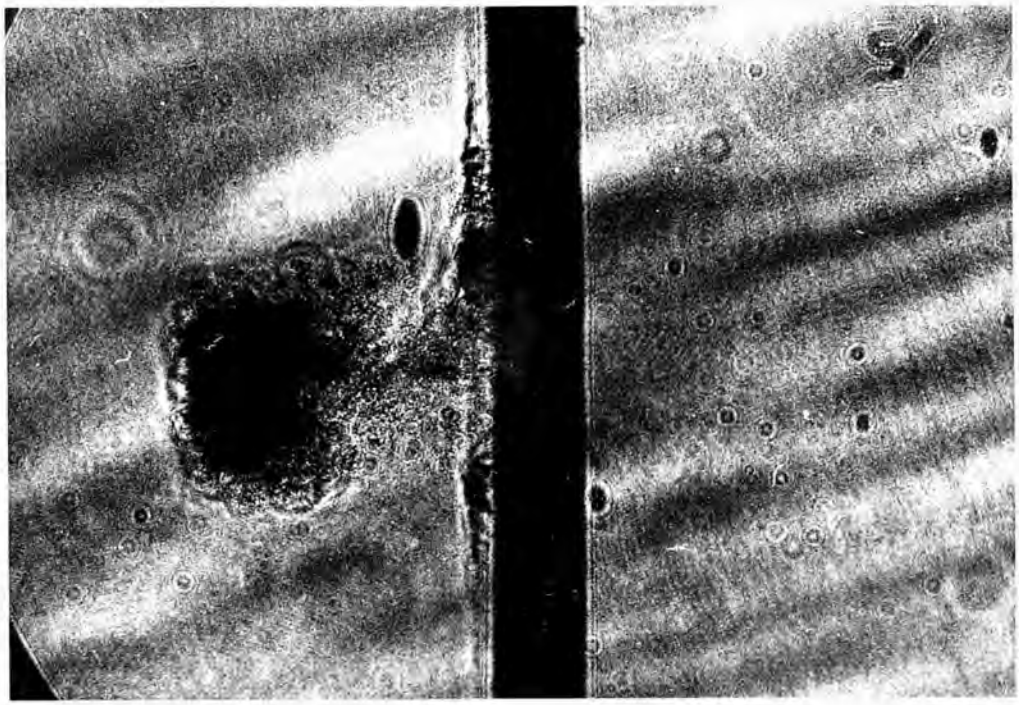

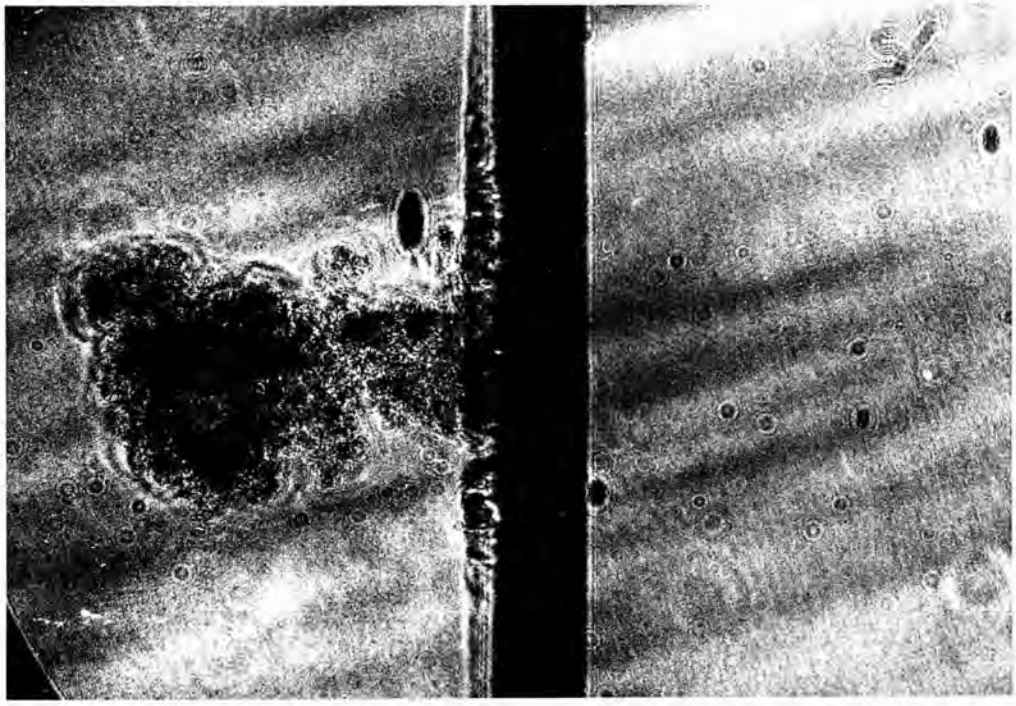

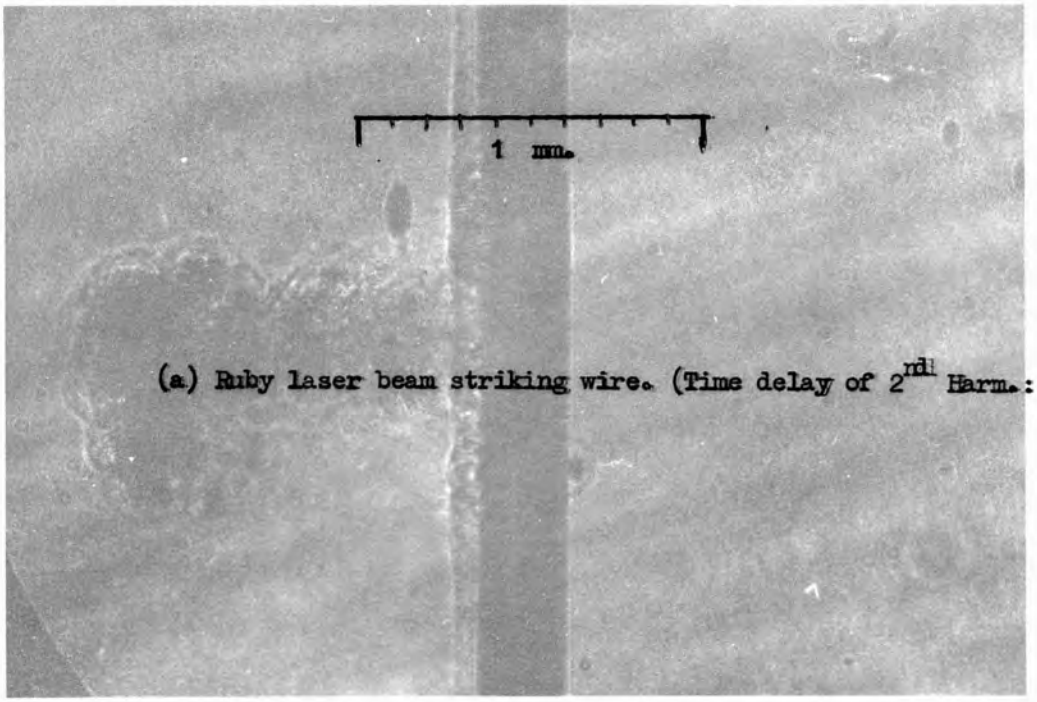

(a) Ruby laser beam striking wire. (Time delay of 2nd Harm.: 48 ns.)

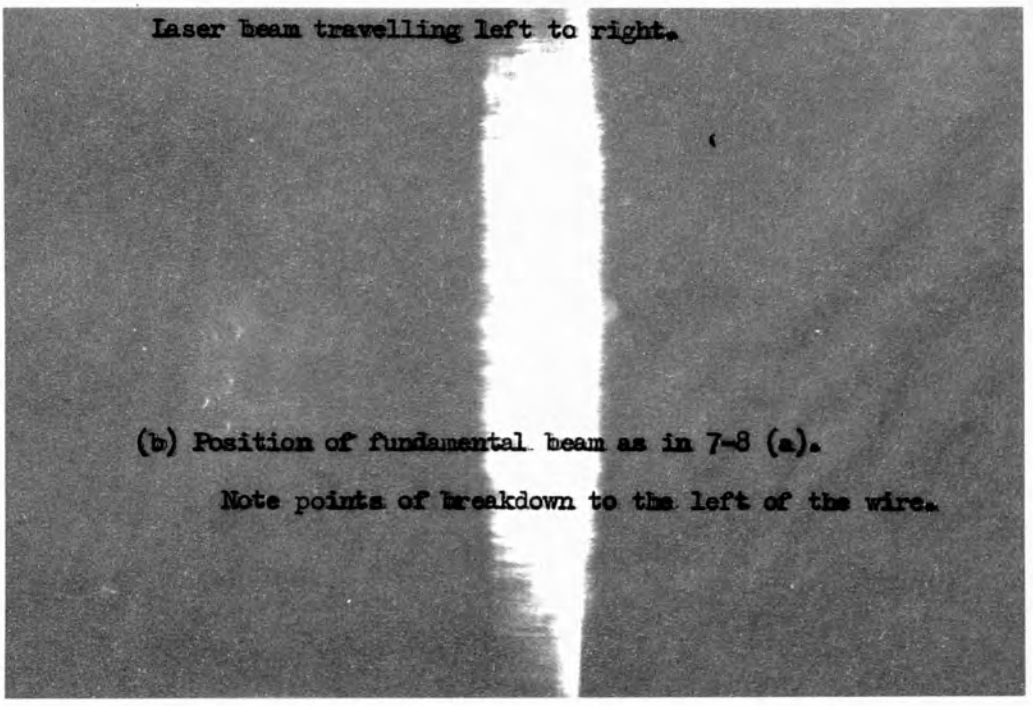

(b) Position of fundamental beam as in 7-8 (a).

Note points of breakdown to the left of the wire.

FIGURE 7-8.

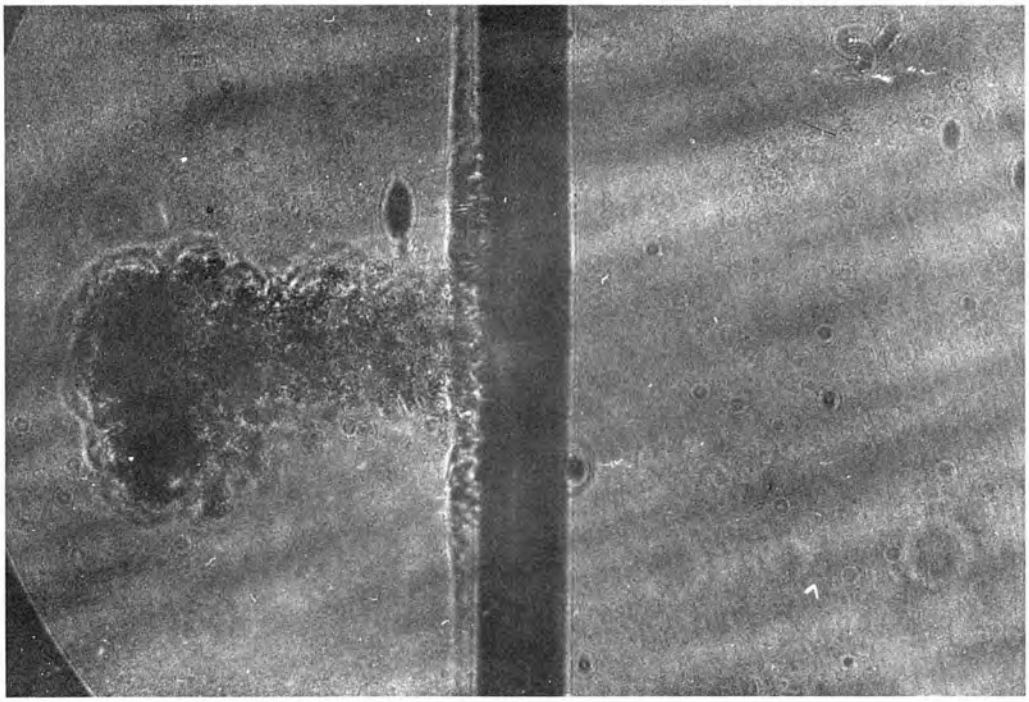

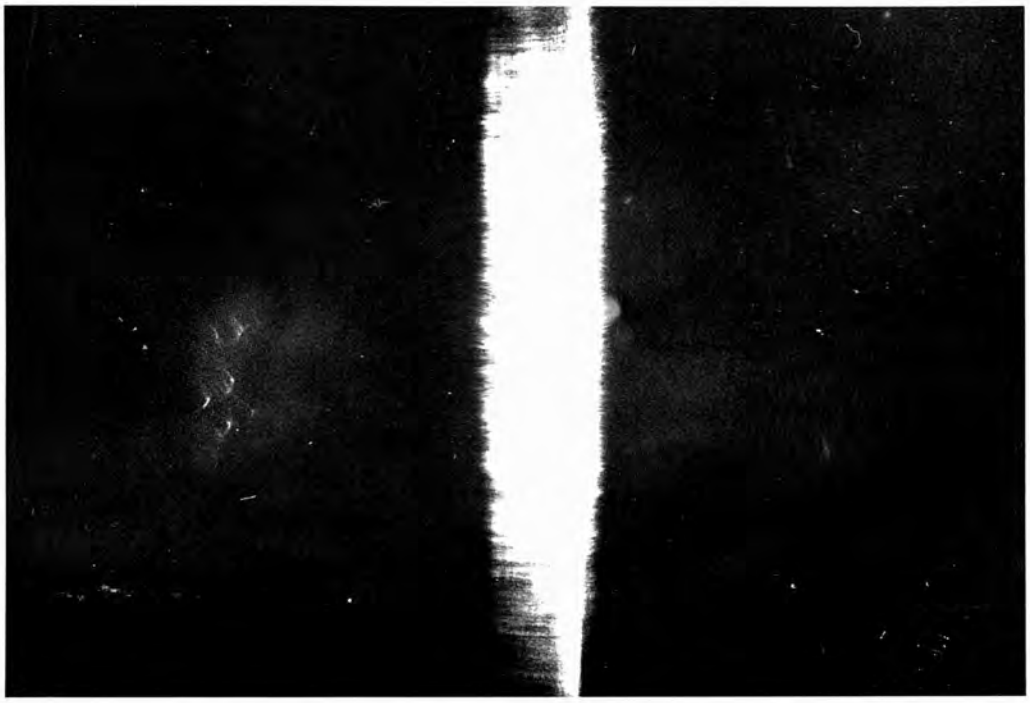

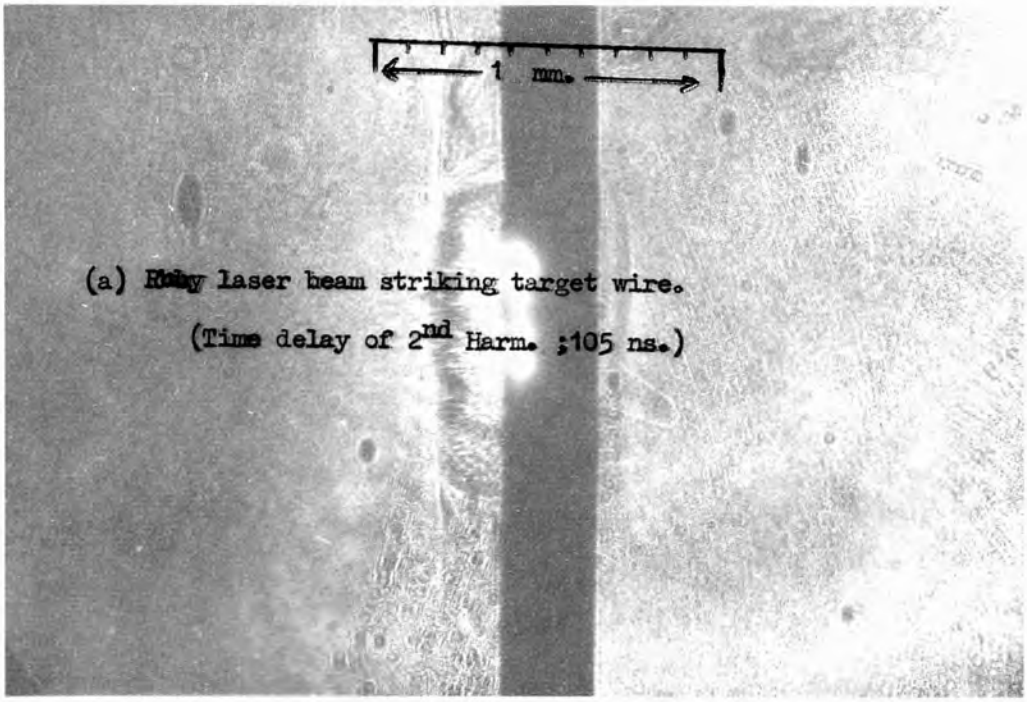

(a) Ruby laser beam striking target wire.

(Time delay of 2nd Harm. ;105 ns.)

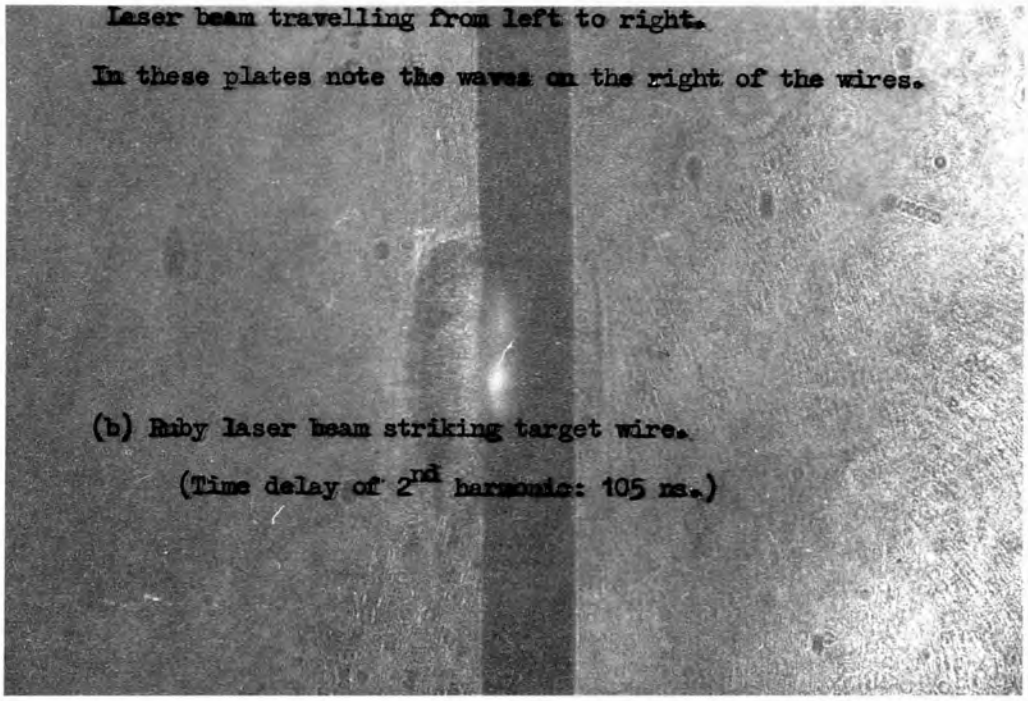

Laser beam travelling from left to right.

In these plates note the waves on the right of the wires.

(b) Ruby laser beam striking target wire.

(Time delay of 2nd harmonic: 105 ns.)

FIGURE 7-9.

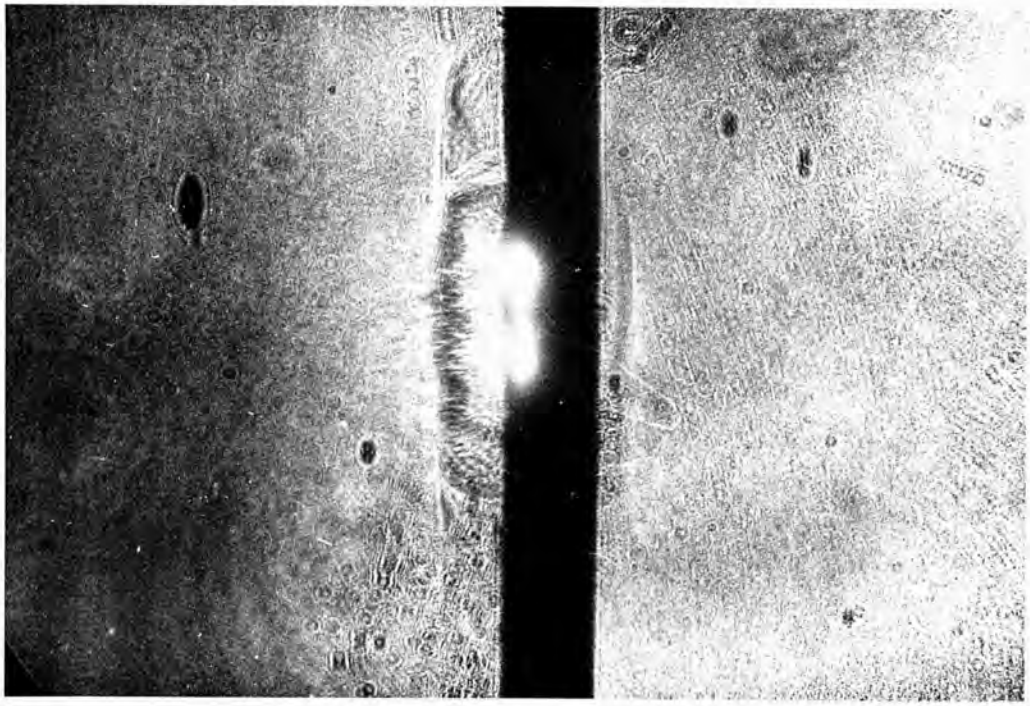

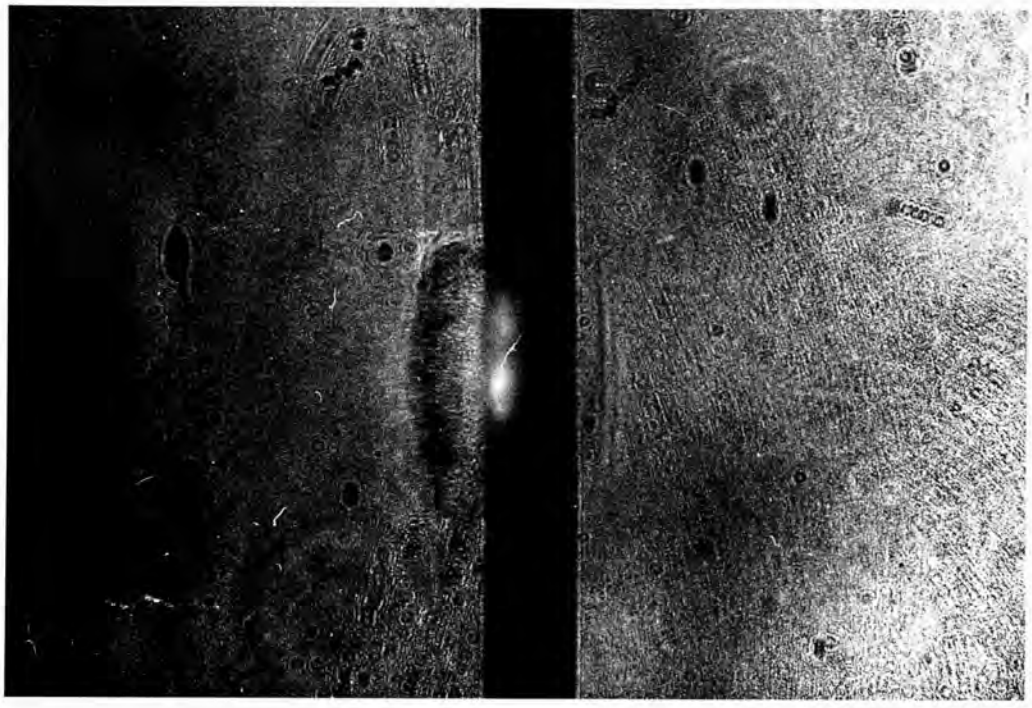

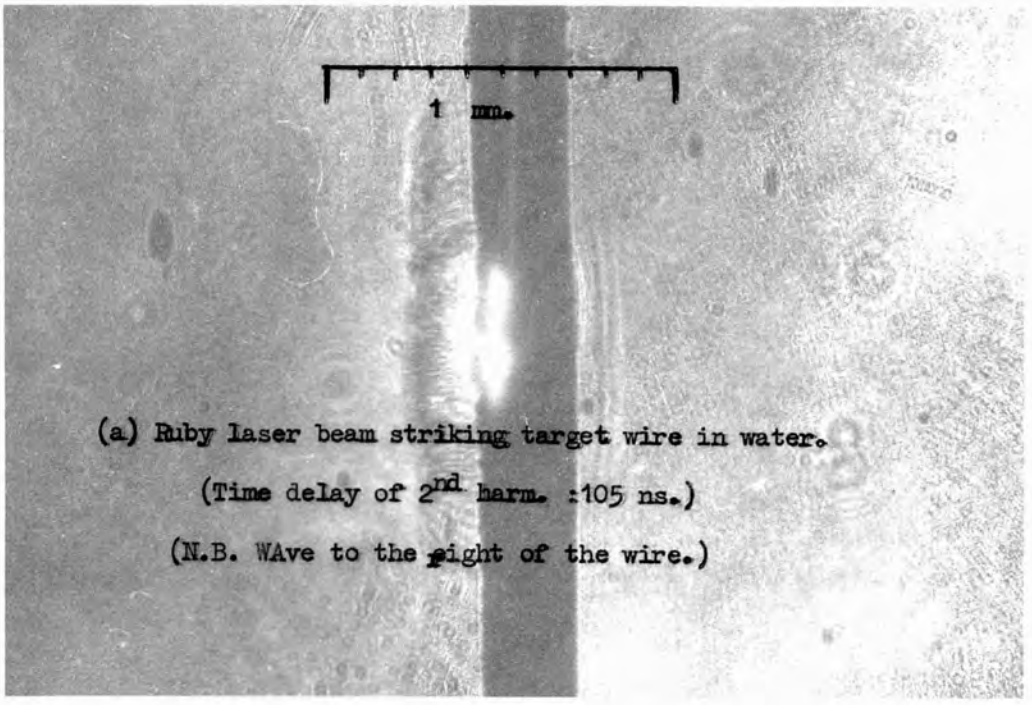

(a) Ruby laser beam striking target wire in water.
(Time delay of 2nd harm. :105 ns.)
(N.B. WAve to the right of the wire.)

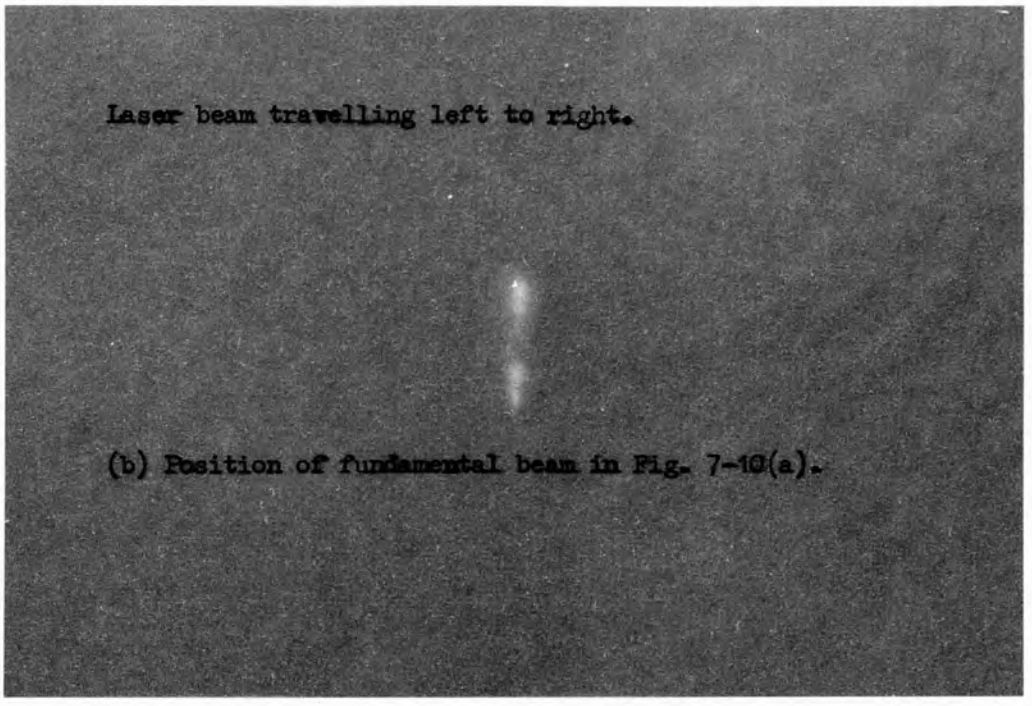

(b) Position of fundamental beam in Fig. 7-10(a).

FIGURE 7-10.

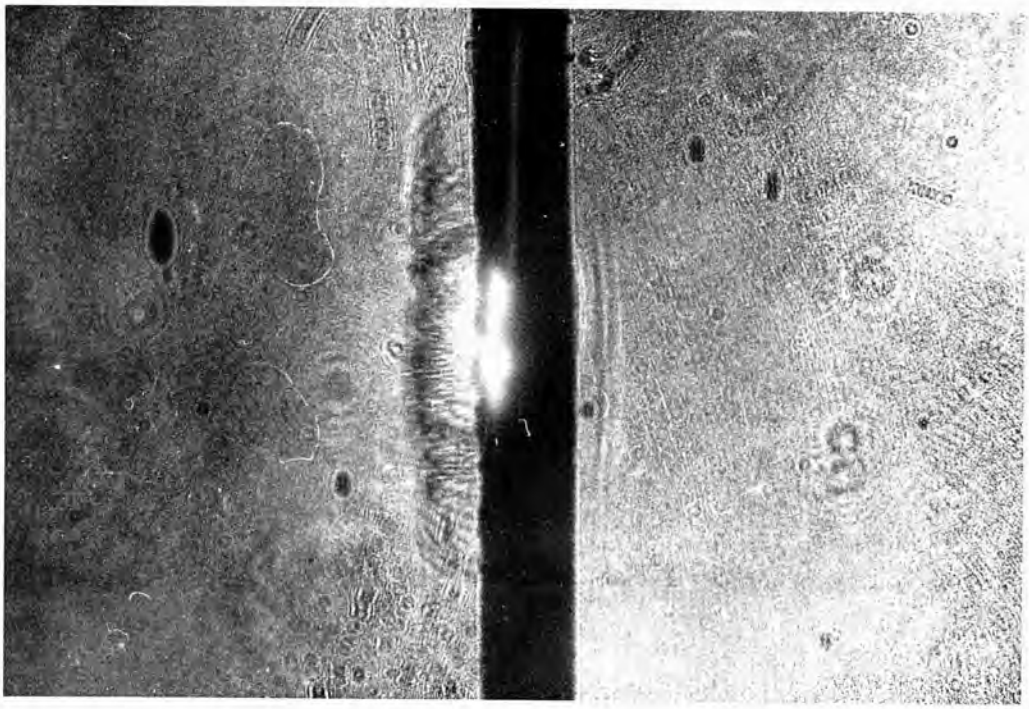

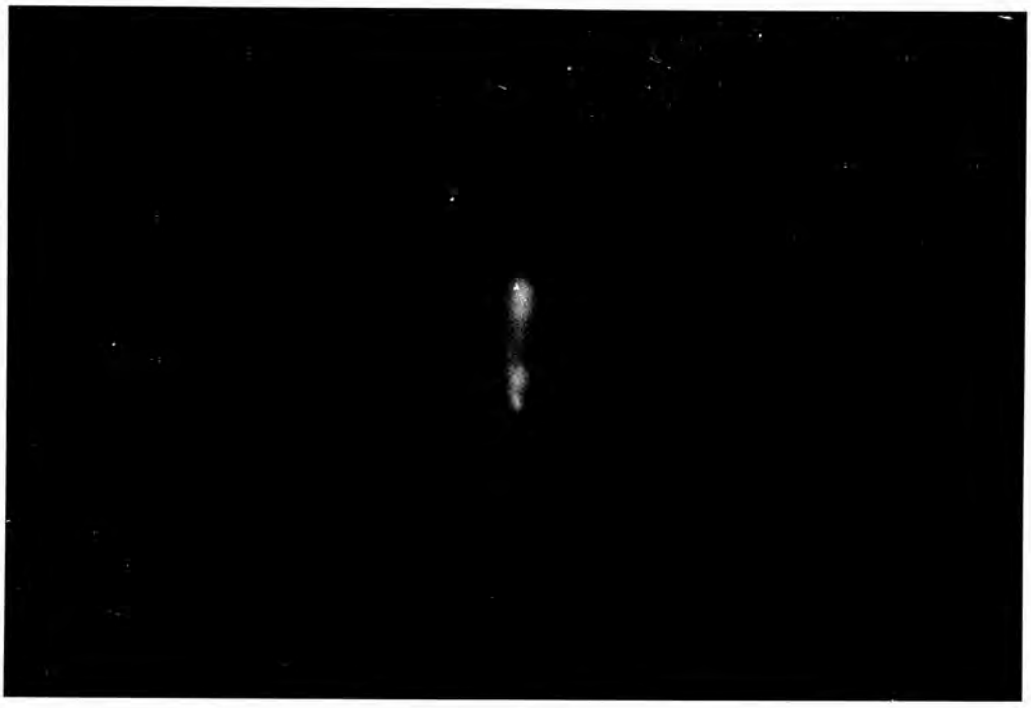

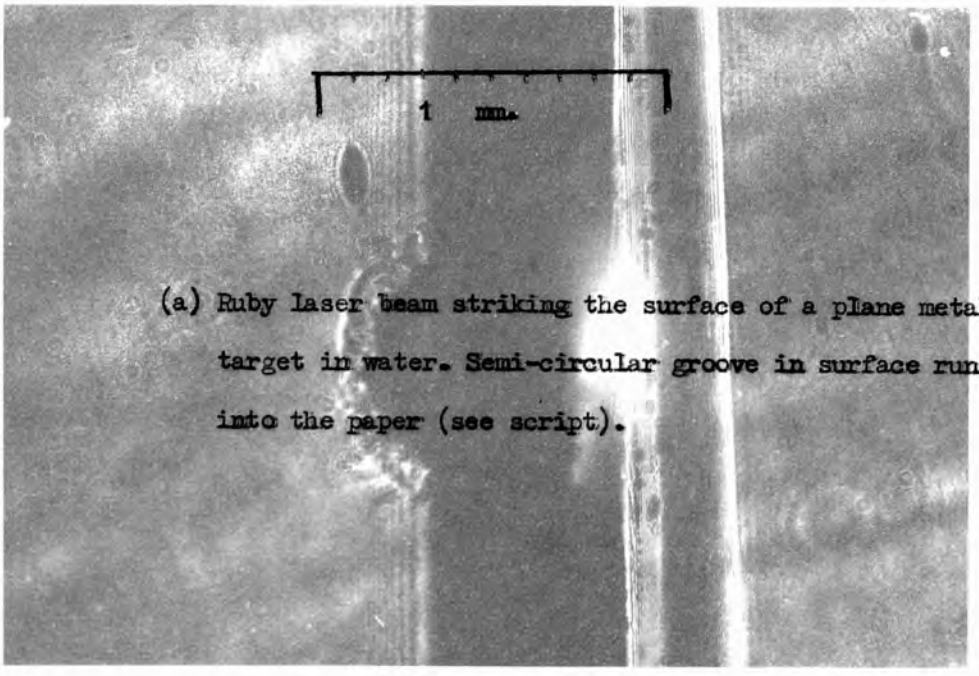

(a) Ruby laser beam striking the surface of a plane metal target in water. Semi-circular groove in surface runs into the paper (see script).

Laser beam travelling from left to right.

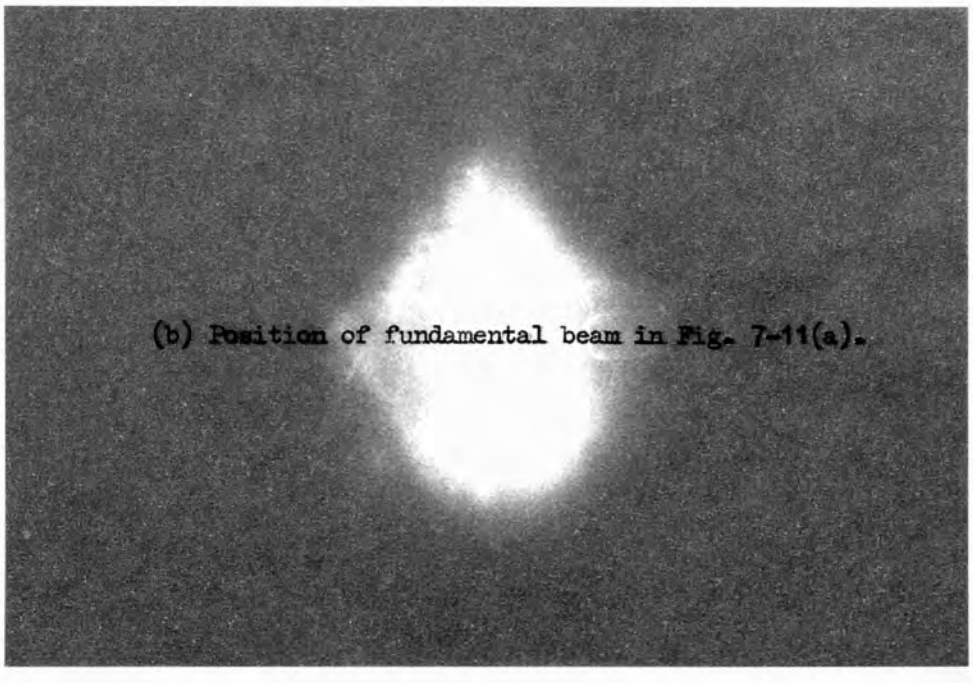

(b) Position of fundamental beam in Fig. 7-11(a).

FIGURE 7-11.

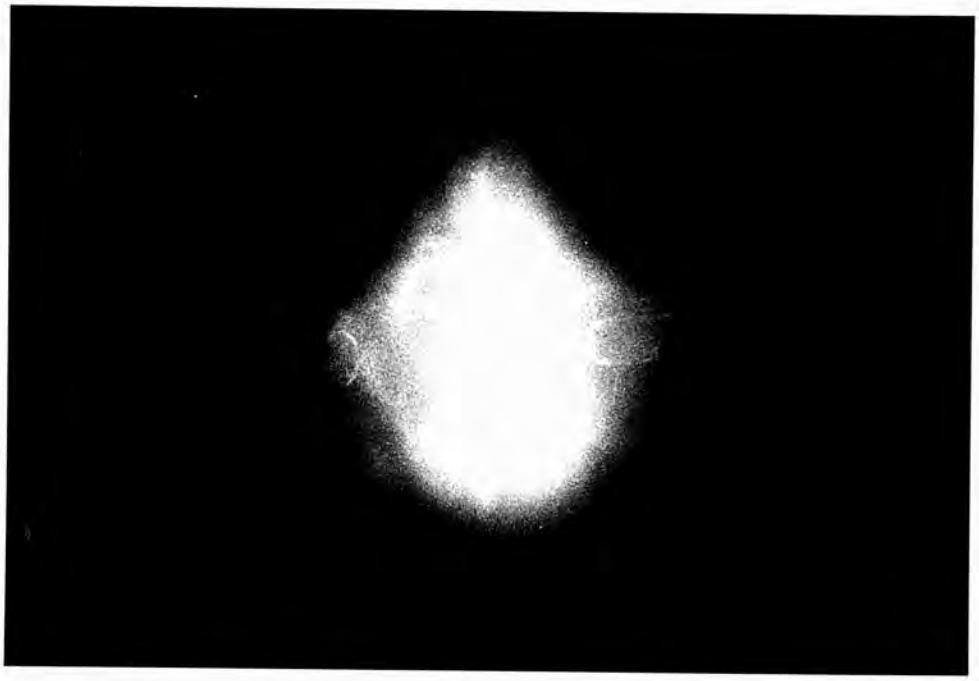

CHAPTER VIII

GENERAL CONCLUSIONS

The experimental work in this thesis falls naturally into three parts:

(1) Initial studies of shock wave and related phenomena produced by exploding wires.

(2) The examination of a high speed optical shutter for possible use in shock wave photography, and the study and development of the cell to demonstrate some of the related phenomena which the cell exhibits.

(3) The optical production of shock waves, together with the photography of the wave propagation and velocity measurements.

The initial studies have shown some of the possible uses of exploding wires as shock wave producers. On the micro-scale, wires have been shown to be reliable shock wave generators. The number of associated phenomena which have been observed when looking at exploding wires at low energies demonstrate some aspects of wire disintegration.

The low energy range for exploding wires has not hitherto received as much attention from researchers as has the higher energy range when the wire vapourization is accompanied by a cylindrical shock wave. The behaviour of molten wire droplets has been shown to be along the same lines as has been demonstrated by Lane et al[106] for water droplets in an air flow.

The work on the development of the optical shutter has shown how the Kerr effect may be used to render electric fields visible. The main problems of Kerr cell operation, the balance of large Kerr switching capability with capacitance, has been solved, though at the cost of reduced aperture. The development of the knife-edged cell and the subsequent construction of a razor blade stack cell shows more processes associated

with electric fields in liquids. The use of a highly unsymmetric electrode geometry (e.g. the razor blade state) makes possible the attainment of extremely high electric fields when relatively low voltages are applied across the cell. Thus the difficulties of switching the applied potential across the electrodes are diminished. The cell can be used to switch light into the diffraction pattern produced from the induced grating in the liquid. This process is electrostrictive and thus very fast.

The high speed photography of optically produced shock waves has been solved by the means of a beam splitter and an optical delay path, so that part of the light pulse which produces the shock wave is also used to photograph the wave. The system has the advantage of zero jitter in the photographic pulse. The time delay is easily adjusted by varying the length of the delay path. Double exposures are theoretically possible, indeed a triple photographic light pulse has been detected.

Unfortunately the failure of the ruby crystal curtailed experimental work before good double exposure photographs could be taken. The results so obtained showed various processes in action producing shock waves and acoustical waves. The process of electrical breakdown optically induced in the liquid has been shown giving rise to an associated shock wave. The evaporation of surface material by focused laser radiation onto a target metal wire has been shown to produce a shock wave following the contours of the surface. A second inward-going ablation wave has been shown to be associated with the removal of surface material. The inward travelling wave has a greater velocity than the wave travelling straight into the liquid. The method of shaping the target can produce shock waves of pre-determined shaping and should prove convenient for the study of such waves. Further work along these lines would have to take place in order to give a more detailed evaluation of the technique.

APPENDIX I

STIMULATED BRILLOUIN SCATTERING

This is the phenomenon in which a very intense forward going wave $E_0 \cos(\omega_0 t - k_0 x)$, is partically backscattered in the normal Brillouin scattering process from propagating density fluctuations in the liquid. The backscattered wave is frequency shifted according to the Doppler effect to produce $E\cos(\omega t + kx)$. The superposition of these two waves, provided the intensity is large enough, results in the production of difference frequency fluctuations in the polarization of the medium. Thus, in the high field case, if $P = \chi_1 E + \chi_2 E^2 + \chi_3 E^3 \ldots$ etc. it follows in the case of homogeneous materials, that the component of P in phase with E is given by:

$$P = \chi_1 E + \chi_3 E^3 + \ldots \qquad \ldots (A1.1)$$

where the even powers produce unidirectional components only. This may be written:

$$P = \chi E \qquad \ldots (A1.2)$$

where $\chi = (\chi_1 + \chi_3 E^2)$. It can be seen that P has frequency components ω_0 and ω arising from the linear term, and from the E^2 term there will be components in $2\omega_0$, 2ω, $\omega_0 - \omega$ and $\omega_0 + \omega$.

A full expression for P would be:

$$P = \chi_1 \left[E_0 \cos(\omega_0 t - k_0 x) + E\cos(\omega t + kx)\right] + \chi_3 \left[E_0 \cos(\omega_0 t - k_0 x) + E\cos(\omega t + kx)\right]^2 \qquad \ldots (A1.3)$$

The latter term becomes

$$\chi_3 \left[\tfrac{1}{2}E_0^2 \left[1 + \cos 2(\omega_0 t - k_0 x) + 1 + \cos 2(\omega t + kx)\right] + 2E_0 E\left[\cos\left([\omega_0 - \omega]t - [k_0 + k]x\right) + \cos\left([\omega_0 + \omega]t + [k_0 - k]x\right)\right] \qquad \ldots (A1.4)$$

Of these terms the difference frequency term will be very slowly varying in comparison with the summation terms. This frequency difference term constitutes a wave travelling in the same direction as the incident

wave with a phase velocity $(\omega_o - \omega)/(k_o + k) = v$.

The incident wave is backscattered from this polarization wave (or refractive index phase grating) and suffers in frequency shift

$$\frac{2v}{c} \cdot \frac{c}{\lambda} = \frac{vk_o}{\pi} = \frac{\omega_o - \omega}{k_o + k} \cdot \frac{k_o}{\pi} = 2(\nu_o - \nu) \qquad \ldots \text{(A1.5)}$$

since k_o and k differ by only a few parts in a million. That is to say that this main phase grating produces a frequency shift identical to that produced in the spontaneous Brillouin backscattering process.

APPENDIX II

LIST OF SYMBOLS USED IN VARIOUS CHAPTERS

CHAPTER I : Subscripts 1 = before shock; Subscript 2 = behind shock.

P = pressure

V = volume

S = entropy

ϵ_1 = internal energy = $h - pV$ where h = specific enthalpy

ρ = density

v = flow velocity w.r.t. the surface of discontinuity.

r = radius

h = specific enthalpy = $\epsilon + pV$, $dh = TdS + Vdp$

j = mass flux density at surface.

CHAPTER II : Subscripts 1 = in front of shock; Subscript 2 = behind shock.

R = radius

$S(\gamma)$ is a function only of the ratio of the specific heat (= 1.009 for air)

E = instantaneous energy release per unit length on the shock axis at $t = t_0$

ρ_0 = initial ambient density

M = Mach number

V = shock wave velocoty.

CHAPTER V :

n_1 = refractive index in liquid for light parallel to the applied field

n_2 = refractive index in liquid for light whose polarization is perpendicular to the applied field

λ = wavelength

k = Kerr's constant

E = electric intensity

I_0 = incident light intensity

I = intensity of transmitted light through Kerr cell

ω = angular frequency of modulation voltage

ϵ = dielectric constant

R = distance to a datum of potential $\gg$ distances in the diagram

δ = phase retardation of extra-ordinary ray

d = distance from wire to electrical image (= 2h) see Fig.5.1.

CHAPTER VI

K_e = dielectric constant

$p-p_o$ = excess pressure

ϵ_o = permittivity of free space

E = electrostatic field

P = dipole moment

T = torque

C = compressibility

V = volume

λ = wavelength

m = Bragg order

θ = angle of incidence

D = grating spacing

R = reflectivity

N = number of modulations crossed

δ = $\Delta n_a/2n_{ao}$

b = tip radius of curvature

n_o = undisturbed refractive index for argon light

Δn = change in refractive index for argon light

k = $2\pi/\lambda$

δA_r = amplitude of wave reflected from boundary

A_i = amplitude of incident wave

θ' = angle of refraction at refractive index boundary

z = distance through grating parallel to electrode surface

REFERENCES

(1) STOKES, E.E., Phil. Mag, 3, (33), 349-356 (1848).

(2) RAYLEIGH, Lord, Proc. Roy. Soc., 84, 247-284 (1910).

(3) BAND, W., DUVELL, G.E., Amer. J. Phys., 29, 780 (1961).

(4) LANDAU, L.D., LIFSHITZ, E.M., 'Course of Theoretical Physics', vol.6, Pergamon Press, (1959).

(5) RANKINE, W.J.M., Trans. Roy. Soc., 160, 277-288 (1870).

(6) HUGONIOT, H, Journal de l'école Polytechnique, 58, 1 (1889).

(7) COURANT, R., FRIEDRICHS, K.O. 'Supersonic Flow and Shock Waves', Interscience, (1948).

(8) TAYLOR, G.I., MACCOLL, J.W. 'Mechanics of Compressible Fluids' editor W.F. Durand. vol.VIII, (1935).

(9) TAYLOR, G.I., Proc. Roy. Soc. A., 201, 159 (1950).

(10) TAYLOR, G.I., Proc. Roy. Soc. A., 201, 175 (1950).

(11) SCHARDIN, H., Comm. on Pure and Applied Maths., 7, 223 (1954).

(12) LIN, S-C., J. Appl. Phys., 25, 1, 54 (1954).

(13) BRIDGMAN, P.W., Revs. Mod. Phys., 18, 1 (1946).

(14) GORANSON, R.W. et al., J. Appl. Phys., 26, (12), 1472 (1955).

(15) WALSH, J.M., CHRISTIAN, R.H., Phys. Rev., 97, 1544 (1955).

(16) DUVAL, G.E., ZWOLINSKI, B.J., J. Acoust. Soc. Amer., 27, 1054 (1955).

(17) BUCHANAN, J.S., JANES, H.J. and TEAQUE, G.W., Phil. Mag. (series 8), 3, 1424 (1958).

(18) LAWTON, H., SKIDMORE, I.C., Discs. of Faraday Soc., 54, (22), 188 (1956).

(19) MINSHALL, S., J. Appl. Phys., 26, 463 (1955).

(20) BANCROFT, D. et al., J. Appl. Phys., 27, 291 (1956).

(21) WALSH, J.M., RICE, M.H., J. Chem. Phys., 26, 815 (1957).

(22) RICE, M.H., WALSH, J.M., J. Chem. Phys., 26, 824 (1957).

(23) DEAL, W.E., J. Appl. Phys., 28, 782 (1957).

(24) PACK, D.C., EVANS, W.M., JAMES, H.J., Proc. Phys. Soc. London, 60, 1 (1948).

(25) BENNETT, F.D., BURDEN, H.S. and SHEAR, D.D., Phys. Fluids, 5, (1), 102 (1962).

(26) EARNSHAW, K.B., BENEDICT, C.M., J. Research, Nat. Bur. Stand. 66C, 297 (1962).

(27) EYLON, Sixth Conference of High Speed Photography, 331, (1962)

(28) BELL, C.E., LANDT, J.A., Appl. Phys. Letts., 10, (2), 46 (1967).

(29) SCHARDIN, H., Ergen. Exact. Naturw., 20, (1941).

(30) CHESTERMAN, W.D., 'The Photographic Study of Rapid Events', Oxford University Press, (1951).

(31) ZELDOVICH, Ya.B., et al., Sov. Phys. Doklady, 6, (6), 494 (1961).

(32) FLOOK W.M., HORNIG, D.F., J. Chem. Phys., 23, (5), 816 (1955).

(33) GINZBURG, V.P., MOTULAVICH, G.P., Uzp. Fiz. Nauk., 55, 469 (1955).

(34) ALTSHULEV, L.V., et al., Sov. Phys. Doklady, 3, 761 (1958).

(35) SIMPSON, D., SMY, P.R., J. Appl. Phys., 40, (12), 4928 (1969).

(36) EWALD, A.H., HAMANN S.D., Appl. Phys. Letts., 2, (3), 49 (1963).

(37) LUCAS, R Compt. Rend., 206, 827 (1938).

(38) PETERLIN, A., J. Phys. Radium., 11, 45 (1950).

(39) RUTGERS, A.J., RIGOLE, W., Trans. Faraday Society, 54, 139 (1958).

(40) DAVID, H.G., EWALD, A.H., Australian J. Appl. Sci., 11 (3), 317 (1960).

(41) PHILIPPOFF, W., Nature, 181, 1011 (1958).

(42) FRÜNGEL, F., et al. Proc. 3rd Int. Congr. on High Speed Photography London (1956).

(43) FRÜNGEL, F., 'High Speed Pulse Technology', vol.1, Academic Press, (1965).

(44) FRÜNGEL, F., Explosivstoffe, 10, 236, (1958).

(45) MACK, J.E., MDDC, 221, U.S. Atomic Energy Commission (1947).

(46) ZELDOVICH, Ya.B., and RAIZER, Yu.R., 'Physics of Shock Waves and High-Temperature Hydrodynamic Phenomena', Academic Press (1967).

(47) FOWLER, R.G. et al., Phys. Rev., 88, 137 (1952).

(48) KOLB, A.C., Phys. Rev., 107, (2), 345 (1957)

(49) KOLB, A.C., Phys. Rev., 107, 1197 (1957).

(50) ANDERSON, J.A., Astrophysics Journal, 51, 37 (1920).

(51) ANDERSON, J.A., Astrophysics Journal, 64, 295 (1926).

(52) BENNETT, F.D., Phys. Fluids, 1, (4), 347 (1958).

(53) BENNETT, F.D., Phys. Fluids, 1, (6), 515 (1958).

(54) BENNETT, F.D., Phys. Fluids, 5, (8), 891 (1962).

(56) BENNETT, F.D., KAHL, G.D. and WEBER, F.N., Phys. Fluids, 13, (7), 1725 (1970).

(57) ZERNOW, L. et al., Photo. Sci. and Engineering, 4, (1), 31 (1960).

(58) MELNIKOV, M.A., BARCHENKO, T.N., Izvestiya VUZ Fizika, 4, 39, (1965).

(59) MELINKOV, M.A., OBUKHOV, V.I., Izvestiya VUZ Energetika, 1 99 (1963).

(60) OKTAY, E., Rev. Sci. Instrum. 39, (9), 1327, (1965).

(61) YAAKOBI, B. et al., Proc. Seventh Inter. Conf. on Ionization Phenomenon in Gases, 1, 799 (1966)

(62) KATZENSTEIN, J., SYDOR, M., Rev. Sci. Instrum., 32, 989 (1961).

(63) YAAKOBI, B, J. Quant. Spectrosc. Radiat. Transf., 9, 1603 (1969).

(64) CARLSON, G.A., J. Appl. Phys. (USA), 42 (5), 2155 (1971).

(65) McGRATH, J.R., J. Appl. Phys., 37, (12), 4439 (1966).

(66) NYKL, J. Appl. Phys (USA) 39, (9), 4475 (1968).

(67) BARNETT, T.R., Ph.D. Thesis, London University, (1957).

(68) ALLEN, , MAPES, and MAYFIELD, E.B., J. Appl. Phys., 26, 125 (1955).

(69) VALKENBURG, M.E. van, CLAY, W.G. and HUTH, J.H. J. Appl. Phys., 27, 1123 (1956)

(70) ROSTOKER, N., Meteoritics, 1, 11 (1953).

(71) Proc. Third Symposium on Hypervelocity Impact, vol.1, February 1959.

(72) MAYFIELD, E.B., ROGERS, J.W., J. Appl. Phys., 31, 3 (1960).

(73) LIGHTHILL, M.J., Mem. Manch. Lit. Phil. Soc., 101, 7 (1959).

(74) STOKER, J.J., Comms. on Appl. Maths., 1, (1), 1 (1948).

(75) AFANASEV, Yu.V., KOKHIN, O.N., Sov. Phys. JETP, 25, (4), 639 (1967).

(76) DAWSON, J.M., Phys. Fluids, 7, (7), 981 (1964).

(77) BASOV, N.G. et al., JETP Letts., 6, 168 (1967).

(78) ANISIMOV, S.I. et al., Sov. Phys. - Tech. Phys., 11, (7), 945 (1967).

(79) ANISIMOV, S.I., Sov. Phys. JETP, 27, (1), 182 (1968).

(80) STEVERDING, B., J. Phys. D., 3, 358, (1970).

(81) AFANASEV, Yu.V. et al., Sov. Phys. - Tech. Phys., 14, (5), 669 (1969).

(82) ANISIMOV, S.I., Sov. Phys. JETP, 31, (1), 181 (1970).

(83) BATANOV, V.A., et al. ZhETF Pis. Red., 11, (2), 113 (1970).

(84) UJIHARA, K., KAMIYAMA, M., Proc. IEEE, 57, 1664 (1969).

(85) UJIHARA, K., Proc. IEEE (Letters), 56, 2090, (1968).

(86) READY, J.F., J. Appl. Phys., 36, 2, 462 (1965).

(87) HOWE, J.A., J. Chem. Phys., 39, 1362 (1963).

(88) MOTT, N.F., JONES, H., 'The Theory and Properties of Metals and Alloys', Dover, (1958).

(89) READY, J.F., Appl. Phys. Letts., 3, 11 (1963).

(90) READY, J.F., 'Effects of High Power Laser Radiation' Academic Press, Ch.3, (1971).

(91) DABBY, F.W., PAEK, Un-C, IEEE J. Quantum Electronics, QE-8, 2 106 (1972).

(92) MASTERS, J.I., J. Appl. Phys., 27, 477 (1956).

(93) CARUSO, A., et al., Il Nuovo Cimento, XLV B, N.2, 176 (1966).

(94) CHUN, M.K., ROSE, K., J. Appl. Phys., 41, (2), 614 (1970).

(95) HAUN, R.D., IEEE Spectrum, 5, (5), 82 (1968).

(96) CAROME, E.F., et al., J. Acoust. Soc. Am., 40, 1462, (1966)

(97) CAROME, E.F., et al., Appl. Phys. Letts., 11, (2), 64 (1967).

(98) ROACH, J.F. et al., Proc. IEEE, 57, 1693 (September 1969).

(99) KAPANY, N.S. et al., Appl. Optics., 4, (5), 517 (1965).

(100) CAMPBELL, C.J. et al., Trans. Am. Acad. Opth. Otolaryngol., 67, 58 (1963).

(101) ZARET, M.M. et al., Science, 134, 1525 (1961).

(102) BARNES, P.A., RIECHKOFF, K.E., Appl. Phys. Letts., 13, 282, (1968).

(103) ROWLEY, D.M., Ph.D. Thesis, London University (1971)

(104) LANE, W.R., EDWARDS, J., Ministry of Supply, Porton Tech. Paper no.71. (1948).

(105) LANE, W.R., J. Sci. Inst., 24, 98 (1947).

(106) LANE, W.R., PREWETT, W.C. and EDWARDS, J. Porton Tech. Paper no.115, Ministry of Supply (1949).

(107) AHLBORN, F., Phys. Zeit., 32, 138 (1931).

(108) TAYLOR, G.I., Porton Tech. Paper n . R.S. 8505/42, Ministry of Supply, (1949).

(109) THOMSON, J.J., NEWALL, H.F., Proc. Roy. Soc., 39, 417 (1885).

(110) RAYLEIGH, Lord., Proc. Roy. Soc., 29, 71 (1879).

(111) KINGSBURY, E.F., Rev. Sci. Inst., 1, 22 (1930).

(112) DUNNINGTON, F.G., Phys. Rev., 38, 1506 (1931).

(113) DUGUAY, M.A., HANSEN, J.W. Appl. Phys. Letts., 15, 6, 192 (1969).

(114) STORE, J. et al., Appl. Optics, 5, (4), 653 (1966).

(115) FEWKES, J.H., YARWOOD, J., 'Electricity and Magnetism', University Tutorial Press, (1965).

(116) BRIERE, G., GASPARD, F., Chem, Phys. Letts., 1, (13), 706 (1968).

(117) KEY, P.Y., HARRISON, R.G., LITTLE, V.I. and KATZENSTEIN, J. IEEE J. Quantum Electronics, QE-6, (10), 641 (1970).

(118) LEITE, R., MOORE, R. and WINNERY, J., Appl. Phys. Letts., 5, 141 (1964)

(119) DABBY, F., WINNERY, J., Appl. Phys. Letts., 13, 284 (1968).

(120) CHIAO, R.Y., et al., Phys. Rev. Letts., 12, 592 (1964).

(121) GROB, K., Zeitschrift, fur Physic, 201, 59 (1967).

(122) HARRISON, R.G. et al., Appl. Phys. Letts., 13, (8), 253 (1968).

ACKNOWLEDGEMENTS

I would like to acknowledge the kind advice and guidance of my supervisor Dr V.I. Little, who conceived this project and has given full support throughout.

So too, I would like to record my gratitude to the late Prof. S. Tolansky who has obtained the financial support necessary for this work.

This work has been carried out at Royal Holloway College, and I would like to acknowledge all my many friends and colleagues there, whose help I have taken. In particular I wish to thank Mr R. Elton who has constructed most of the apparatus.

I wish to thank Wilkinson Sword Blade Ltd. for the procision of numerous razor blades for use in this research.

My special thanks are also due to Ina Godwin for her hard work both in deciphering my writing and in typing this thesis.